CFD BASED PREDICTION OF ROTORDYNAMIC COEFFICIENTS AND STABILITY ANALYSIS FOR CENTRIFUGAL PUMP/COMPRESSOR

A Dissertation

by

EUNSEOK KIM

Submitted to the Office of Graduate and Professional Studies of
Texas A&M University
in partial fulfillment of the requirements for the degree of

DOCTOR OF PHILOSOPHY

Chair of Committee,	Alan B Palazzolo
Committee Members,	Dara Childs
	Ham-Ching Chen
	Robert Handler
Head of Department,	Andreas A. Polycarpou

December 2016

Major Subject: Mechanical Engineering

ABSTRACT

Fluid forces acting on the shrouded centrifugal pump/compressor impellers are evaluated using the computational fluid dynamics (CFD) approach. A face-seal impeller is selected to study for predicting the rotordynamic coefficients of the whirling impeller. The resultant impedances of the face-seal impeller can be modeled as a quadratic polynomial of whirling frequency to calculate the rotordynamic coefficients. However, the impedances of a conventional wear-ring seal impeller have some inflection points in the curves. Some possible sources that can affect the fluctuating impedance curves are investigated by varying design parameters such as shape of leakage path, inlet tangential velocity, flow rate of primary passage, and seal clearance. Effects of the peaks in the impedance curves of the wear-ring seal impeller are evaluated by performing stability analysis of a rotordynamic finite element (FE) model with the unconventional impedances. A linear curve-fit algorithm is developed to identify the complex shape of impedance curves of the wear-ring seal impeller. A Jeffcott rotor model with the impeller forces is modeled to apply and validate the developed curve-fit algorithm and the stability analysis has been performed. The analysis results indicate that the bump and dip in the impedance curves destabilize the Jeffcott rotor.

Precessing motion of the shrouded centrifugal impeller is also an important vibration source that can cause the rotordynamic instability problem. By considering the tilted impeller, the reaction force and moment coefficients of the face-seal impeller are predicted utilizing CFD technique, and a full set of the rotordynamic coefficient matrices

(4×4) is calculated. In order to evaluate the coupled motion of whirling and precessing for the face-seal impeller, a 3D impeller model with the dynamic eccentricity and the tilting angle is generated and the corresponding rotordynamic coefficients are obtained. The calculated results indicate that the precessing motion increases the tendency towards destabilization of the rotor.

Lastly, influence of static eccentricity on the face-seal impeller is investigated. In actual operation of the rotor, misalignment may be destabilizing and cause serious vibration problems. A CFD modeling approach is developed to evaluate the forces for the statically eccentric face-seal impeller, and it has been found that the presence of static eccentricity on the face-seal impeller has an adverse effect on rotordynamic stability.

ACKNOWLEDGEMENTS

I would like to express my deepest thanks to my advisor, Dr. Alan Palazzolo for his immeasurable considerations and concerns during my graduate study in the Vibration Control Electromechanical Lab. I also would like to thank my committee members, Dr. Dara Childs, Dr. Ham-Ching Chen, and Dr. Robert Handler, for their guidance and support throughout the course of this research.

Thanks also go to my friends and colleagues and the department faculty and staff for making my time at Texas A&M University a great experience.

Finally, thanks to my family members for their encouragement and moral support.

NOMENCLATURE

A	system matrix of Jeffcott rotor model
$A_{xx}, A_{xy}, A_{yx}, A_{yy}$	state matrices of impedances
$[A]$	system matrix of FE model
$[B]$	control matrix of Jeffcott rotor model
$B_{xx}, B_{xy}, B_{yx}, B_{yy}$	input matrices of impedances
c_b	bearing damping of Jeffcott rotor model (*N-s/m*)
$C_{xx}, C_{xy}, C_{yx}, C_{yy}$	output matrices of impedances
$[C]$	global damping matrix of FE model
$[C_B]$	bearing damping matrix of FE model
$[C_G]$	gyroscopic matrix of FE model
D_I	diameter (*m*)
e	imbalance eccentricity distance (*m*)
f	Ω / ω, Precession Frequency Ratio (PFR)
F	unbalance force vector of Jeffcott rotor model
F_r	radial reaction force of impeller (*N*)
F_t	tangential reaction force of impeller (*N*)
F_x	reaction force of impeller in x-direction (*N*)

F_y	reaction force of impeller in y-direction (*N*)
$\{F_u\}$	unbalance force vector of FE model.
$\{\tilde{F}_u\}$	magnitude of unbalance force vector of FE model
$[F_I]$	impeller impedance matrix of FE model
H	head (*m*)
I , or $[I]$	Identity matrix
I_r	Radial impedance
I_t	Tangential impedance
ISR	Inlet Swirl Ratio of impeller model
K, C, M	direct stiffness, damping, mass (*N/m, N-s/m, kg*)
k,c,m	cross-coupled stiffness, damping, mass (*N/m, N-s/m, kg*)
k_b	bearing stiffness of Jeffcott rotor model (*N/m*)
$[K]$	global stiffness matrix of FE model
$[K_B]$	bearing stiffness matrix of FE model
$[K_S]$	shaft stiffness matrix of FE model
m_d	disk mass of Jeffcott rotor model (*kg*)
$[M]$	global mass matrix of FE model
N	spin speed of impeller (*rad/s*)
p	static pressure (Pa)

ΔP	pressure difference between shroud inlet and seal outlet (Pa)
PFR	Precession Frequency Ratio ($f = \Omega / \omega$)
Q	flow rate of impeller (m^3 / s)
$T_{xx}, T_{xy}, T_{yx}, T_{yy}$	force vectors of impedances
V_0	inlet tangential velocity
v_x, v_y	velocity of disk center (*m/s*)
x,y,z	Cartesian coordinates
$x(t), y(t)$	position of disk center (*m*)
$Z_{xx}, Z_{xy}, Z_{yx}, Z_{yy}$	state vectors of impedances
$\tilde{Z}$	eigenvector of Jeffcott rotor model
$\{z\}$	displacement vector of FE model
$\{\tilde{z}\}$	magnitude of displacement vector of FE model
δ	logarithmic decrement of Jeffcott rotor model
ε	eccentricity of whirling motion (*m*)
$\boldsymbol{\varepsilon}$	turbulence dissipation
ζ	damping ratio of Jeffcott rotor model $\zeta = \frac{c}{2\, m\, \omega_n}$
$\boldsymbol{k}$	turbulence kinetic energy
θ_x, θ_y	angular displacement
λ	eigenvalue of Jeffcott rotor model

ϕ	flow coefficient
ψ	head coefficient
ω	spin speed (*rad/s*)
ω_n	natural frequency of Jeffcott rotor model (*rad/s*) $\omega_n = \sqrt{\frac{k}{m}}$
Ω	whirl frequency (*rad/s*)
Ω_w	whirl frequency ratio at instability ($\frac{k}{C\omega}$)

TABLE OF CONTENTS

Page

LIST OF FIGURES

Page

LIST OF TABLES

Page

1. INTRODUCTION

1.1 Overview

Centrifugal pumps and compressors have various vibration sources which can produce serious instability problems. Among many possible sources of the rotor vibration, fluid forces acting on the turbomachines have been considered an important factor causing rotordynamic instability. In order to analyze the fluid forces, much research has been performed experimentally and theoretically. These studies explained that fluid forces acting on the shroud surface play an important role in the resulting destabilizing forces and understanding the mechanism of the forces are crucial to design turbomachines with higher power densities. In the present study, various destabilizing mechanism of the shrouded centrifugal impellers and the resultant impedances of the impellers will be addressed using CFD technique.

1.2 Literature Review

1.2.1 Measurements of Hydrodynamic Forces on Centrifugal Impellers

Jery et al. [1] measured radial and tangential forces of a 3D centrifugal impeller and the resulting impedances from the experiment fairly matched a quadratic curve. Least square curve fit algorithm was used to calculate the rotordynamic coefficients from the measured forces. The authors showed that the identified rotordynamic coefficients matrices have equal diagonal elements and skew-symmetric off-diagonal elements. Measurements were performed to investigate the effect of a flow coefficient

and diffuser guides of the impeller. The flow coefficients is defined based on the impeller discharge area and tip speed ($Q / \omega r_2 A_2$ Q : flow rate, ωr_2 : impeller tip speed, A_2 : discharge area). The experimental data showed that the hydrodynamic forces are affected a lot by the flow coefficient rather than the diffuser guides.

Bolleter et al. [2] tested a boiler feed pump impeller with vaned diffuser. Seal forces were not considered by employing a face seal on the suction side of the shrouded impeller. The rotordynamic coefficients of the impeller system were identified by performing hydrodynamic force measurements using translational motion and wide frequency range excitation. In 1989, Bolleter et al. [3] implemented additional experiments by changing the geometry of the impeller shroud, type of seal, spin speed and temperature. The tested impellers had tighter clearance of the shroud leakage flow path and this resulted in higher values of the rotordynamic coefficients when compared to the results of Jery et al. [1]. In the test case of an impeller with an annular seal, a whirl frequency ratio at instability ($k / C\omega$) was 2.26. The abnormally high value of the whirl frequency ratio at instability was reduced to 1.16 by attaching a small swirl break in the suction side of the impeller.

Ohashi et al. [4] measured lateral fluid forces on two and three dimensional centrifugal impellers. The authors evaluated the effect of vaned and vaneless diffusers, clearance between the front shroud and the casing, and interaction between the impeller and the guide vane. Fluid induced forces on a 3D impeller with a vaned diffuser are 50% larger than those with a vaneless impeller. The authors concluded that the clearance between the casing and the shroud has an influence on the fluid induced forces on the

front shroud of the impeller and the hydrodynamic forces acting on the shroud surface are increasing with smaller gap between casing and front shroud.

Yoshida et al. [5] investigated the effect of the interaction between the impeller and the volute casing. The measured tangential force increased as the flow rate was reduced and the whirling speed was lowered. Tsujumoto et al. [6] implemented flow and pressure measurements in the back shroud/casing clearance of a precessing centrifugal impeller and integrated the unsteady pressure distribution to obtain the fluid moment coefficients. Yoshida et al. [7] measured detailed flow and pressure in the backshroud/casing clearance to calculate moment coefficients. The inlet gap ('Gap-A') of backshroud leakage flow path and the leakage flow influenced the rotordynamic stability. With the decreased inlet gap, the absolute values of fluid moments are increasing. The increased leakage flow makes the impeller more destabilizing.

1.2.2 Bulk Flow Analysis for Shroud Leakage Path

Childs [8] employed a bulk-flow analysis for the leakage path between an impeller shroud and a pump housing to predict rotordynamic coefficients. A face-seal pump impeller and a conventional wear-ring seal pump impeller were considered. The determined rotordynamic force coefficients of the face-seal pump impeller case showed reasonable correlation to experiment results measured by Bolleter et al. [2]. In Childs' model, recirculation zones in the shroud leakage path could not be captured since the bulk-flow model can analyze only 1D fluid flow. In his results for the face-seal pump impeller and the conventional wear-ring seal pump impeller, 'dips' and 'bumps' were

observed in the radial and the tangential impedances curves. Because of the peaks, the predicted impedances cannot be modeled by the conventional MCK (Mass-Damping-Stiffness) model. The phenomenon disappeared when the centrifugal acceleration term in the bulk flow model is removed.

Gupta [9] utilized a bulk flow model for compressible flow and verified his approach by comparing the results with the measurement data of Yoshida et al. [7]. The compressible bulk flow model showed dips and bumps in the calculated impedance curves and the recirculation zones couldn't be observed due to the limitation of the bulk flow model. Based on the verified approach, a full set of rotordynamic coefficients (4X4 matrices) of an impeller stage was predicted and the stability analysis performed by applying the predicted coefficients to a semi cantilevered rotor.

1.2.3 CFD Approaches for Rotordynamic Problems

Baskharone et al. [10] modeled a 3D eccentric impeller shroud region of Sulzer impeller tested by Bolleter et al. [2] and evaluated the rotordynamic coefficients using FEM based solution. The calculated impedance curves of the face-seal impeller in the FE solution showed smooth curves without bumps and dips. Baskharone et al. [11] investigated the main and leakage flow by adding the primary passage on the shroud model. However, any perturbations were not imposed in the FE model and no rotordynamic coefficients were predicted.

Moore et al. [12] performed prediction of rotordynamic forces acting on the shroud surface of a centrifugal pump impeller. They used TASCflow which is a

commercial code utilizing FVM based CFD technique. For the CFD analysis, a 3D eccentric structured grid for the shroud leakage path was generated. The eccentric grid of the shroud region was combined with the centered grid model of the blade impeller and rotordynamic prediction performed using the commercial CFD solver. In the combined impeller grid model, the eccentricity for generating whirling orbit was applied to only shroud region and the primary passage was assumed to be operating at centered position. The imposed eccentricity of the grid model was determined to have 10% of the shroud clearance based on the study of Moore et al. [13]. The predicted rotordynamic coefficients for the face-seal impeller in the study were well matched with the measurement data of Bolleter et al. [2]. The fluctuating impedance curves shown in the result of bulk flow code by Childs [8] were not observed in the CFD results of the face-seal impeller.

Moore et al. [14] adopted a commercial CFD code for predicting the rotordynamic coefficients of a centrifugal compressor. Unstructured mesh technique utilized to generate 3D eccentric grid model. Likewise the face-seal impeller case of Moore et al. [12], only shroud region was modeled to have 10% eccentricity of the shroud clearance. The considered compressor in the paper has 4 stages and suffered from rotordynamic instability. Simulations are performed using the given boundary conditions to predict the rotordynamic coefficients of the multistage compressor. The predicted rotordynamic coefficients for stage 1 and stage 3 showed good agreement with the experimental data. Based on the parametric study using the calculated rotordynamic

coefficients, the authors developed a new analytical formula to predict the cross-coupled stiffness for the centrifugal compressor impellers.

1.2.4 Measurements and Analysis of Unconventional Impedances

Franz et al. [15] observed unconventional impedance curves with bumps and dips in their measurement and showed the phenomenon was influenced by the flow coefficients. Brennen et al. [16] also observed the bumps and dips in the measured radial and tangential impedances of the centrifugal impellers at lower flow operations. Similar experimental evidences were observed in experimental results (figure 8 and 9) of Bolleter et al. [3]. Bolleter pointed out that the measured radial and tangential impedances didn't have parabola curves at lower flow rates in their experiments.

Childs [8] predicted qualitatively similar results in his bulk flow analysis on the shrouded pump impellers and performed extensive studies on the bumps and dips in the impedance curves [17-19]. Childs [17] examined the axial reaction forces which are caused by the pressure and the shear stress on the shroud surface. He introduced a method for estimating stiffness, damping, and mass coefficients for the axial reaction forces. The effects of the rotordynamic coefficients for the axial reaction forces were investigated by applying the coefficients in a double-suction single-stage pump. The rotordynamic coefficients for the axial reaction forces were meaningful only for the case that system natural frequency is much lower than the operating speed. An approach to calculate eigenvalues for the lateral excitation and the axial vibration was developed in Childs [18]. In the research, eigensolutions (magnitude and phase) for the path velocity,

circumferential velocity, and pressure were calculated and analyzed according to the inlet swirl ratio. In 1992, Childs [19] analyzed the effect of pressure oscillation in the shroud leakage path. The variation of the impeller discharge pressure in circumferential direction cause the pressure oscillation in shroud clearance. Peak-pressure oscillation in the shroud leakage path appeared near the wear-ring seal in the analysis.

Williams et al. [20] suggested an approach to evaluate the unconventional impedance curves in his bulk flow models. They modeled the impedances by dividing them into constant rotordynamic coefficients (mass, stiffness, damping) and whirl-frequency-dependent direct and cross-coupled stiffness. Using the approach, they evaluated the Jeffcott-based, double-suction impeller leakage path model and concluded that the peaks in the impedances had considerable effect on rotordynamic stability of the impeller model.

1.2.5 System Identification for Unconventional Impedances

Kleynhans and Childs [21] introduced general transfer function model, utilizing the impedance model of Bolleter et al. [2]. Their research was motivated to model the radial and tangential impedances of a long honeycomb gas seal which cannot be modeled using the conventional reaction force equation. Kleyhans employed approximated transfer functions to express the unconventional impedance curves in Laplace domain. Although their approach couldn't be fully investigated because of the limited frequency range of the used test data, they suggested useful Laplace-domain model to perform rotordynamic analysis for the unconventional impedances. Based on

the research of Kleyhans et al. [21], Thorat et al. [22] expanded the model by using a curve-fit approach to obtain the impedance functions, D and E, which were introduced by Bolleter et al. [2]. Thorat derived D and E functions in the forms of standard polynomial. He extracted the stiffness and damping coefficients from the derived D and E function to model frequency dependent Models. Comparisons were made between traditional frequency independent force model and frequency dependent model to show the validity of their new approach for estimating the unconventional impedance functions.

1.2.6 Effect of Static Eccentricity on Rotordynamic Instability

Falco et al. [23] tested a short seal to investigate the effect of the static eccentricity on the cross-coupled stiffness and direct stiffness of the seal. In the case, L/D =0.25 and eccentric ratio (e/c) was examined up to 0.7. Analytical solutions of a Reynolds' equation based finite element model were also obtained and comparisons were made with the experiment data. The predicted results were fairly close to the measured data for the eccentric plain annular seal.

Nelson et al. [24, 25] developed an approach to analyze eccentric annular incompressible seals. A bulk flow model with moody friction model is utilized. Zeroth order equations were solved by employing Fast Fourier Transforms (FFT). The developed approach was verified by comparisons with the experiment data performed by Jenssen [26]. First order equation also solved in Ref. [25] to calculate the rotordynamic coefficients for the static displacement of the eccentric annular seal. Comparisons were

made with the experiment data of Falco et al. [23] and Allaire et al. [27]. Nelson's approach showed improved results than the predictions for the short seal case of Falco et al. [23].

Padavala et al. [28] developed a simple scheme based on cubic splines to obtain solutions for a statically eccentric seal, an arbitrary profile seal, and a distorted seal. Using the method, the authors could make simpler solution procedures than the approach of Nelson et al. [25]. Comparisons were made with the predictions of Nelson's and Allaire's approach for the case of Allaire et al. [27]. The predicted rotordynamic coefficients showed similar rotordynamic coefficients with the results of Nelson and Allaire.

Kanki and Kawakami [29] measured the rotordynamic force from the circular whirling motion of a pump annular seal and evaluated the rotordynamic coefficients according to the applied static eccentricity. Test conditions are 2,000 rpm and $\Delta p = 0.98\,MPa$. The tested plain annular seal is $L/D = 1.0$ and $C_r/R = 0.005$. San Andres [30] utilized a finite difference scheme to solve the turbulent flow in the seal. Moody friction factor was used to account for surface roughness effects. Using the developed approach, San Andres predicted the measured seal case of Kanki and Kawakami [29] and showed fairly good agreement. Kanki and Kawakami [31] tested grooved seals and showed that the grooved seal is insensitive to changes in eccentricity ratio.

Marquette et al [32] provided measured results and predictions for a seal with $L/D = 0.45$ and $C/R = 0.0029$. For the prediction of leakage flowrate and the

rotordynamic coefficients, a developed code by San Andres [30] was utilized. Overall predictions of the rotordynamic coefficients showed good agreement with the test results. Leakage flowrate increased with increasing Δp, and reduced with higher running speed. With the increased eccentricity, the leakage flow rate increased slightly. The seal became more unstable with increasing eccentricity. Marquette et al. [33] also provided rotordynamic coefficients versus eccentricity ratio and leakage flow rate results for finely and coarsely grooved seals. For the predictions, Marquette et al. [33] utilized three control volume bulk flow theory with Hirs friction model. Rotordynamic coefficients and leakage flow rate for grooved seals are relatively insensitive to static eccentric ratio up to 0.5. The authors concluded that the grooved seal is more stable than the plain annular seals [32] in the aspect of the whirl frequency ratio. However, the grooved seals were less stable than the plain annular seals [32] based on effective damping. In their results, overall predictions showed accurate results except cross-coupled stiffness terms.

1.3 Objectives and Contributions of Current Work

API 617 level-II analysis [34] for the rotordynamic stability of centrifugal compressors requires detailed computed rotordynamic coefficients if level-I criteria fails. Thus, more accurate calculation of the rotordynamic coefficients is important to examine the rotordynamic stability. The goal of the current work is to predict more reliable fluid induced forces and the corresponding rotordynamic coefficients of shrouded centrifugal compressor/pump impellers. This will be implemented through the use of the commercial CFD code, ANSYS CFX. The specific objectives and contributions are:

1) To develop a numerical approach to calculate 4×4 rotordynamic coefficients with CFD :

CFD models to determine 4×4 rotordynamic coefficients will be developed in the current work. To calculate the full set of the rotordynamic coefficients using CFD technique, the circular motion with the whirling orbit and the conical motion with the tilt angle should be modeled. Since there's no validated approach to model 3D tilted centrifugal impeller for the CFD analysis, the developed approach for the tilted impeller will be verified by considering the test case of [7]. After the verification, the 4×4 rotordynamic coefficients will be calculated for the face-seal impeller analyzed in [2, 8, 12] and the rotordynamic analysis will be performed using the coefficients to estimate the stability of the impeller.

2) To develop a CFD modeling approach for coupled circular and conical motion of a shrouded centrifugal face-seal impeller:

In the real rotor operation, lateral motion and tilt motion arise together when considering the flexible rotor bending motion. The coupled (circular + conical) motion can be modeled in one CFD complete model by imposing whirling orbit and tilting angle. In the present study, ANSYS CFX is utilized to model the coupled rotor motion by imposing dynamic eccentricity and tilting angle in the 3D shrouded face-seal impeller model. Because of the geometric constraint, small angles (0.025 ° and 0.05 ° in the face-seal impeller case) should

be imposed with the dynamic eccentricity. The effect of the coupled motion on the rotordynamic stability will be investigated by evaluating the whirl frequency ratio at instability using the resultant rotordynamic coefficients from the CFD simulation of the coupled motion.

3) To examine factors causing rotordynamic instability of a shrouded centrifugal impeller:

As reviewed in the above, Childs [8] predicted the unconventional impedances for the face-seal impeller and the wear-ring seal impeller. The phenomenon also observed in the measurements of Franz et al. [15] and Brennen et al. [16]. For the face-seal impeller case, Moore [35] calculated the fluid induced forces acting on the shroud surface using CFD approach and the bumps and dips in the impedance curves were not observed. The same face-seal impeller model is constructed for the verification in the current research and the estimated impedances show typical impedance curves for the positive precession frequency range. However, slight bumps and dips can be observed in the predicted impedance curves when the fluid induced forces on the shroud surface are calculated for a wider range including the negative frequency region. For the wear-ring seal case, the bumps and dips in the predicted impedance curves are clearly seen and the trend and shape are very similar with the results of Childs [8]. According to Childs' analysis, the unconventional impedances resulted from the centrifugal acceleration term in his bulk flow model. In this study, CFD code will

be utilized to examine factors causing the peaks including the centrifugal acceleration effect. In addition, rotordynamic stability analysis will be also performed to investigate the influence of the bumps and dips in the impedance curves.

4) To develop a reliable approach to model impedances of seals and impellers:

The fluctuating impedance curves cannot be modeled by the traditional MCK model with rotordynamic coefficients. In order to identify the impedances, earlier work utilizing the transfer function approach to identify the unconventional impedance curves was suggested by Kleyhans et al. [21] and Thorat et al. [22] expanded the approach. However, Kleyhans' approach had limitations such as low curve-fit quality and limited frequency range for its application. The transfer function derived by Thorat was open-loop unstable. Thus, in order to address these limitations, a new alternate approach using fictitious, fast poles and segmentation will be suggested and validated in this research.

5) To develop a numerical approach to model a statically eccentric, whirling shrouded centrifugal impeller:

For the vibration problems of centrifugal impellers, static eccentricity has not been considered in the previous research. When considering the actual operation of the centrifugal impeller, the vibration caused by the static

misalignment is more likely to happen. Thus, an approach for analyzing the effect of the static eccentricity will be developed in this study. Measurement results by Falco et al. [23] and analysis predictions of [24, 25, 27, 28] on eccentric seals will be compared with the CFD results in order to validate the developed approach. The developed approach will be applied for the face-seal impeller case.

2. NUMERICAL METHOD DESCRIPTION[123]

The reaction forces acting on the impeller should be calculated at multiple excitation frequencies to predict the rotordynamic coefficients. For more accurate prediction of the rotordynamic coefficients, it is important to perform the CFD analysis in the wide range of the excitation frequency with the refined step. However, too many steps require high computational cost. Thus, it is important to consider efficiency as well as accuracy when choosing a numerical solver for the rotordynamic problems.

The present study utilizes ANSYS CFX to calculate the rotordynamic coefficients. ANSYS CFX uses the co-located grid approach that all flow variables are stored at the grid nodal point [36]. Basically, the approach is less laborious than the staggered grid approach utilized in other solvers because the co-located grid approach doesn't need a different grid for each velocity component and the pressure. In addition to that ANSYS CFX has been widely used to perform the rotordynamic analysis of rotating machinery and well proven in many rotordynamic problems. The validity of the selected solver (ANSYS CFX) and the numerical approach for the current research will be evaluated by

---

[1] Reprinted in Part with permission from "Rotordynamic Force Prediction of a Shrouded Centrifugal Pump Impeller-Part I : Numerical Analysis," by Eunseok Kim and Alan Palazzolo, J. Vib. Acoust. 2016; 138(3), p. 031014. © 2016 ASME.

[2] Reprinted in Part with permission from "Fluid-Structure Interaction Forces at Pump-Impeller-Shroud Surfaces for Rotordynamic Calculations," by D.W. Childs, J. Vib., Acoust., Stress, and Reliab. 1989; 111(3), pp. 216-225. © 1989 ASME.

[3] Reprinted in Part with permission from "Effects of Volute Curvature on Performance of a Low Specific-Speed Centrifugal Pump at Design and Off-Design Conditions," by Hamed Alemi, Seyyed Ahmad Nourbakhsh, Mehrdad Raisee, and Amir Farhad Najafi, J. Turbomach. 2015, 137(4), p.041009. © 2015 ASME.

the mesh density study and the comparisons of impedance curves between the predictions and the measured data in Sec. 2.7.

The standard k - ε turbulence model is selected to analyze complex turbulent flow in the shrouded impeller leakage path in the current research. Although the standard k - ε model is robust and reasonably accurate, the ε equation contains a term that cannot be calculated at the wall and the model has limitation to perform accurate prediction for flows with strong separation, large streamline curvature, and large pressure gradient. In order to compensate those drawbacks, ANSYS CFX employees the scalable wall function for the standard k - ε model and curvature correction that are utilized for the rotordynamic analysis of the present study. The subsequent sections will explain the utilized CFD technique including the scalable wall function and the curvature correction. The strategy for rotordynamic modeling will be also discussed.

2.1 The Standard $k-\varepsilon$ Turbulence Model

In turbulence models, the original unsteady Navier-Stokes Equations are modified by introducing averaged and fluctuating quantities to produce the Reynolds Averaged Navier-Stokes (RANS) equations. Think that velocities $u, v, w,$ and pressure, $p,$ may be composed of ensemble average values and turbulent fluctuations as below :

$$\begin{aligned} u &= \bar{u} + u' \qquad v = \bar{v} + v' \\ w &= \bar{w} + w' \qquad p = \bar{p} + p' \end{aligned} \tag{1}$$

Components with apostrophe denote fluctuating time varying parts and components with hyphen indicate the ensemble average or the mean value. For example,

an average component ($\overline{u}$) is given by

$$\bar{u} = \frac{1}{\Delta t}\int_{t}^{t+\Delta t} u \; dt \tag{2}$$

Substituting these decompositions of Eq. (1) to the Navier-Stokes equations and taking the ensemble average, the Reynolds averaged equations are obtained as

$$\frac{\partial \rho}{\partial t} + \frac{\partial}{\partial x_j}\left(\rho U_j\right) = 0 \tag{3}$$

$$\frac{\partial \rho U_i}{\partial t} + \frac{\partial}{\partial x_j}\left(\rho U_i U_j\right) = -\frac{\partial \rho}{\partial x_i} + \frac{\partial}{\partial x_j}\left(\tau_{ij} - \rho\overline{u_i u_j}\right) + S_M \tag{4}$$

where, S_M is the sum of body forces and τ is the molecular stress tensor. Equations for ensemble averaged values equal to the Navier-Stokes equation except for the cross-products of the fluctuation terms, $(u')^2, (v')^2, (w')^2, (u'v'), (u'w'), (v'w')$. These terms are called Reynolds stresses, $\rho\overline{u_i u_j}$, or 'turbulent stresses', since they have similar functions as viscous stresses. In order to close the system, the behavior for the turbulence cross-product terms should be defined. Reynolds Stress Model (RSM) needs transport equations for the fluctuation terms by six. This model has advantage in complex 3D turbulent flows with large streamline curvature and swirl. However, this approach is difficult to attain the converged solutions and the computational cost is higher than One-Equation or Two-Equation models. Two equation turbulence models are commonly used and the number of extra equations for the fluctuation terms is reduced to only two. ANSYS CFX provides various Two-Equation models [36]. In the current research, the standard $k-\varepsilon$ model is utilized to compute the turbulent flow and the scalable

logarithmic wall function is used to describe the near wall velocity.

In the standard k-ε model, the Reynolds stresses are assumed to be proportional to mean velocity gradients. The turbulent Reynolds stresses are approximated by the Boussinesq hypothesis and modeled as

$$-\rho\overline{u_i u_j} = \mu_t\left(\frac{\partial U_i}{\partial x_j}+\frac{\partial U_j}{\partial x_i}\right)-\frac{2}{3}\delta_{ij}\left(\rho k+\mu_t\frac{\partial U_k}{\partial x_k}\right) \quad \textbf{(5)}$$

μ_t is the turbulence viscosity defined using the turbulence kinetic energy, k, and the turbulence dissipation rate, ε, as follows :

$$\mu_t = C_\mu \rho\frac{k}{\varepsilon} \quad \textbf{(6)}$$

where, C_μ =0.09.

The extra equations are needed for the closure and the transport equations for k and ε are modeled as

$$\frac{\partial(\rho k)}{\partial t}+\frac{\partial}{\partial x_j}\left(\rho U_j k\right)=\frac{\partial}{\partial x_j}\left[\left(\mu+\frac{\mu_t}{\sigma_k}\right)\frac{\partial k}{\partial x_j}\right]+P_k-\rho\varepsilon+P_{kb} \quad \textbf{(7)}$$

$$\frac{\partial(\rho\varepsilon)}{\partial t}+\frac{\partial}{\partial x_j}\left(\rho U_j \varepsilon\right)=\frac{\partial}{\partial x_j}\left[\left(\mu+\frac{\mu_t}{\sigma_\varepsilon}\right)\frac{\partial \varepsilon}{\partial x_j}\right]+\frac{\varepsilon}{k}\left(C_{\varepsilon 1}P_k-C_{\varepsilon 2}\rho\varepsilon+C_{\varepsilon 1}P_{\varepsilon b}\right) \quad \textbf{(8)}$$

where $C_{\varepsilon 1}, C_{\varepsilon 2}, \sigma_k$, and σ_ε are constants. P_{kb} and $P_{\varepsilon b}$ represent the influence of the buoyancy forces. P_k is the turbulence production due to viscous forces, which is modeled with:

$$P_k = \mu_t\left(\frac{\partial U_i}{\partial x_j}+\frac{\partial U_j}{\partial x_i}\right)\frac{\partial U_i}{\partial x_j}-\frac{2}{3}\frac{\partial U_k}{\partial x_k}\left(3\mu_t\frac{\partial U_k}{\partial x_k}+\rho k\right) \quad \textbf{(9)}$$

The empirical constants are

$$C_{\mu} = 0.09,\ C_{\varepsilon 1} = 1.44,\ C_{\varepsilon 2} = 1.92,\ \sigma_k = 1.0,\ \sigma_{\varepsilon} = 1.30 \quad \textbf{(10)}$$

2.2 Scalable Wall Function

In the law of wall function model, the boundary layer can be divided into three regions of viscous sublayer, log layer, and defect layer, according to the near-wall distance. The near wall tangential velocity in the log layer region is related to the wall-shear-stress, τ_{ω}, by means of a logarithmic relation. The near wall velocity, u^{+}, is described as

$$u^{+} = \frac{U_t}{u_{\tau}} = \frac{1}{\kappa}\ln\left(y^{+}\right) + C \quad \textbf{(11)}$$

where,

$$y^{+} = \frac{\rho \Delta y\, u_{\tau}}{\mu},\ \mu_{\tau} = \left(\frac{\tau_{\omega}}{\rho}\right)^{\frac{1}{2}} \quad \textbf{(12)}$$

In the above equations, u_{τ}, is the friction velocity, U_t, is the known velocity tangent to the wall at a distance of Δy from the wall and y^{+} is the dimensionless distance from the wall. κ is the von-Karman constant and C is a log-layer constant depending on the roughness. For a smooth wall condition, C is 5.10.

Eq. (12) cannot be used at the separation point because the near wall velocity, U_t, approaches zero at the point and it becomes singular. To prevent this, an alternative velocity scale, u^{*}, can be utilized instead of u_{τ} as shown in the below.

$$u^* = C_\mu^{1/4} \kappa^{1/2} \tag{13}$$

This scale doesn't become zero when the near wall velocity approaches zero. By utilizing this, the following equation for u_τ can be defined as

$$u_\tau = \frac{U_t}{\frac{1}{\kappa}\ln\left(y^*\right) + C} \tag{14}$$

Then, the absolute value of the wall shear stress, τ_ω, becomes

$$\tau_\omega = \rho u^* u_\tau \tag{15}$$

where,

$$y^* = \frac{\left(\rho u^* \Delta y\right)}{\mu} \tag{16}$$

In the wall function model, the numerical calculation results are affected by the mesh quality near the wall. In addition, the accuracy of the results is not guaranteed by refining the mesh (Grotjans and Menter [37]). ANSYS CFX developed the scalable wall function approach to provide consistent solutions on arbitrarily fine meshes near the wall regardless of the Reynolds number of the application [36]. The basic idea of the scalable wall function is that the computed value of y^* is not allowed to become below 11.06. This number indicates the intersection between the logarithmic and the linear near wall profile. The y^* can be limited in ANSYS CFX by using a relationship defined as

$$\tilde{y}^* = \max\left(y^*, 11.06\right) \tag{17}$$

Eq. (17) makes all mesh points locate outside the viscous sublayer and the inconsistencies according the mesh refinement can be overcome. In order to guarantee the accuracy by applying the scalable wall function, most y^* have to bigger than 11.06.

2.3 Curvature Correction

ANSYS CFX utilizes curvature correction for Two-Equation turbulence models including the standard $\boldsymbol{k}$ - $\boldsymbol{\varepsilon}$ model to sensitize the turbulence models to streamline curvature and system rotation [36]. In order to analyze the swirling flows and flows with strong streamline curvature, an empirical function is introduced by Spalart and Shur [38] as shown below.

$$f_{rotation} = (1 + c_{r1}) \frac{2r^*}{1 + r^*} \left[1 - c_{r3} \tan^{-1}\left(c_{r2} \tilde{r} \right) \right] - c_{r1} \quad \textbf{(18)}$$

where, $c_{r1} = 1.0$, $c_{r2} = 2.0$, and $c_{r3} = 1.0$.

This function is utilized as a multiplier of the production term of Eq. (9). The multiplier is limited as follows:

$$P_k \rightarrow P_k \cdot f_r \quad \textbf{(19)}$$

where,

$$f_r = \max\left[0, 1 + C_{scale} \left(\tilde{f}_r - 1 \right) \right] \quad \textbf{(20)}$$

$$\tilde{f}_r = \max\left\{ \min\left(f_{rotation}, 1.25 \right), 0 \right\} \quad \textbf{(21)}$$

C_{scale} of Eq. (20) is utilized to influence the effect of the curvature correction for a specific flow if needed. The scaling coefficient is set as 1.0 for all cases in the current research. In Eq. (18), all the variables and their derivatives are defined with respect of the reference frame of the calculation and Ω^{rot}, r^*, and $\tilde{r}$ of Eq. (18) are defined as

$$r^* = \frac{S}{\Omega} \tag{22}$$

$$\tilde{r} = 2\Omega_{ik} S_{jk} \left[\frac{DS_{ij}}{Dt} + \left(\varepsilon_{imn} S_{jn} + \varepsilon_{jmn} S_{in} \right) \Omega_m^{Rot} \right] \frac{1}{\Omega D^3} \tag{23}$$

The strain rate and vorticity tensor are defined using Einstein summation convention as

$$S_{ij} = \frac{1}{2} \left(\frac{\partial U_i}{\partial x_j} + \frac{\partial U_j}{\partial x_i} \right) \tag{24}$$

$$\Omega_{ij} = \frac{1}{2} \left(\frac{\partial U_i}{\partial x_j} - \frac{\partial U_j}{\partial x_i} \right) + 2\varepsilon_{mji} \Omega_m^{rot} \tag{25}$$

where

$$S^2 = 2S_{ij} S_{ij},\ \Omega^2 = 2\Omega_{ij} \Omega_{ij},\ D^2 = \max(S^2, 0.09\omega^2) \tag{26}$$

2.4 Pressure-Velocity Coupling

ANSYS CFX utilizes non-staggered, a co-located grid that the control volumes are identical for all transport equations [36]. Rhie and Chow [39] introduced an alternative discretization approach for the mass flows to prevent a decoupled (checkerboard) pressure field for the non-staggered grid. Majumdar [40] performed further modification

of the discretization approach to eliminate the dependence of the steady-state solution on the time step. The Rhie-Chow interpolation is the same as adding a pressure term which is for eliminating pressure and velocity oscillations. In the continuity equation, the 4th order pressure term is added as below:

$$\left(\frac{\partial U}{\partial x}\right)_i + \frac{\Delta x^3 A}{4\dot{m}}\left(\frac{\partial^4 P}{\partial x^4}\right) = 0 \qquad \textbf{(27)}$$

The additional term in Eq. (27) is called the pressure-redistribution term and the term becomes significantly smaller when the mesh is refined to reasonable level. In the term, A is the face area and Δx is the grid spacing.

2.5 Summary of Assumptions

The summarized assumptions and numerical methods for the present study are shown in Table 1..

Table 1 Numerical method and assumptions

Analysis Type	Steady State
Turbulent model	Standard $\boldsymbol{k}$ - $\boldsymbol{\varepsilon}$, scalable wall function
Discretization scheme	High resolution
Heat Transfer	Isothermal
Wall properties	Smooth, Non-slip, Adiabatic

All the predictions of the rotordynamic coefficients in the present research are calculated using steady state solution. The wall properties of the shrouded centrifugal impeller problems are assumed to be smooth, non-slip and adiabatic. Since there are no heat sources in the selected experiment cases for the centrifugal impellers, isothermal

condition is assumed in the numerical calculation. The utilized discretization scheme is high resolution scheme (2nd order upwind scheme with limiter).

2.6 CFD Modeling for Whirling Rotor Motion

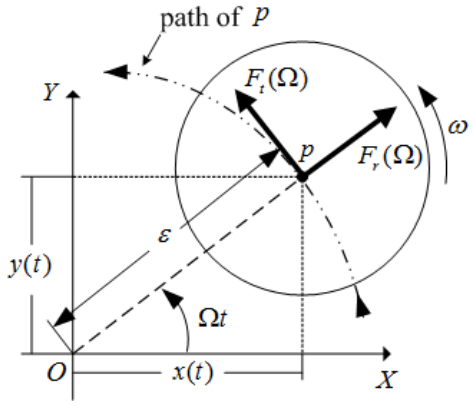

Fig. 1 Circular whirl orbit motion of the impeller

Fig. 1 illustrates typical whirling motion of rotor model which is applied in the present study. The points O and p indicate the center of the whirling orbit and the center of the impeller, respectively. The distance ε represents the dynamic eccentricity of the impeller. The shrouded impeller is whirling at the angular rate Ω, while the shroud surface spins about the center of the rotor at the spin rate ω. In ANSYS CFX, this motion is modeled by defining the fluid region as a rotating frame while the stator wall is defined as a counter rotating wall in the opposite direction to the rotating frame. To simulate positive whirling, the direction of the rotating rotor has to be same with the direction of the rotating frame.

The conventional, MCK model used to describe the fluid structure interaction forces between the shroud leakage, secondary flow path fluid and the whirling rotor is:

$$-\begin{Bmatrix} F_x(t) \\ F_y(t) \end{Bmatrix} = \begin{bmatrix} K & k \\ -k & K \end{bmatrix} \begin{Bmatrix} x(t) \\ y(t) \end{Bmatrix} + \begin{bmatrix} C & c \\ -c & C \end{bmatrix} \begin{Bmatrix} \dot{x}(t) \\ \dot{y}(t) \end{Bmatrix} + \begin{bmatrix} M & m \\ -m & M \end{bmatrix} \begin{Bmatrix} \ddot{x}(t) \\ \ddot{y}(t) \end{Bmatrix} \quad \textbf{(28)}$$

where, $x(t) = \varepsilon \cos(\Omega t)$ and $y(t) = \varepsilon \sin(\Omega t)$. In this equation, $F_x(t)$ and $F_y(t)$ are related to the radial and tangential forces by

$$\begin{aligned} F_x(t) &= \frac{F_r}{\varepsilon} \varepsilon \cos \Omega t - \frac{F_t}{\varepsilon} \varepsilon \sin \Omega t = \frac{F_r}{\varepsilon} x(t) - \frac{F_t}{\varepsilon} y(t) \\ F_y(t) &= \frac{F_r}{\varepsilon} \varepsilon \sin \Omega t + \frac{F_t}{\varepsilon} \varepsilon \cos \Omega t = \frac{F_t}{\varepsilon} x(t) + \frac{F_r}{\varepsilon} y(t) \end{aligned} \quad \textbf{(29)}$$

At $\Omega t = 0$, the location, velocity, and acceleration of the impeller center become

$$\begin{aligned} x &= \varepsilon & y &= 0 \\ \dot{x} &= 0 & \dot{y} &= \varepsilon \Omega \\ \ddot{x} &= -\varepsilon \Omega^2 & \ddot{y} &= 0 \end{aligned} \quad \textbf{(30)}$$

By substituting Eq. (30) into Eq. (28), the forces exerted on the impeller are expressed as

$$\begin{aligned} \frac{F_r}{\varepsilon} &= \frac{F_x(0)}{\varepsilon} = -K - c\Omega + M\Omega^2 \\ \frac{F_t}{\varepsilon} &= \frac{F_y(0)}{\varepsilon} = k - C\Omega - m\Omega^2 \end{aligned} \quad \textbf{(31)}$$

Once a numerical solution is obtained at a certain whirl frequency, the radial and tangential forces, F_r and F_t, can be determined by integrating the force at each node on the shroud surface. The forces can be expressed

$$\begin{aligned} F_r &= F_x(0) = \sum f_{x_i} \\ F_t &= F_y(0) = \sum f_{y_i} \end{aligned} \quad \textbf{(32)}$$

where, f_{x_i} : reaction force in X direction at each node

f_{y_i} : reaction force in Y direction at each node

The forces at each node are calculated by

$$f_{x_i} = P_i \times A_i \times n_{x_i}$$
$$f_{y_i} = P_i \times A_i \times n_{y_i} \quad \textbf{(33)}$$

where, P_i : pressure at each node , A_i : area at each node

n_{x_i} : normal vector in X direction at each node

n_{y_i} : normal vector in Y direction at each node

In Eq. (31), the impedances, F_r / ε and F_t / ε, should be obtained at least at three whirl frequencies to calculate the rotordynamic coefficients because there are 6 unknowns, the linear stiffness, damping, and mass coefficients in Eq. (28). Preferably, the rotordynamic coefficients can be evaluated using the Least Square Algorithm after obtaining impedances at many frequency ratios. To obtain solutions at multiple frequency ratios, relative rotor speed is required at each frequency ratio to impose a boundary condition of the rotor speed. The relative rotor speed is defined is defined as follows:

$$\omega_{rotor} = \omega - \Omega \quad \textbf{(34)}$$

Ω is identical rotational speed of the domain and ω_{rotor} is the relative rotor spin speed. The rotor spin speed, ω, of the shroud impellers in this research is 2000 rpm.

Table 2 shows the whirling speed and the calculated relative speed using Eq. (34) at each frequency ratio. The listed frequencies are utilized value to obtain the impedance curves of the shrouded centrifugal impellers as shown in Fig. 8.

Table 2 Whirling speed and relative rotor speed ($\omega = 2000\,rpm$)

Frequency ratio (f = Ω/ ω)	0	0.25	0.5	0.75	1	1.5
Ω (rpm)	0	500	1000	1500	2000	3000
ω_{rotor} (rpm)	2000	1500	1000	500	0	-1000

To simulate multi domain problems with rotating frames, interface model is required. In this study, Frozen Rotor model will be used to capture circumferential flow variation. Since speeds of each domain are not same, mesh connection method is need to be set as GGI (general grid interface) and this model does not require matching nodes on either side of two connected surfaces.

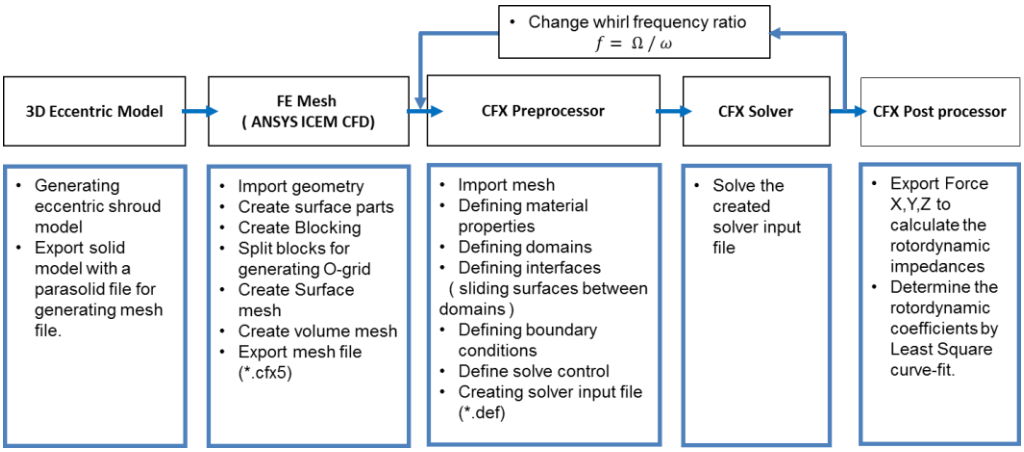

Fig. 2 Overall work flow for dynamic impedance and dynamic coefficient determination

Fig. 2 illustrates the overall computation procedure to calculate the rotordynamic impedances and coefficients. The numerical solution process is performed over a wide whirl frequency range for use in both imbalance response and rotordynamic stability codes. The frequency response results are used to calculate the rotordynamic coefficients

using the method of least square error. Thus, by varying the precession frequency ratio as shown in Table 2, the preprocessing and solving step is repeated as shown in the figure.

2.7 Mesh Generation and Boundary Conditions

Fig. 3 shows geometric and dimensional information for the face seal impeller and a conventional wear-ring seal impeller, which is used for the CFD simulations.

Dimensions in each impeller model are indicated based on the information in [8, 12]. In case of the face-seal impeller, some of the dimensions of the leakage flow path in the shroud model had to be approximated because the exact geometry information is unclear in the references.

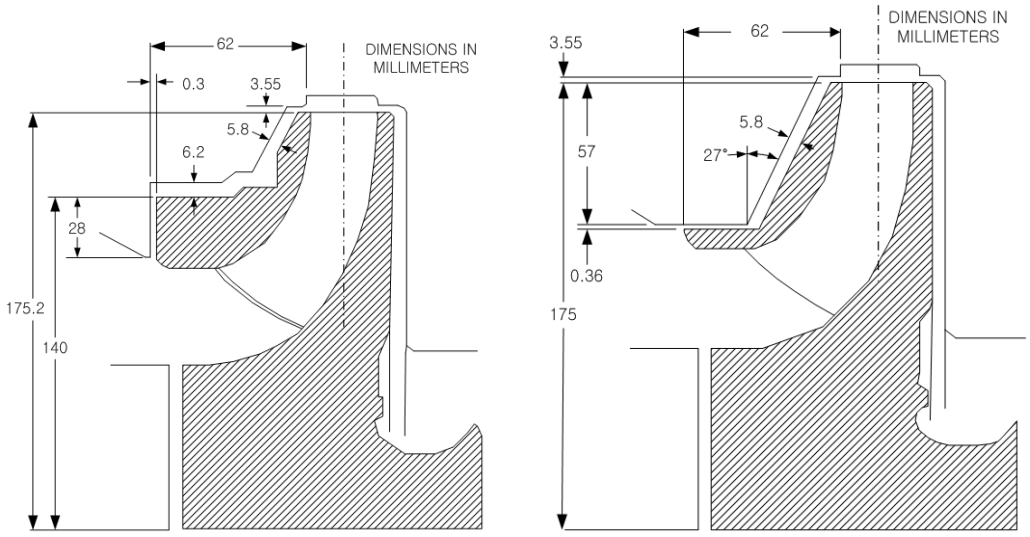

(a) (b)

Fig. 3 Nominal configuration of impeller (a) face-seal impeller [8] (b) Wear-ring seal impeller [8]

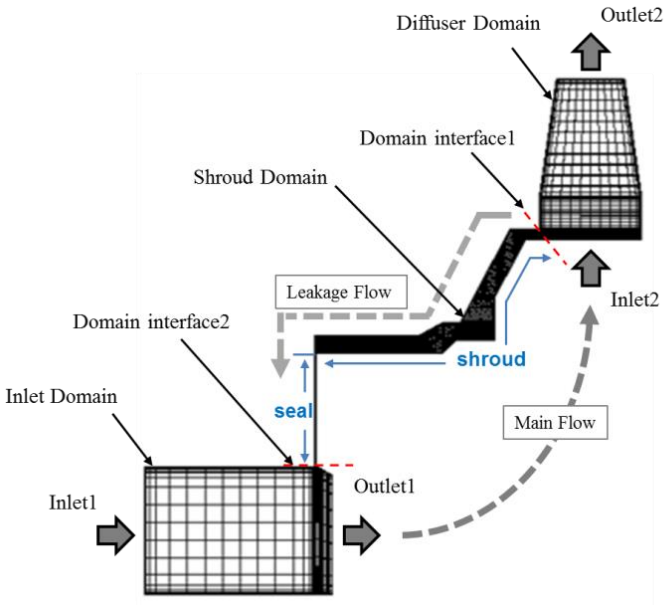

(a)

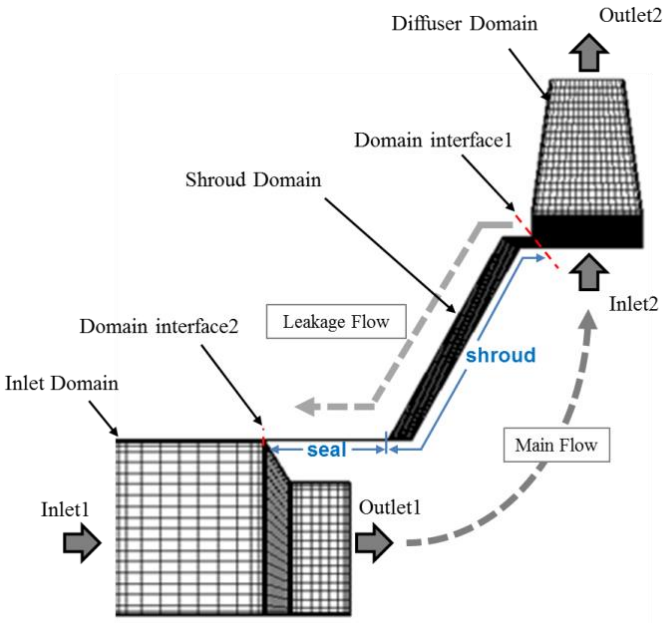

(b)

Fig. 4 Cut plane view of 3D eccentric grid (a) face-seal impeller (b) wear-ring seal impeller

Based on the dimensions in Fig. 3, 3D eccentric grid models for the face-seal impeller and the conventional wear-ring seal impeller are generated. Fig. 4 describes the cut plane view of the 3D eccentric grid models of the impeller. The goodness of the 3D eccentric mesh will be evaluated using the mesh density studies in the following sections.

The impeller models are composed of three domains as shown Fig. 4. The diffuser domain in each numerical model is added to impose the inlet swirl velocity on the secondary flow path, which can be set in the computational model by defining the domain as a rotating frame. Two surfaces located between domains are set as domain interfaces to define domains rotating at different spin rates. The numerical impeller models have 2 inlets and 2 outlets and they are placed in the diffuser and inlet domains as shown in Fig. 4. The same mass flow rate should be imposed at the two inlets since the omitted primary flow passage is a continuous flow path. The outlet pressures are determined based on the head rise at the main flow region. Based on the operating conditions provided in the research of Bolleter et al. [2], the boundary conditions at $\Omega = 0$ are specified as shown in Table 3, where Ω is the whirl velocity as shown in Fig. 1. Stationary walls in the rotating frames are treated as counter rotating walls and a no-slip condition is imposed at all walls in the numerical model. For the numerical calculation, a 64 bit processor with 4 cores operating at 28GHz and 8 GB memory are utilized and the desired convergence target of each solution is 10^{-4} or an even lower value.

Table 3 Boundary conditions for the shrouded impeller model at $\Omega = 0$

Parameters	Values
Working Fluid	Water
Fluid Temperature	26.5°
Inlet Swirl Ratio	0.5
Flow rate at Inlet1	130 Kg/s
Flow rate at Inlet2	130 Kg/s
Static Pressure at Outlet1	0.1 MPa
Static Pressure at Outlet2	0.57 MPa
Stationary walls	Counter Rotating Wall
Rotating walls	2000 rpm

2.8 Validity of Axisymmetric Pressure Boundary Condition

Constant pressure boundary condition at Outlet2 is assumed for the shrouded only impeller model as indicated in Table 3. If a centrifugal impeller is installed in an asymmetric volute, the constant pressure at the outlet of the impeller is need to be justified when considering asymmetric shape of the volute. Alemi et al. [41] investigated the effect of a volute on a centrifugal pump. They measured pressure along the circumferential direction at the impeller outlet as shown in Fig. 5. The measured data were compared with the predictions using various types of turbulence model provided in ANSYS CFX. The compared results are indicated in Fig. 6. The measurement and the predictions showed that deviation of the pressure along the circumferential direction at impeller outlet is small enough to assume constant pressure boundary condition.

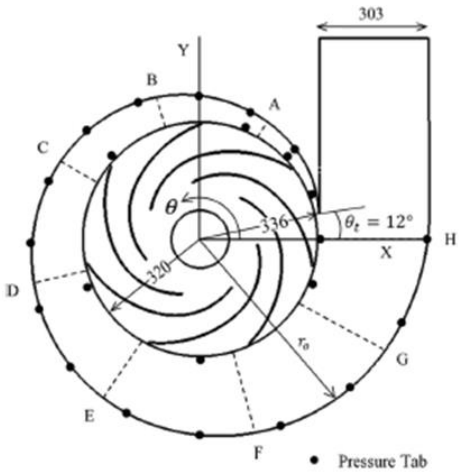

Fig. 5 Asymmetric volute and impeller geometry [41]

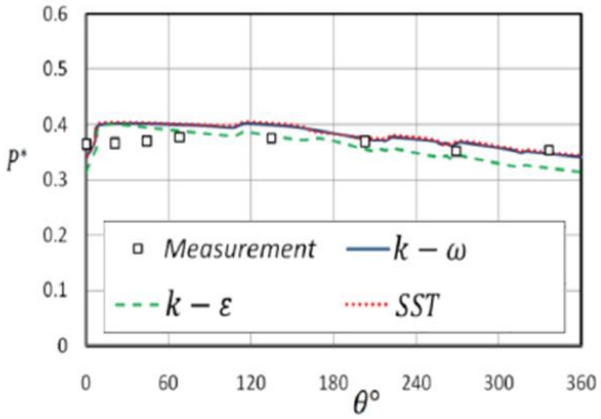

Fig. 6 Comparison of pressure at outlet of impeller between measurement and predictions [41]

2.9 Grid Independence Study

2.9.1 Face Seal Impeller of Fig. 3(a)

The 3D eccentric grid model of the face-seal impeller of Fig. 3(a) does not include the primary passage as shown in Fig. 4 (a) because the exact geometry information of

the impeller blade is unavailable. Thus, the 3D shroud only model which was utilized in the previous CFD research [10, 12] is used to determine the rotordynamic coefficients.

Three grid models (coarse, medium, and fine) are constructed to determine the appropriate mesh size for the rotordynamic predictions. The sizes of the coarse, medium, and fine mesh are 0.46×10^6, 0.82×10^6, and 1.61×10^6 nodes, respectively. Fig. 7 shows the predicted impedances for the three grid models. The results of the medium grid and the fine grid model are almost identical and the coarse grid result has negligible differences from other grid models. Moreover, when considering the fact that a grid model with 187,800 nodes in the previous study [12] could predict reliable solutions for the face-seal impeller case, the fine grid of Fig. 7 can be considered enough to determine the fluid induced forces.

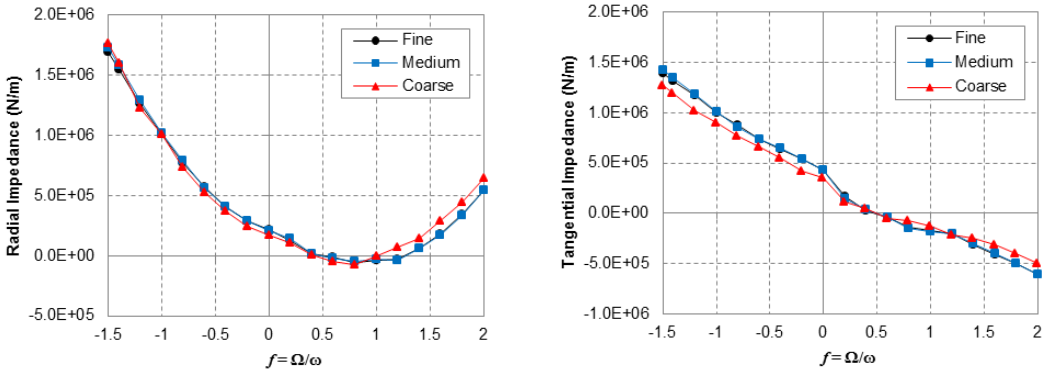

(a) (b)

Fig. 7 Influence of grid density on impedance curves of face-seal impeller (a) radial (b) tangential

A wide range of the precession frequency ratios (PFR, $f = \Omega / \omega$) is investigated in Fig. 7 to check the existence of the bump and dip which were observed in the bulk

flow analysis by Childs [8]. Slight bump and dip are observed in the calculated impedances for all grid models as shown in Fig. 7. The computed results of Fig. 7 can be reasonably curve fit to Eq. (31) to obtain the rotordynamic coefficients because the magnitudes of the bump and dip are small enough to ignore.

The predicted results for fine mesh are compared to the results of previous studies in Fig. 8 and Table 4. The precessing frequency of the compared impedances of Fig. 8 is ranging from 0 to 1.5. The calculated direct and cross-coupled stiffness are under-predicted and the direct damping is somewhat over-predicted when compared to the experiment results. However, when considering the fact that geometry approximations had to be made for constructing the current face-seal impeller model, the overall results show reasonable agreement with the experimental data.

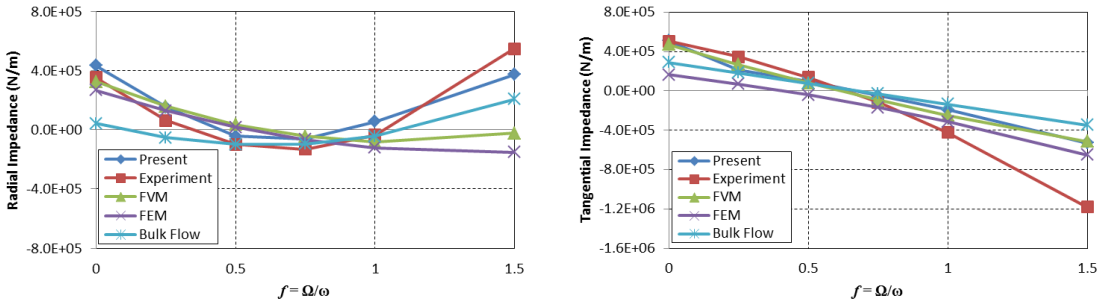

(a) (b)

Fig. 8 Predicted impedances for the comparison with the previous predicted and measured results (a) radial (b) tangential

Table 4 Calculated rotordynamic coefficients for the face-seal shrouded impeller

	K (N/m)	c (N-s/m)	M (kg)	k (N/m)	C (N-s/m)	m (kg)	$\frac{k}{C\omega}$
Present Model	-2.50E+05	3.58E+03	1.01E+01	4.10E+05	4.35E+03	-6.06E+00	0.45
FVM[12]	-3.24E+05	3.59E+03	7.92E+00	4.71E+05	4.05E+03	-2.92E+00	0.56
Experiment [3]	-3.53E+05	6.80E+03	2.36E+01	5.06E+05	2.58E+03	8.85E+00	0.94
FEM [10]	-2.68E+05	2.92E+03	5.03E+00	1.65E+05	1.64E+03	3.03E+00	0.48
Bulk Flow Model [8]	-4.20E+04	2.29E+03	8.96E+00	2.88E+05	2.02E+03	-9.00E-03	0.69

The effect of the inlet swirl ratio on the face-seal impeller is investigated in Fig. 9 to determine its influence on the impedance curves. The y-intercepts of the impedance curves are increasing and therefore by eq. (1) the absolute values of the direct and cross-coupled stiffness are increasing as the intensity of the inlet swirl at the shroud entrance becomes larger. Small deviations from the forms in eq. (1) can be seen and their magnitudes are increasing at higher ISR. However, the magnitudes of the bump and dip are smaller than the predictions of Childs [8] and the shapes of the peaks are quite different.

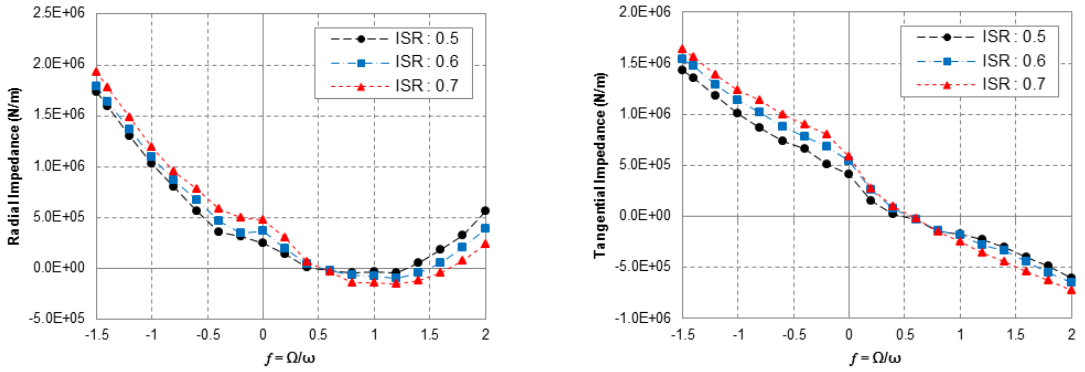

(a) (b)

Fig. 9 Impedances for the face-seal impeller according to ISR (a) radial (b) tangential

2.9.2 Conventional Wear-Ring Seal Impeller of Fig. 3(b)

In this section, a mesh density study is performed to obtain reliable results and determine optimal grid model for the calculation of the impeller reaction forces. Table 5 shows the grid models for the mesh density study and the corresponding calculation time per precession frequency ratio. The grid model is defined as a coarse grid in cases of less than a million nodes. CFD calculations are implemented and the leakage flow rates are compared in Fig. 10. As shown in the figure, no noticeable changes are observed for the grid models over 800,000 nodes and the difference between the medium and fine grid is only 0.5 %. Fig. 11 shows a comparison of the impedances for the various grid models. In cases of Coarse1 and Coarse2, the calculated impedances have some significant differences when compared to the other cases. The results of the medium and fine grid are almost identical. Based on the results, the CFD solutions for the fine grid can be considered as converged results and therefore the fine grid model is selected for the simulation in this paper.

Table 5 Comparison of grid models of the wearing seal impeller

Grid Model	No. of Nodes	Calculation Time for PFR = 0
Fine	1949568	5.123×10^{3} sec
Medium	1310836	3.827×10^{3} sec
Coarse1	810768	2.640×10^{3} sec
Coarse2	224200	8.722×10^{2} sec
Coarse3	159488	6.942×10^{2} sec

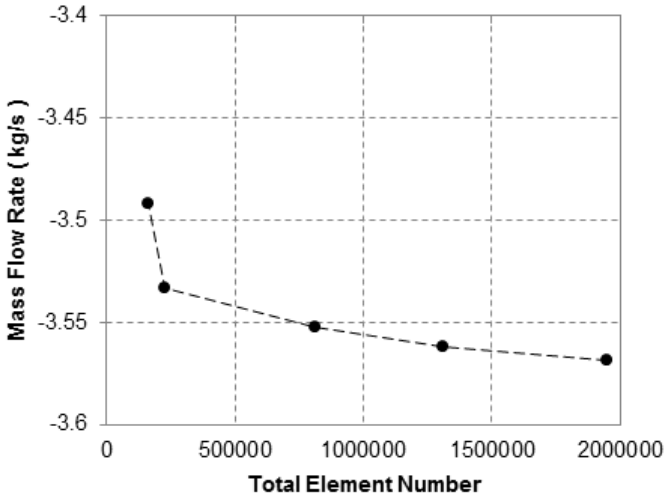

Fig. 10 Leakage flow rate at seal outlet of the wear-ring seal impeller

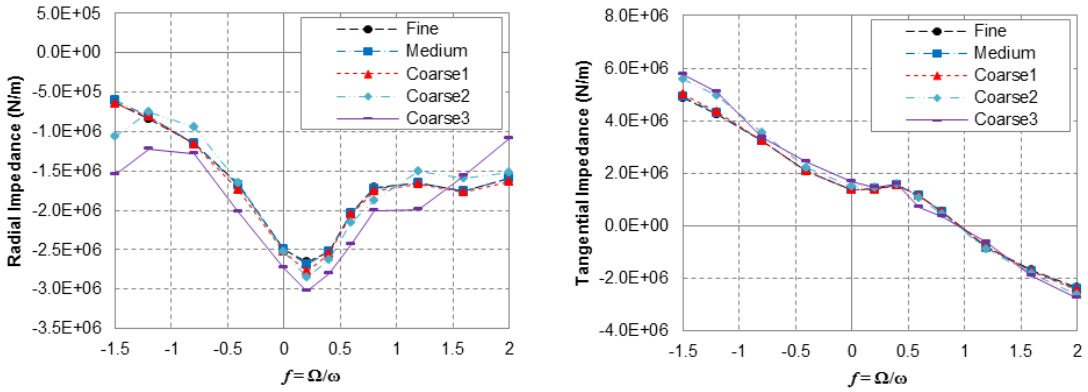

(a) (b)

Fig. 11 Influence of grid density on impedance curves of the wear-ring seal impeller (a) radial (b) tangential

3. ROTORDYNAMIC ANALYSIS ON SHROUDED CENTRIFUGAL IMPELLER

3.1 Impedances of Conventional Wear-Ring Seal Impeller

Fig. 4(b) shows the 3D eccentric grid of the conventional wear-ring seal impeller of Fig. 3(b). This model is also constructed without blade region and has three domains like the face-seal impeller case. And the detailed boundary conditions used for the numerical simulation of the conventional wear-ring seal are the exactly those of the face seal impeller case. The shroud domain of the wear-ring seal impeller is divided into 2 sections: seal and shroud as shown in Fig. 4 (b), in order to evaluate the fluid induced forces on the seal and shroud surface separately. Fig. 12 and Fig. 13 show the predicted radial and tangential impedances of combined (seal + shroud), shroud, and seal versus the precession frequency ratio, which ranges from -1.5 to 2.0. The radial and tangential impedances in the figures have the dip and bump shapes in the frequency ratio range 0 to 0.5. The predicted impedance curves for the shroud of the wear-ring seal impeller in Fig. 12(b) and Fig. 13(b) have similar trends with the bulk flow results of Childs [8]. The peaks are clearly present in the computed curves and the magnitudes of the bump and dip are increasing at higher ISR. Fig. 12(c) and Fig. 13(c) indicate the computed radial and tangential impedances for the wear-ring seal of the impeller model. The seal results show relatively small bump and dip when compared to the values of the shroud. In case of the tangential impedance, the fluid induced forces on the shroud contribute most for generating the bump in the curves. Generally, the x-intercept of the tangential impedance

curve can be defined as the whirl frequency ratio at instability, $\Omega_w = k/C\omega$, if the curve is approximately linear. With higher Ω_w, the impeller is more destabilizing. In Fig. 13(a), the x-intercept of the tangential impedance has a higher value for increased ISR and thus it can be concluded that the impeller tends to be more destabilizing at higher ISR. The same phenomenon could be observed in the results of the bulk flow model by Childs [8].

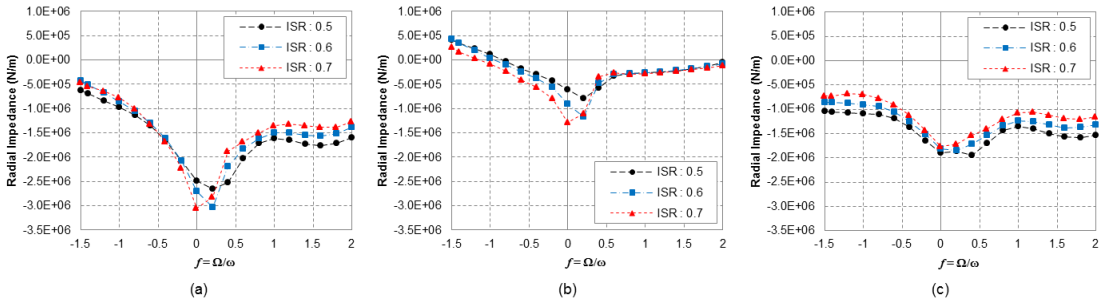

Fig. 12 Radial impedances for the wear-ring seal impeller according to the inlet swirl ratio (a) combined (shroud + seal) (b) shroud (c) seal

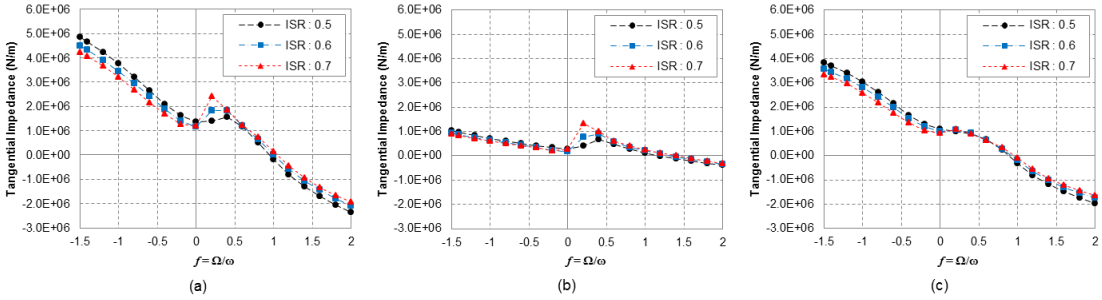

Fig. 13 Tangential impedances for the wear-ring seal impeller according to the inlet swirl ratio (a) combined (shroud + seal) (b) shroud (c) seal

The peaks in the impedance curves of the centrifugal impeller could be also observed clearly in the past experimental results from the Caltech program by Franz et al. [15]. In that paper, the tangential and radial impedances of centrifugal impeller had been measured by varying the flow rate of the primary passage with constant speed and

the several types of volutes and impellers. They investigated the influence of the flow rate on the rotordynamic instability and concluded that the volute had impact on the hydrodynamic force for high flow rates and the shape of the tangential force curve and the destabilizing force were affected by the flow rate. The same phenomenon was observed in the experiment by Brennen et al. [16]. In their research, the bump and dip were also shown in the measured forces at low flow coefficients and the authors concluded that the impedance bump and dip were independent of volute type.

3.2 Effect of Main Flow Rate

Franz et al. [15] evaluated the effect of flow coefficients and found that the shape of the force curves was influenced by the flow coefficients. In this section, a 3D numerical model of the conventional wear-ring seal impeller is employed to determine the dependence of impedances on flow rate through the primary passage. The flow rates of the primary passage are used as inlet boundary conditions for the numerical solutions of the face-seal impeller and the conventional wear-ring seal impeller in the present study. The boundary conditions are indicated in Table 3. In order to evaluate the effect of the flow rate on the wear-ring seal impeller, the flow rates on inlet boundary conditions are changed. The flow rate is changed from 130kg/s to 250kg/s and 300kg/s. Note that the static pressures are assumed to be constant for the cases.

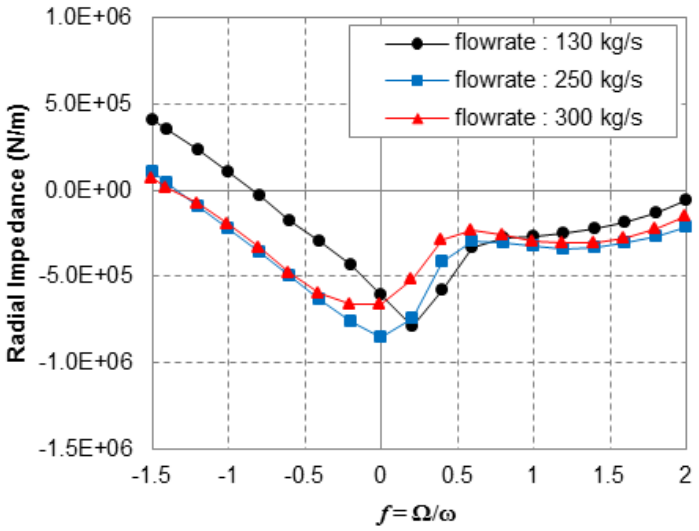

(a)

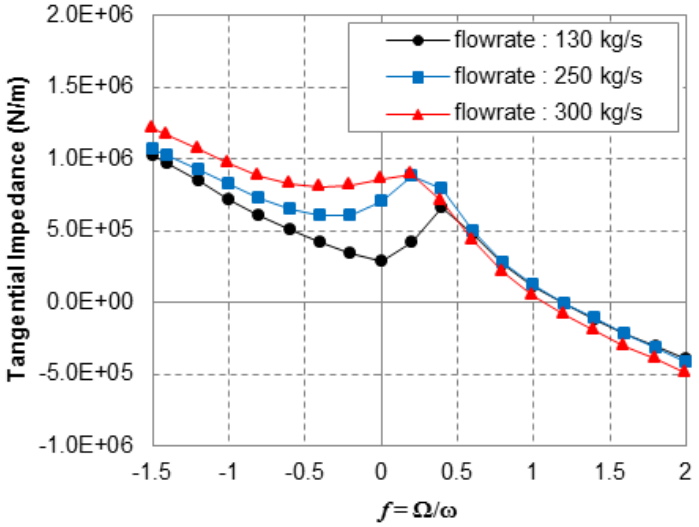

(b)

Fig. 14 Impedances on the shroud for three flow rates of the primary passage (a) radial (b) tangential

Fig. 14 shows the computed impedance curves according to the flow rate in the primary passage. In the results, it is observed that as the main flow rate increases, the shape of the bump and dip in the impedance curves changes. In case of the radial

impedance in Fig. 14(a), the magnitude of the bump in the curve becomes smaller with lowered flow rate. Fig. 14(b) describes the computed tangential impedances according to the flow rate. At the highest flow rate, the y-intercept of the tangential impedance has the largest value and the x-intercept has the smallest value. This tendency of the current numerical solution is identical to the measured data from Franz et al. [15] and it can be concluded that the wear-ring seal impeller is viewed as being less destabilizing at lower flow rate.

3.3 Effect of Shroud Leakage Path Shape

Childs [8] explained that the bump and dip in the impedance curves computed by the bulk flow analysis appear because of a centrifugal acceleration term in the path-momentum equation. He explained that the peaks substantially decreased when the term was removed in the path-momentum equation of the bulk flow model. The bulk flow centrifugal acceleration term was defined as follows:

$$\frac{2u_{\theta 0}}{r}\frac{dr}{ds}/b^2 \tag{35}$$

where, $u_{\theta 0}$ is the circumferential velocity, and r, s, and b are the non-dimensional variables of the inlet radius, path length, and velocity ratio in reference [8].

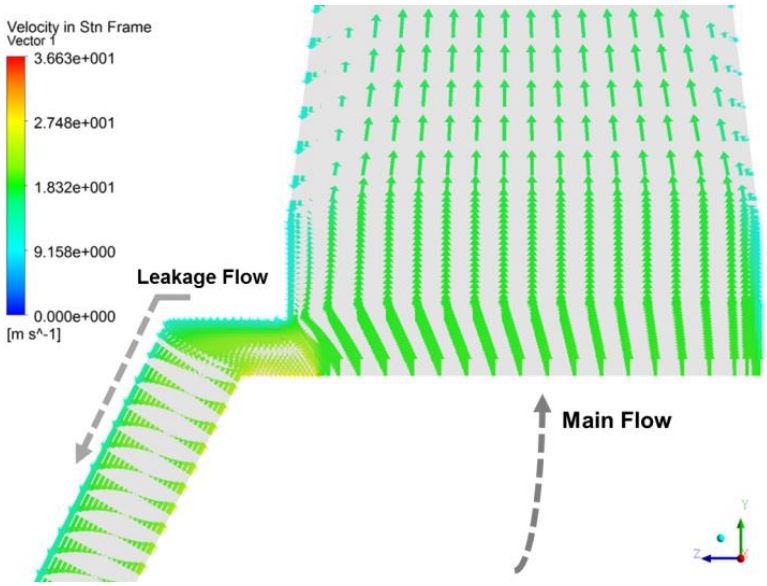

(a)

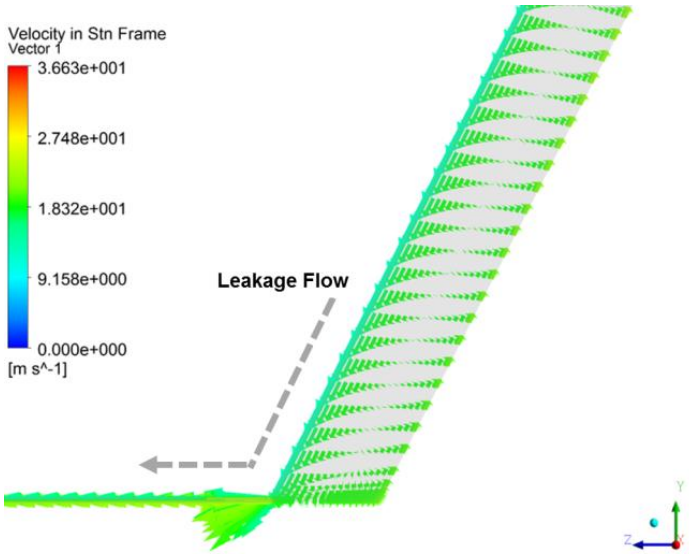

(b)

Fig. 15 Velocity vector plots of the wear-ring seal impeller at (a) shroud entrance (b) seal inlet

The centrifugal acceleration effect in the shroud region is visualized in the vector plot near the shroud surface as indicated in Fig. 15. In the figure (a) and (b), the fluid

flow near the shroud surface of the impeller is pushed up while the fluid near the stator wall flows to downward due to the pressure difference between the shroud entrance and the outlet of the wear-ring seal.

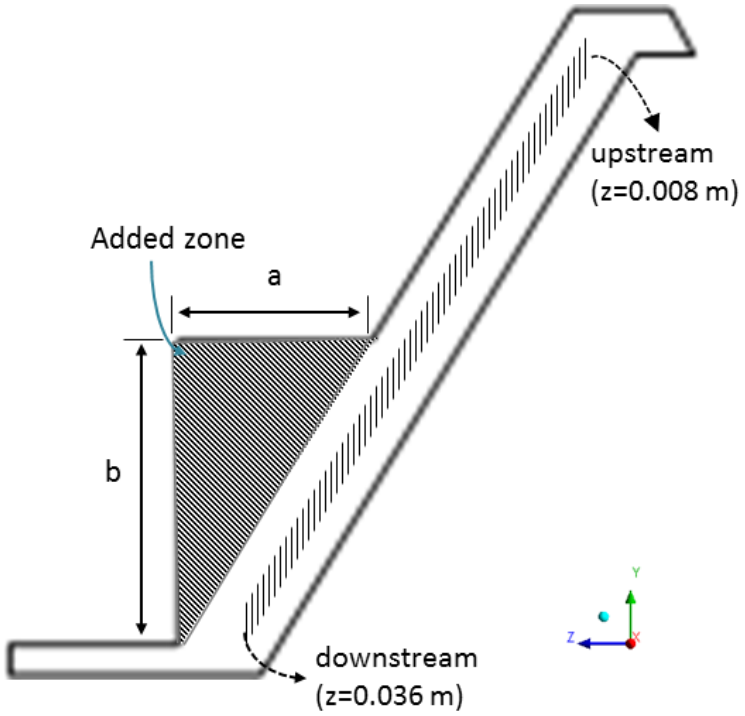

Fig. 16 Modified shroud geometry on stator-side

In eq. (35) , the circumferential velocity term is one of the factors that has an influence on the centrifugal acceleration. Thus, reducing the velocity near the shroud wall can make the centrifugal acceleration decrease. In order to reduce the velocity of the reverse flow near the shroud surface, the geometry of the shroud region is changed as illustrated in Fig. 16. Additional recirculation zones are added by assuming that strong recirculation in the shroud region can slow down the velocity of the reverse flow and circumferential velocity. Three cases referred to as A1, A2, and A3 are considered to

evaluate the effect of the added zone on the impedance curves of the wear-ring seal impeller model. The widths and heights of the cases are shown in Table 6. CFD models are constructed and the flow fields of the models are calculated using these parameter values.

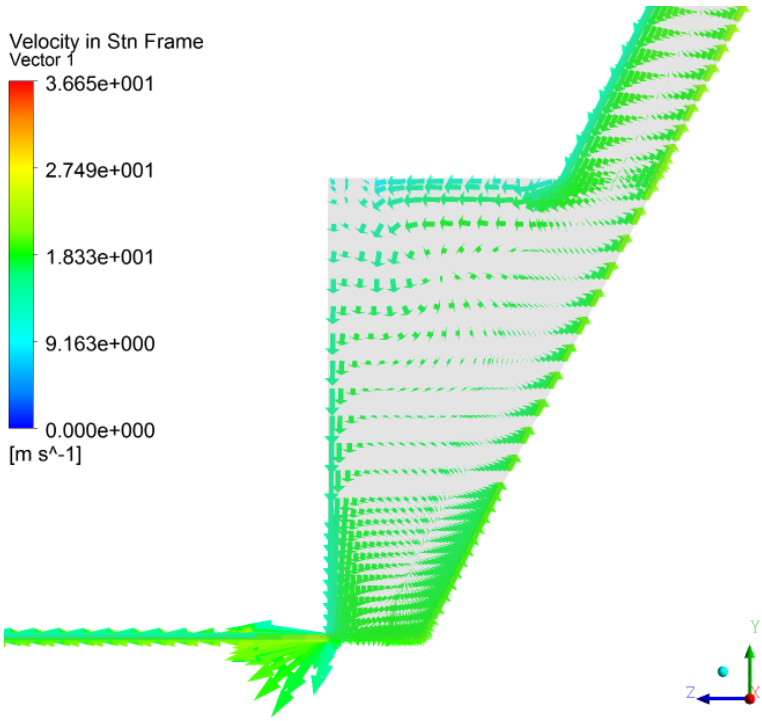

Fig. 17 Vector plots in the added recirculation zone (A2)

Table 6 Dimensions of added zones on the shroud leakage path

	A1	A2	A3
a (mm)	10.2	15.3	20.4
b (mm)	20.0	30.0	40.0

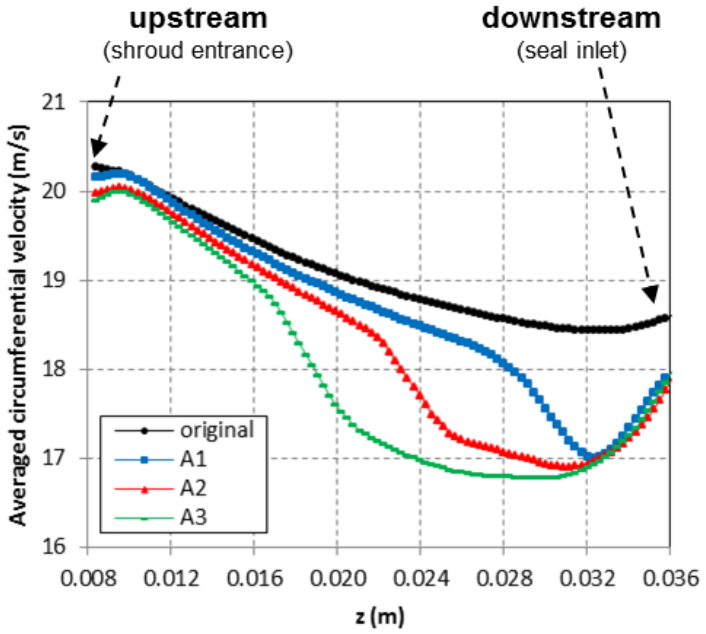

Fig. 18 Averaged circumferential velocity according to the shape of shroud

Fig. 17 shows the recirculation flow in the added zone (A2). The averaged circumferential velocity along the z-axis of the entire shroud region is obtained for the changed shroud cases and the original shroud case. The sampled region to obtain the averaged circumferential velocity for all compared cases is indicated in Fig. 16. A comparison of the averaged circumferential velocity is made in Fig. 18. The averaged circumferential velocity in the shroud region decreases as the area of the added zone increases. Since the clearance near to the shroud entrance is same, the effect of the added area is relatively small and therefore the velocity differences of all the cases could be considered negligible. However, the velocity differences around the enlarged shroud zone are large enough to have an influence on the shear stress on the shroud surface.

Table 7 Comparison of leakage flow rate according to the size of the added zones

	Added zone			
	original	A1	A2	A3
Leakage (kg/s)	3.5685	3.2350	3.2344	3.2549

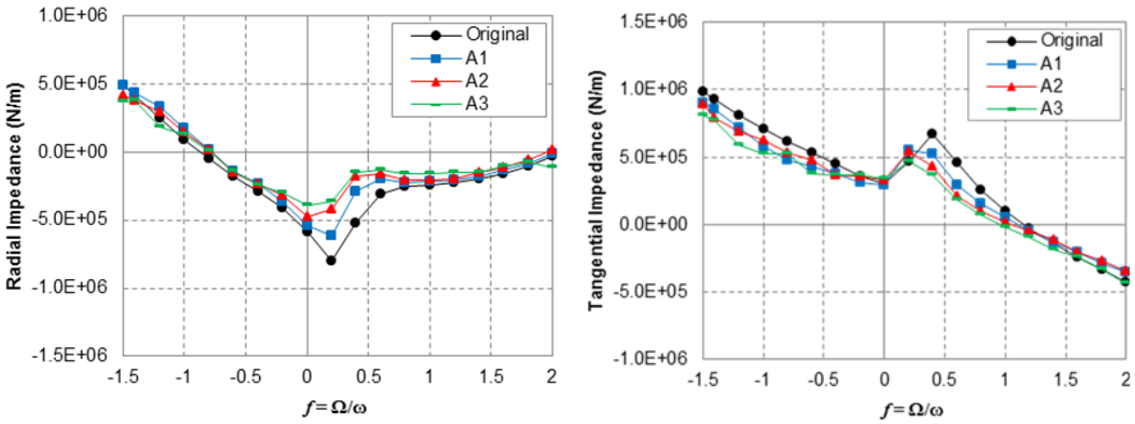

(a) (b)

Fig. 19 Impedances on the shroud according to the secondary flow path geometry (a) radial (b) tangential

In order to check the effect of the added zone on the shroud leakage path, the radial and tangential impedances of the shroud are compared according to the size of the added zone including the original wear-ring seal impeller model in Fig. 19. Adding the recirculation zone reduces the magnitude of the bump and dip in the impedance curves and the cross coupled stiffness. Increasing the area in the shroud region further reduces the peaks in the impedance curves. Reducing the velocity in the leakage flow path is effective for decreasing the peaks from the impedance predictions and modifying the shroud shape is one possible solution to reduce the circumferential velocity and

centrifugal acceleration. The leakage flow rate is reduced by about 10 % when the additional recirculation zone is added as indicated in Table 7. However, no noticeable change of the leakage flow rate is shown as the area in the shroud leakage path is increased from A1 ($102\,mm^2$) to A3 ($408\,mm^2$).

3.4 Effect of Seal Clearance

This section investigates the effect of the wear ring, end-seal clearance on impedances. The selected seal clearances for the comparison are 0.36, 0.54, and 0.7mm. The imposed boundary conditions for the simulations are assumed to be the same for all cases. The computed results are described in Fig. 20 and Fig. 21. Like the previous cases in this paper, the shroud has a relatively larger contribution as a cause for the bump and dip in the impedance curves. In case of 0.36mm, the phenomenon can be seen clearly and the peaks disappear with the increased seal clearance as shown in Fig. 20(b) and Fig. 21(b). The y-intercepts of the radial and tangential impedances in Fig. 20(c) and Fig. 21(c) decrease when the seal clearance is increasing. If assumed that the impedances are approximately modeled using Eq.(37), the decreased y-intercepts in impedance curves imply reduced direct stiffness and cross-coupled stiffness, respectively. The same trend was predicted for the conventional wear-ring seal impeller by the bulk flow analysis of Childs **[8]**.

Table 8 indicates the leakage flow rate increases more than proportionately as the wear-ring seal clearance increase.

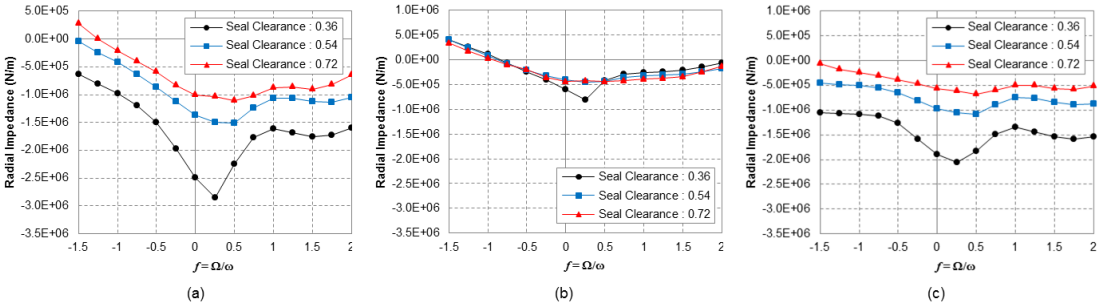

Fig. 20 Radial impedances for the wear-ring seal impeller according to the seal clearance (a) combined (shroud + seal) (b) shroud (c) seal

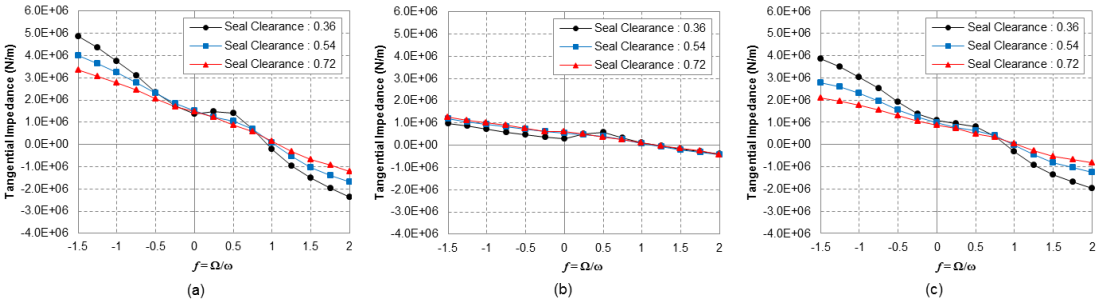

Fig. 21 Tangential impedances for the wear-ring seal impeller according to the seal clearance (a) combined (shroud + seal) (b) shroud (c) seal

Table 8 Comparison of leakage flow rate according to the seal clearance

	Seal Clearance		
	0.36	0.54	0.72
Leakage (kg/s)	3.5685	6.6498	9.5105

4. STABILITY ANALYSIS WITH FINITE ELEMENT MODEL[4]

4.1 Finite Element Rotordynamic Model

Fig. 22 shows the configuration of a FE rotor model with the conventional wear-ring seal impeller analyzed. In the FE model, the shaft has 5 beam elements on both sides and the disk has 2 beam elements. In the FE analysis, it is assumed that the impeller force from the lateral motion of the impeller is acting on the center where the position is located at the 7th node (center node) in the model of Fig. 22. The system is supported by the flexible bearings placed at both ends. The bearing coefficients and geometry demensions of the FE rotor model are indicated in Table 9.

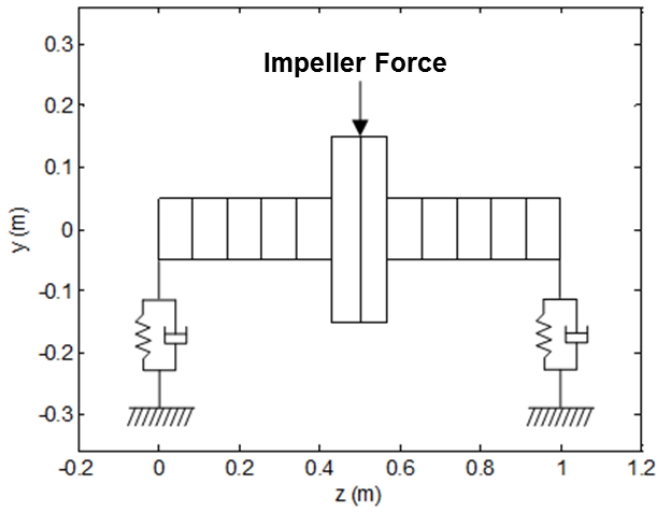

Fig. 22 Finite element model of rotor-bearing system

[4] Reprinted in Part with permission from "Rotordynamic Force Prediction of a Shrouded Centrifugal Pump Impeller-Part I : Numerical Analysis," by Eunseok Kim and Alan Palazzolo, J. Vib. Acoust. 2016; 138(3), p. 031014. © 2016 ASME.

Table 9 Parameters of the Rotor-Bearing Model

Parameters	Values
Young's modulus (Pa)	2×10^{11}
Density (kg / m^3)	8000
Length of shaft (m)	1.0
Length of disk (m)	0.14
Diameter of shaft (m)	0.1
Diameter of disk (m)	0.3
Unbalance eccentricity of disk (m)	0.36×10^{-4}
Bearing stiffness (N / m)	1.5×10^{6}
Bearing damping (Ns / m)	2×10^{3}

4.2 Synchronous Unbalance Response Analysis

The free body diagram of the wear-ring seal impeller is shown in Fig. 1. The point O in Fig. 1 indicates the center of the whirling orbit and the point p represents the center of the rotating impeller. The finite element model of Fig. 22 is expressed mathematically as

$$[M]\{\ddot{z}\}+[C]\{\dot{z}\}+[K]\{z\}=\{F_u\}+[F_I] \tag{36}$$

where at node i, the displacement vector, $\{z_i\}$, is expressed as

$$\{z_i\}=\{x_i \quad \theta_{xi} \quad y_i \quad \theta_{yi}\}^T \tag{37}$$

The $[F_I]$ of Eq. (36) is an impeller force vector acting on the disk of Fig. 22. An element vector of $[F_I]$ at node No.7 can be expressed with mass, damping, and stiffness matrices and it has a form of

$$[F_{I7}] = -\begin{bmatrix} M & 0 & m & 0 \\ 0 & 0 & 0 & 0 \\ -m & 0 & M & 0 \\ 0 & 0 & 0 & 0 \end{bmatrix} \begin{Bmatrix} \ddot{x}_7 \\ \ddot{\theta}_{x7} \\ \ddot{y}_7 \\ \ddot{\theta}_{y7} \end{Bmatrix} - \begin{bmatrix} C & 0 & c & 0 \\ 0 & 0 & 0 & 0 \\ -c & 0 & C & 0 \\ 0 & 0 & 0 & 0 \end{bmatrix} \begin{Bmatrix} \dot{x}_7 \\ \dot{\theta}_{x7} \\ \dot{y}_7 \\ \dot{\theta}_{y7} \end{Bmatrix} - \begin{bmatrix} K & 0 & k & 0 \\ 0 & 0 & 0 & 0 \\ -k & 0 & K & 0 \\ 0 & 0 & 0 & 0 \end{bmatrix} \begin{Bmatrix} x_7 \\ \theta_{x7} \\ y_7 \\ \theta_{y7} \end{Bmatrix} \quad \textbf{(38)}$$

and $[F_{Ii}]$ is zero at the other nodes. By assembling the mass, damping, and stiffness matrices with 4×4 zero matrices for other elements, $[F_I]$ of the Eq. (36) can be derived in the form of a global matrix equation to utilize in the stability analysis.

For circular and synchronous whirl motion of Fig. 1, the whirl orbit is defined as

$$\begin{aligned} x_i &= \varepsilon_i \cos \Omega t \\ y_i &= \varepsilon_i \sin \Omega t \end{aligned} \quad \textbf{(39)}$$

and the whirl frequency equals the spin frequency

$$\Omega = \omega \quad \textbf{(40)}$$

The circular motion constraint in Eq. (39) is consistent with the assumptions in part I but in practice is typically relaxed to model arbitrary motions in rotordynamic unbalance response, transient and stability simulations. In Eq. (36), $[F_I]$ is the impeller forces matrix and $[F_u]$ is the unbalance force vector of the FE model. $[M]$, $[C]$, and $[K]$

represent a global mass, damping, and stiffness matrix. The $[C]$ matrix and the $[K]$ matrix are defined as

$$\begin{aligned}[C] &= [C_B] + [C_G] \\ [K] &= [K_B] + [K_S]\end{aligned} \tag{41}$$

where B indicates bearing, G indicates gyroscopic and S indicates shaft.

For a steady state solution, it's assumed that

$$\begin{aligned}\{z\} &= \{\tilde{z}\} e^{i\Omega t} \\ \{F_u\} &= \{\tilde{F}_u\} e^{i\Omega t}\end{aligned} \tag{42}$$

Substitute Eq. (42) into Eq. (36), and divide by $e^{i\Omega t}$ to obtain

$$\left(-\Omega^2 [M] + i\Omega [C] + [K] - [F_I]\right)\{\tilde{z}\} = \{\tilde{F}_u\} \tag{43}$$

Define

$$[A] = -\Omega^2 [M] + i\Omega [C] + [K] - [F_I] \tag{44}$$

and the synchronous whirl coordinate of the FE model can be determined by

$$\{\tilde{z}\} = [A]^{-1} \{\tilde{F}_u\} \tag{45}$$

In order to obtain synchronous unbalance response, the impeller impedances at PFR=1 are required , and also over a frequency range if an M-K-C approach is utilized. This must be repeated at many different spin speeds and the corresponding boundary

conditions for the CFD analysis must be changed at each spin speed. The next section discusses the appropriate treatment of boundary conditions as spin speed varies.

4.3 Calculation of Boundary Conditions

To calculate impedances at multiple spin speeds using CFD approach, boundary conditions of the inlet and outlet at different spin speed have to be determined properly since the blade region is not included in the current CFD model of Fig. 4(b). The boundary conditions are mass flow rate of the primary passage of the impeller and pressure difference, ΔP , between the shroud entrance and the seal exit.

A flow coefficient and head coefficient are employed [42] to obtain the boundary conditions vs. rotor spin speed. For the calculation of the boundary conditions, it is assumed that the wear-ring seal impeller runs at the same design point, BEP (Best Efficient Point).

The head coefficient is expressed by

$$\text{Head coefficient : } \psi = \frac{gH}{N^2 D_I^{\,2}} \tag{46}$$

where, H , N , and D_I indicate head(m), spin speed(rad / s), and diameter(m) of the wear-ring seal impeller, and the flow coefficient is defined as below:

$$\text{Flow Coefficient : } \phi = \frac{Q}{N D_I^{\,3}} \tag{47}$$

In Eq. (47), Q (m^3 / s) is the flow rate in the main flow passage of the wear-ring seal impeller model. To determine the boundary conditions of the impeller model, the head and flow coefficients need to be calculated first based on the operating condition of the wear-ring seal impeller. The operating conditions are shown in Table 10 as obtained from [2, 8].

Table 10 Operating conditions of the conventional wear-ring seal impeller

Parameters	Values
Working fluid	Water
Density (kg / m^3)	1,000
Spin speed (rad / s)	209.44
Head (m)	68
Diameter (m)	0.35
Flow rate (m^3 / s)	0.130

Table 11 Calculated boundary conditions at multiple spin speeds

Spin Speed (rad/s)	104.72	209.44	314.16	418.88
Q (kg/s)	65.10	130.21	195.31	260.41
ΔP (MPa)	0.12	0.47	1.05	1.87

The computed head and flow coefficients from the operating conditions are $\psi = 0.124, \phi = 0.0145$, respectively. Based on these values, each operating condition is calculated as indicated Table 11. The flow rates are converted from m^3 / s to *Kg/s* by

multiplying by the density of water. The impedances curves of the impeller at different spin speed are calculated and compared in Fig. 23. The sizes of the bump and dip in the impedances increase as the spin speed of the impeller increases. At lower spin speed case, the bump and dip in the impedance curves still exist although their magnitudes are relatively small.

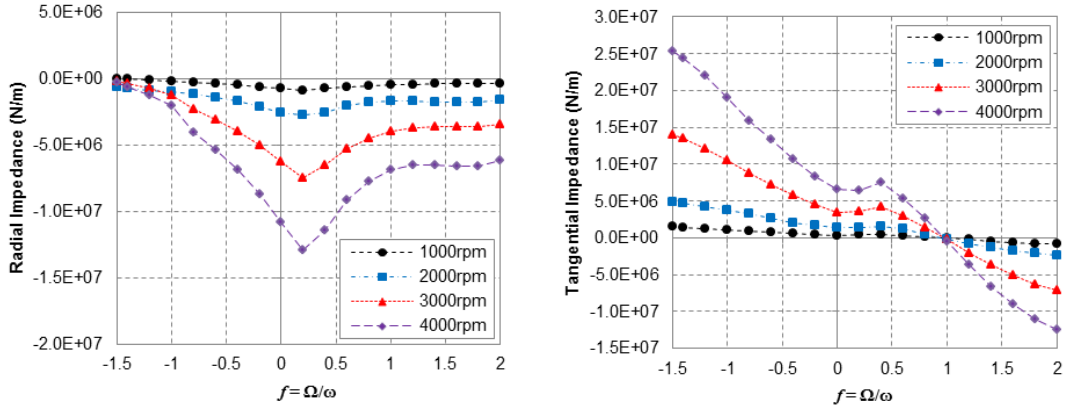

(a) (b)

Fig. 23 Impedance curves at multiple spin speeds

The quadratic least square curve-fit to calculate mass/damping/stiffness of Eq. (28) cannot be used to represent the impeller impedances for stability analysis, in cases where the calculated impedance curves have a highly non-quadratic shape. Likewise, this suggests that the accuracy of synchronous imbalance response predictions will be enhanced by utilizing the calculated impedances at PFR=1 instead of using stiffness, damping and mass representations obtained from curve fitting the calculated impedances with quadratic curve fits at each speed.

4.4 Rotordynamic Models and Predicted Response

In order to perform the synchronous unbalance response analysis, the radial and tangential impedances are calculated at multiple spin speeds and the resultant synchronous (PFR=1) impedances vs. spin speeds are plotted in Fig. 24. The two curves shown in Fig. 24 correspond to the following 2 approaches:

a) Quadratic Approximation: The stiffness/damping/mass coefficients are determined at each rotor speed using the least square, quadratic curve-fit of the impedance curves of Fig. 23. The impeller's synchronous impedances (PFR=1) for the unbalance response prediction are then determined from the computed rotordynamic coefficients.

b) Full Impedance: Impedances are selected from the actual curves of Fig. 23 at PFR=1. To utilize the impeller forces for the calculation of the synchronous unbalance frequency response, Eq. (28) is modified as follows:

$$-\begin{Bmatrix} F_x \\ F_y \end{Bmatrix} = \begin{bmatrix} M & m \\ -m & M \end{bmatrix} + \begin{bmatrix} C & c \\ -c & C \end{bmatrix} + \begin{bmatrix} K + K'(\Omega) & k + k'(\Omega) \\ -\left(k + k'(\Omega)\right) & K + K'(\Omega) \end{bmatrix} \quad \textbf{(48)}$$

where K' and k' are included to account for the differences between the actual impedances and the approximated impedances (obtained from the least square quadratic curve fit). This model was used by Williams et al. [20] to predict the unbalance frequency response for a Jeffcott rotor model.

The magnitude of the radial impedance in Fig. 24(a) is quite large compared with

the tangential impedance in Fig. 24(b), at the same spin speed. As the spin speed increases, the absolute values of the radial and tangential impedances increase and the values converge to zero when the spin speed approaches zero. The FE model's synchronous unbalance response vs. spin speed is calculated using the impedances and is shown in Fig. 25. The quadratic approximation impedance approach shows slightly smaller amplitudes than the results of the full impedance approach. The difference results from the deviation between the original impedances and the approximated impedances at PFR=1 in Fig. 24.

The increased amplitude is indicative of reduced damping. Thus the FE model's stability is expected to be less when using the quadratic curve fit than when using the impedances directly from the PFR =1 prediction from the impeller flow CFD model.

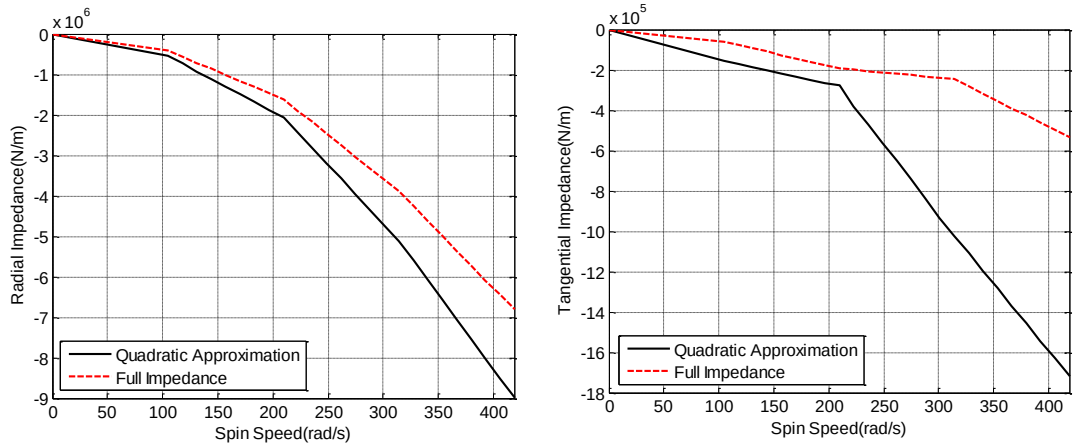

(a) (b)

Fig. 24 Impedances for PFR=1 at multiple spin speeds: (a) radial impedance (b) tangential impedance

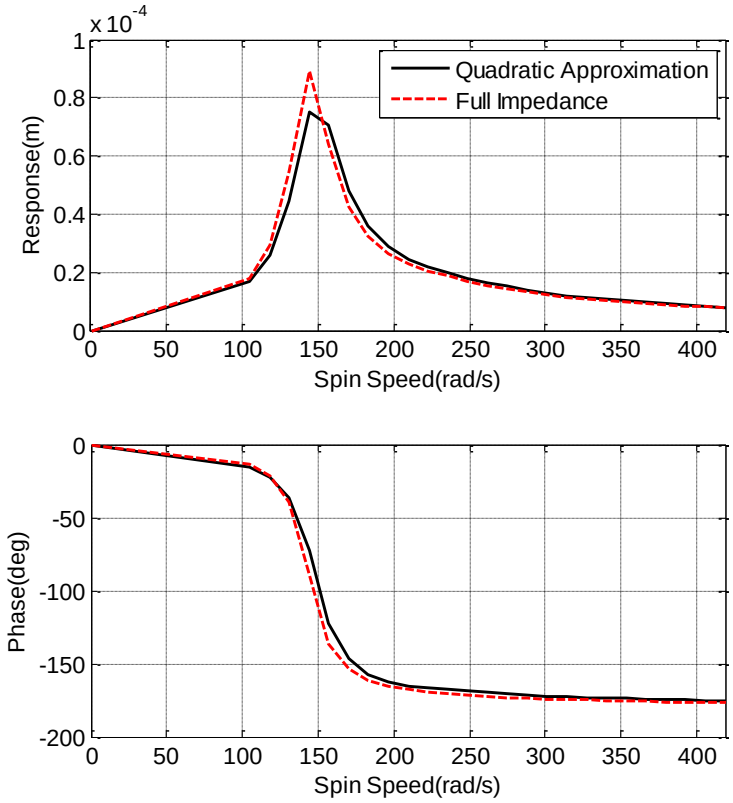

Fig. 25 Synchronous unbalance response vs. spin speed

5. STABILITY ANALYSIS ON JEFFCOTT ROTOR MODEL

Rotordynamic stability of the shaft/bearing/seal/impeller system is typically evaluated by using rotordynamic coefficients calculated from the least squares, quadratic curve fit of the measured or calculated impeller impedances. However, when the bump and dip exists in the computed impedance curves as described in Fig. 12 and Fig. 13, the impedances may not be well represented by the quadratic force model of Eq.(31), in which case the system stability prediction may be unreliable.

In the present study, a curve-fit algorithm is considered to represent the unconventional (bump and dip) impedances of the impeller and include them in the system stability simulation.

5.1 System Stability Prediction with Impeller Impedances for a Jeffcott Rotor Model

For sake of illustration consider the simplified Jeffcott model of a rotating shaft/disc assembly as shown in Fig. 8. This model is often used for explaining some general features of rotating machinery vibration. In the rotor model, fluid induced forces, F_x and F_y, are acting on the disc which represents the wear-ring seal impeller.

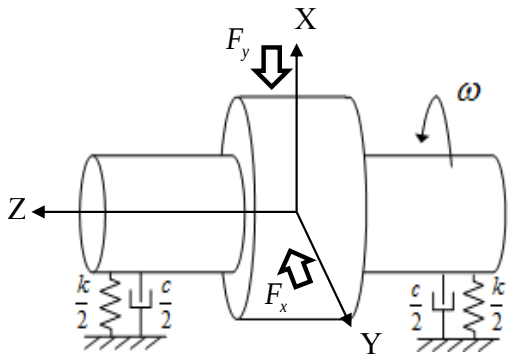

Fig. 26 Simple Jeffcott rotor model including impeller impedances

The governing equations for the Jeffcott rotor model with the impeller forces are expressed by

$$\begin{aligned} m_d \ddot{x} + c_b \dot{x} + k_b x &= F_{u_x} + F_x \\ m_d \ddot{y} + c_b \dot{y} + k_b y &= F_{u_y} + F_y \end{aligned} \tag{49}$$

where c_b and k_b indicate bearing damping and stiffness coefficients, and F_{u_x} and F_{u_y} are unbalance forces in the model. The bearing support stiffness in the model is assumed to be considerably softer than the shaft bending stiffness. The bearing damping ratio ζ is defined as $\zeta = \dfrac{c}{2\, m\, \omega_n}$. As previously mentioned, the impeller forces of Eq. (49) can be modeled by Eq. (28) if the radial and tangential impedance curves have the form of a parabola. The existence of the bump and dip in the impedance curves as shown in Fig. 12 and Fig. 13, may disallow use of Eq. (1) for modelling the fluid induced forces of the impeller. In order to express the forces properly, a new approach is proposed below.

If the fluid induced forces in the x and y direction are assumed to be modeled by *n*th order differential equations, the forces can be described as

$$
\begin{aligned}
-\begin{Bmatrix} F_x \\ F_y \end{Bmatrix} &= \begin{bmatrix} a_0 & b_0 \\ -b_0 & a_0 \end{bmatrix}\begin{Bmatrix} x \\ y \end{Bmatrix} + \begin{bmatrix} a_1 & b_1 \\ -b_1 & a_1 \end{bmatrix}\begin{Bmatrix} \dot{x} \\ \dot{y} \end{Bmatrix} + \begin{bmatrix} a_2 & b_2 \\ -b_2 & a_2 \end{bmatrix}\begin{Bmatrix} \ddot{x} \\ \ddot{y} \end{Bmatrix} + \\
&\begin{bmatrix} a_3 & b_3 \\ -b_3 & a_3 \end{bmatrix}\begin{Bmatrix} \dddot{x} \\ \dddot{y} \end{Bmatrix} + \begin{bmatrix} a_4 & b_4 \\ -b_4 & a_4 \end{bmatrix}\begin{Bmatrix} x^{(4)} \\ y^{(4)} \end{Bmatrix} + \cdots + \begin{bmatrix} a_n & b_n \\ -b_n & a_n \end{bmatrix}\begin{Bmatrix} x^{(n)} \\ y^{(n)} \end{Bmatrix} \\
&= \sum_{i=0}^{n} \begin{bmatrix} a_i & b_i \\ -b_i & a_i \end{bmatrix}\begin{Bmatrix} x^{(\mathrm{i})} \\ y^{(\mathrm{i})} \end{Bmatrix}
\end{aligned}
\tag{50}
$$

For harmonic, steady state vibration of frequency Ω, the fluid forces and the resultant responses are defined as

$$
x = \mathrm{Re}(\bar{x}e^{j\Omega t}),\ y = \mathrm{Re}(\bar{y}e^{j\Omega t}),\ F_x = \mathrm{Re}(\bar{F}_x z^{j\Omega t}),\ F_y = \mathrm{Re}(\bar{F}_y y^{j\Omega t}) \tag{51}
$$

Substitute Eq. (51) into Eq. (50). Then, the forces in x and y direction become

$$
\begin{aligned}
-\begin{Bmatrix} \bar{F}_x \\ \bar{F}_y \end{Bmatrix} e^{j\Omega t} &= \begin{bmatrix} a_0 & b_0 \\ -b_0 & a_0 \end{bmatrix}\begin{Bmatrix} \bar{x} \\ \bar{y} \end{Bmatrix} e^{j\Omega t} + \begin{bmatrix} a_1 & b_1 \\ -b_1 & a_1 \end{bmatrix}\begin{Bmatrix} \bar{x} \\ \bar{y} \end{Bmatrix}\left(j\Omega e^{j\Omega t} \right) \\
&+ \begin{bmatrix} a_2 & b_2 \\ -b_2 & a_2 \end{bmatrix}\begin{Bmatrix} \bar{x} \\ \bar{y} \end{Bmatrix}\left(-\Omega^2 e^{j\Omega t} \right) + \begin{bmatrix} a_3 & b_3 \\ -b_3 & a_3 \end{bmatrix}\begin{Bmatrix} \bar{x} \\ \bar{y} \end{Bmatrix}\left(-j\Omega^3 e^{j\Omega t} \right) \\
&+ \begin{bmatrix} a_4 & b_4 \\ -b_4 & a_4 \end{bmatrix}\begin{Bmatrix} \bar{x} \\ \bar{y} \end{Bmatrix}\left(\Omega^4 e^{j\Omega t} \right) + \cdots + \begin{bmatrix} a_n & b_n \\ -b_n & a_n \end{bmatrix}\begin{Bmatrix} \bar{x} \\ \bar{y} \end{Bmatrix}\left((j\Omega)^n e^{j\Omega t} \right) \\
&= \sum_{i=0}^{n} \begin{bmatrix} a_i & b_i \\ -b_i & a_i \end{bmatrix}\begin{Bmatrix} \bar{x} \\ \bar{y} \end{Bmatrix}\left((j\Omega)^i e^{j\Omega t} \right)
\end{aligned}
\tag{52}
$$

The impeller fluid forces can be expressed as complex forms of functions, $D(j\Omega)$, and $E(j\Omega)$ in the frequency domain as shown below:

$$
-\begin{bmatrix} F_x \\ F_y \end{bmatrix} = \begin{bmatrix} D(j\Omega) & E(j\Omega) \\ -E(j\Omega) & D(j\Omega) \end{bmatrix}\begin{bmatrix} x \\ y \end{bmatrix} \tag{53}
$$

where

$$D(j\Omega) = \left(a_0 - a_2\Omega^2 + a_4\Omega^4 - \cdots\right) + j\left(a_1\Omega - a_3\Omega^3 + a_5\Omega^5 - \cdots\right)$$
$$E(j\Omega) = \left(b_0 - b_2\Omega^2 + b_4\Omega^4 - \cdots\right) + j\left(b_1\Omega - b_3\Omega^3 + b_5\Omega^5 - \cdots\right) \quad \textbf{(54)}$$

Bolleter et al. [2] introduced the force model of Eq. (53) which can be expressed with the complex functions, $D(j\Omega)$ and $E(j\Omega)$ for circular orbit motion, i.e. the shaft center motions become

$$\begin{aligned} x(t) &= r\cos(\Omega t) & , \quad y(t) &= r\sin(\Omega t) \\ \dot{x}(t) &= -r\Omega\sin(\Omega t) & , \quad \dot{y}(t) &= r\Omega\cos(\Omega t) \\ \ddot{x}(t) &= -r\Omega^2\cos(\Omega t) & , \quad \ddot{y}(t) &= -r\Omega^2\sin(\Omega t) \\ \dddot{x}(t) &= r\Omega^3\sin(\Omega t) & , \quad \dddot{y}(t) &= -r\Omega^3\cos(\Omega t) \\ &\vdots & &\vdots \end{aligned} \quad \textbf{(55)}$$

In order to obtain the radial and tangential impedances, substitute Eq. (55) into Eq.(50) and evaluate the resulting equation at $\Omega t = 0$:

$$-\begin{Bmatrix} F_r \\ F_t \end{Bmatrix} = -\begin{Bmatrix} F_x(0) \\ F_y(0) \end{Bmatrix} = \begin{bmatrix} a_0 & b_0 \\ -b_0 & a_0 \end{bmatrix}\begin{Bmatrix} r \\ 0 \end{Bmatrix} + \begin{bmatrix} a_1 & b_1 \\ -b_1 & a_1 \end{bmatrix}\begin{Bmatrix} 0 \\ r\Omega \end{Bmatrix} + \begin{bmatrix} a_2 & b_2 \\ -b_2 & a_2 \end{bmatrix}\begin{Bmatrix} -r\Omega^2 \\ 0 \end{Bmatrix} + \begin{bmatrix} a_3 & b_3 \\ -b_3 & a_3 \end{bmatrix}\begin{Bmatrix} 0 \\ -r\Omega^3 \end{Bmatrix} + \begin{bmatrix} a_4 & b_4 \\ -b_4 & a_4 \end{bmatrix}\begin{Bmatrix} r\Omega^4 \\ 0 \end{Bmatrix} + \cdots \quad \textbf{(56)}$$

or;

$$-\begin{Bmatrix} I_r \\ I_t \end{Bmatrix} = -\begin{Bmatrix} F_r / r \\ F_t / r \end{Bmatrix} = \begin{bmatrix} a_0 + b_1\Omega - a_2\Omega^2 - b_3\Omega^3 + a_4\Omega^4 + \cdots \\ -b_0 - a_1\Omega + b_2\Omega^2 + a_3\Omega^3 - b_4\Omega^4 + \cdots \end{bmatrix} \quad \textbf{(57)}$$

From Eq. (53), (54), and (57), the radial and tangential impedances for the forward and backward whirl can be determined using

$$
\begin{aligned}
I_r^{+}(\Omega) &= -\mathrm{Re}\left[D(j\Omega)\right] - \mathrm{Im}\left[E(j\Omega)\right] \\
I_r^{-}(\Omega) &= -\mathrm{Re}\left[D(j\Omega)\right] + \mathrm{Im}\left[E(j\Omega)\right] \\
I_\theta^{+}(\Omega) &= +\mathrm{Re}[E(j\Omega)] - \mathrm{Im}\left[D(j\Omega)\right] \\
I_\theta^{-}(\Omega) &= +\mathrm{Re}\left[E(j\Omega)\right] + \mathrm{Im}[D(j\Omega)]
\end{aligned}
\qquad \textbf{(58)}
$$

In the above equations, I_r and I_t represent the radial and tangential impedances and the superscripts of the impedance functions, '+' and '-', indicate the forward and backward whirl cases, respectively. $D(j\Omega)$ and $E(j\Omega)$ can be calculated using Eq. (58) with the meadured or calculated impedances. After calculating $D(j\Omega)$ and $E(j\Omega)$, each function can be identified in the form of the transfer functions, $D(s)$ and $E(s)$, by utilizing the system identification toolkit in Matlab. The detailed procedure for deriving the transfer functions will be delivered in the next chapter. Once the transfer functions are computed, Eq. (49) can be rewritten in the Laplace domain by considering the relation of Eq. (53) as follows:

$$
\begin{aligned}
\left(m_d s^2 + c_b s + k_b\right) x(s) &= T_{xx}(s) + T_{xy}(s) + F_{u_x}(s) \\
\left(m_d s^2 + c_b s + k_b\right) y(x) &= T_{yx}(s) + T_{yy}(s) + F_{u_y}(s)
\end{aligned}
\qquad \textbf{(59)}
$$

where

$$
T_{xx}(s) = D(s)x(s),\ T_{xy}(s) = E(s)y(s),\ T_{yx}(s) = -E(s)x(s),\ T_{yy}(s) = D(s)y(s) \qquad \textbf{(60)}
$$

Eqs. (59) are transformed into a set of 1st order differential equations in order to solve for system stability. Let

$$
\begin{aligned}
v_x &= \dot{x} \\
v_y &= \dot{y}
\end{aligned}
\qquad \textbf{(61)}
$$

The state space counterparts of the transfer functions, $D(s)$ and $E(s)$, are defined by:

$$
\begin{aligned}
\dot{Z}_{xx} &= A_{xx} Z_{xx} + B_{xx} x, \quad T_{xx} = C_{xx} Z_{xx} \\
\dot{Z}_{xy} &= A_{xy} Z_{xy} + B_{xy} y, \quad T_{xy} = C_{xy} Z_{xy} \\
\dot{Z}_{yx} &= A_{yx} Z_{yx} + B_{yx} x, \quad T_{yx} = C_{yx} Z_{yx} \\
\dot{Z}_{yy} &= A_{yy} Z_{yy} + B_{yy} y, \quad T_{yy} = C_{yy} Z_{yy}
\end{aligned}
\tag{62}
$$

Substituting the velocity vectors of Eq. (61) and the state equations of Eq. (62) into Eq. (49), provides the state variable form

$$
\begin{aligned}
\dot{x} &= v_x \\
\dot{y} &= v_y \\
\dot{v}_x &= \frac{1}{m_d}\left(-c_b v_x - k_b x + C_{xx} Z_{xx} + C_{xy} Z_{xy} + F_{u_x}\right) \\
\dot{v}_y &= \frac{1}{m_d}\left(-c_b v_y - k_b y + C_{yx} Z_{yx} + C_{yy} Z_{yy} + F_{u_y}\right) \\
\dot{Z}_{xx} &= A_{xx} Z_{xx} + B_{xx} x \\
\dot{Z}_{xy} &= A_{xy} Z_{xy} + B_{xy} y \\
\dot{Z}_{yx} &= A_{yx} Z_{yx} + B_{yx} x \\
Z_{yy} &= A_{yy} Z_{yy} + B_{yy} y
\end{aligned}
\tag{63}
$$

The corresponding matrix form is

$$
\dot{Z} = AZ + BF \tag{64}
$$

where

$$
A = \begin{bmatrix}
0 & 0 & 1 & 0 & 0 & 0 & 0 & 0 \\
0 & 0 & 0 & 1 & 0 & 0 & 0 & 0 \\
-k_b/m_d & 0 & -c_b/m_d & 0 & C_{xx}/m_d & C_{xy}/m_d & 0 & 0 \\
0 & -k_b/m_d & 0 & -c_b/m_d & 0 & 0 & C_{yx}/m_d & C_{yy}/m_d \\
B_{xx} & 0 & 0 & 0 & A_{xx} & 0 & 0 & 0 \\
0 & B_{xy} & 0 & 0 & 0 & A_{xy} & 0 & 0 \\
B_{yx} & 0 & 0 & 0 & 0 & 0 & A_{yx} & 0 \\
0 & B_{yy} & 0 & 0 & 0 & 0 & 0 & A_{yy}
\end{bmatrix},
\tag{65}
$$

$$
B = \begin{bmatrix}
0 & 0 & 1 & 0 & 0 & 0 & 0 & 0 \\
0 & 0 & 0 & 1 & 0 & 0 & 0 & 0
\end{bmatrix}^T
$$

and

$$Z = \begin{Bmatrix} x & y & v_x & v_y & Z_{xx} & Z_{xy} & Z_{yx} & Z_{yy} \end{Bmatrix}^T,\ F = \begin{Bmatrix} F_{u_x} \\ F_{u_y} \end{Bmatrix} \tag{66}$$

Note that the above are partitioned matrices since $A_{xx}, A_{xy}, A_{yx}, A_{yy}$, $B_{xx}, B_{xy}, B_{yx}, B_{yy}$ $C_{xx}, C_{xy}, C_{yx}, C_{yy}$ are matrix – vector quantities. In the above equation, A represents the system matrix for the Jeffcott rotor model with impeller forces, and B is the matrix that weights the given inputs. The solutions to Eq. (66) are obtained by assuming a solution that has the form of $Z = \tilde{Z}e^{\lambda t}$, which yields

$$(\lambda I - A)\tilde{Z} = 0 \tag{67}$$

where I denotes the identity matrix.

The eigenvalues and eigenvectors of the Jeffcott rotor system can be determined by using the MATLAB ‘eig’ command or any other eigenvalue solver.

5.2 Identifying Approximated Impedances for Verification

Eq. (49) for the Jeffcott rotor of Fig. 26 can be rewritten as follows assuming that the fluid induced forces satisfy the quadratic curve model and can be accurately described within the framework of Eq. (28),

$$\begin{bmatrix} m_d + M & m \\ -m & m_d + M \end{bmatrix} \begin{Bmatrix} \ddot{x} \\ \ddot{y} \end{Bmatrix} + \begin{bmatrix} c_b + C & c \\ -c & c_b + C \end{bmatrix} \begin{Bmatrix} \dot{x} \\ \dot{y} \end{Bmatrix} + \begin{bmatrix} k_b + K & k \\ -k & k_b + K \end{bmatrix} \begin{Bmatrix} x \\ y \end{Bmatrix} = \begin{Bmatrix} F_{u_x} \\ F_{u_y} \end{Bmatrix} \tag{68}$$

In this section, the conventional stability analysis using the relation of Eq. (68), i.e. the ‘MCK Model’ is considered in order to compare results with the more exact

transfer function model. The transfer function model more accurately captures the bump and dip shape of the predicted impedance curves.

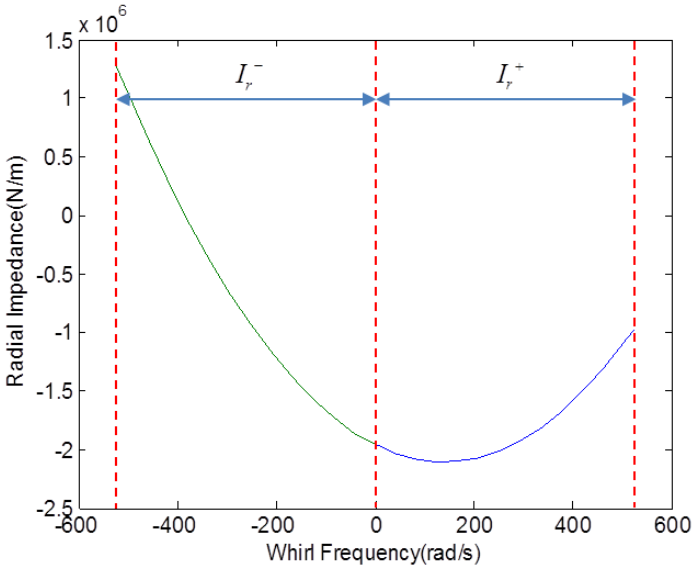

(a)

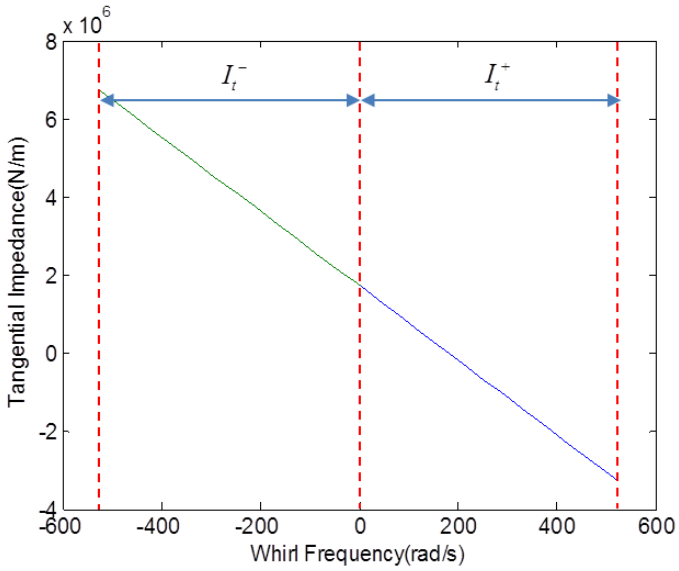

(b)

Fig. 27 Least square curve-fit impedances of 2,000 rpm case (a) tangential impedance (b) radial impedance

For verification purposes the general transfer function model is applied to a purely quadratic impedance curve (Fig. 9) to determine if the results agree with the MCK model. The negative frequencies in this figure correspond to the imposed backward, circular orbits of the impeller in the CFD model. The dynamic coefficient values utilized to generate the impedance curves in Fig. 27 are shown in Table 12. The impedances I_r^+, I_r^-, I_t^+, and, I_t^- of Fig. 27 are utilized to calculate $D(j\Omega)$ and $E(j\Omega)$ functions of Eq. (58). Fig. 28 indicates the computed magnitude and phase of the functions.

Table 12 Approximated rotordynamic coefficients of the conventional wear-ring seal impeller using least square curve-fit

Rotordynamic Coefficients	Values
$K\,(MN/m)$	1.96
$k\,(MN/m)$	1.72
$C\,(KN\cdot s/m)$	9.55
$c\,(KN\cdot s/m)$	2.14
$M\,(kg)$	7.7
$m\,(kg)$	0.009
$\frac{k}{C\omega}$	0.86

Once $D(j\Omega)$ and $E(j\Omega)$ functions are obtained, the corresponding transfer functions $D(\mathrm{s})$ and $E(\mathrm{s})$ are determined to utilize them in the stability analysis Eq. (67). Kleynhans et al. [21] introduced general transfer function models for the eigenvalue analysis, following the model of Bolleter et al. [2]. Thorat et al. [22]

expanded the model by using a curve-fit approach to obtain the D and E functions. However, the approximated transfer functions of Kleynhans [21] had low quality curve-fit results and the ranges were limited, and the transfer function calculated by Thorat [22] had unstable poles (open loop unstable). In the present study, an open-loop stable transfer function for the full range of the original curves is obtained by including artificial, fast (large, negative pure real) poles in the curve fit. Identification of the transfer functions utilizes the Matlab system identification command 'invfreqs'. The command employs an iterative algorithm developed by Levi [43], which is based on the damped Gauss-Newton method. The detailed procedure to derive the transfer functions with stable poles is described as follows:

(1) Obtain $D(j\Omega)$ and $E(j\Omega)$ functions from the forward and backward whirl, measured or predicted impedances at specified whirl frequencies.

(2) Curve-fit the $D(j\Omega)$ and $E(j\Omega)$ amplitude and phase angle vs. Ω with nth or der numerators and zeroth order denominators in the form

$$\frac{b_1 s^n + b_2 s^{n-1} + \cdots + b_{n+1}}{1} \tag{69}$$

(3) Include (n+1) artificial fast real poles. These poles are sufficiently displaced i n the left hand plane to have no influence on the curve fit transfer functions in the range of interest. Include a series product of the added fast poles in a man ner that insures an invariant zero frequency.

$$\frac{p_1 p_2 \cdots p_{n+1}(b_1 s^n + b_2 s^{n-1} + \cdots + b_{n+1})}{(s+p_1)(s+p_2)\cdots(s+p_{n+1})} \tag{70}$$

Curve fits of the $D(j\Omega)$ and $E(j\Omega)$ functions are obtained with the above procedure applied to the results in Fig. 28, and the curve fits are overlaid with the data from Fig. 28, in Fig. 29. Goodness-of-fit for each result is excellent as expressed by R^2 values indicated in the plots. The corresponding curve fit transfer functions are

$$D(s) = \frac{1.616\times10^{18}s^2 + 2.005\times10^{21}s + 4.116\times10^{23}}{s^3 + 1.8\times10^{6}s^2 + 1.07\times10^{12}s + 2.1\times10^{17}}$$

$$E(s) = \frac{1.968\times10^{15}s^2 + 4.487\times10^{20}s + 3.613\times10^{23}}{s^3 + 1.8\times10^{6}s^2 + 1.07\times10^{12}s + 2.1\times10^{17}} \quad \textbf{(71)}$$

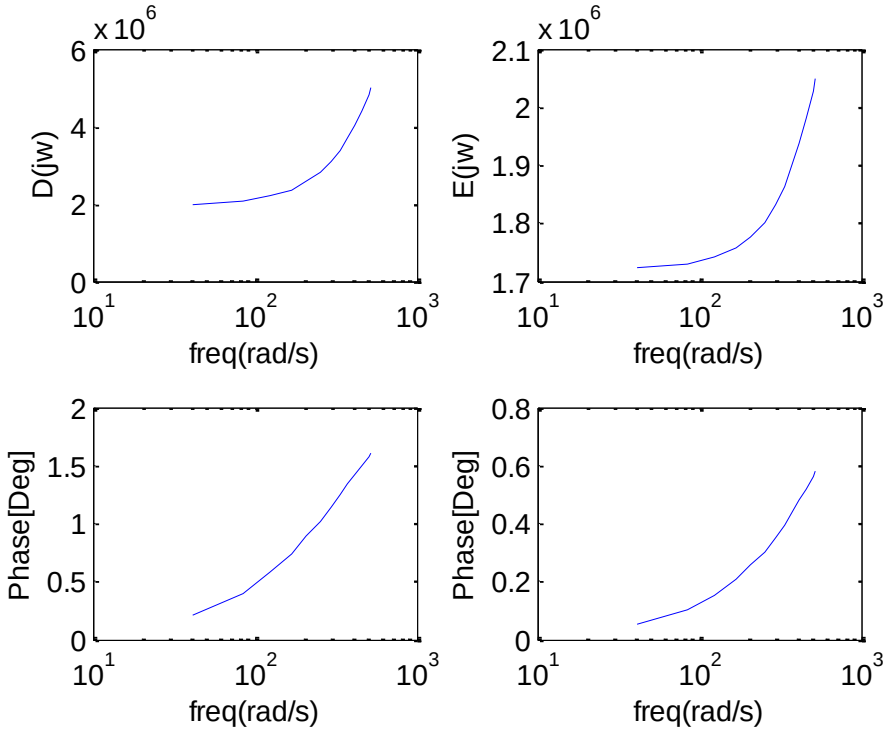

Fig. 28 Magnitude and phase of $D(j\Omega)$ and $E(j\Omega)$ for the approximated quadratic impedances of 2,000 rpm case

The values of the added fast poles for this example are :

$$p_1 = -500000,\ \ p_2 = -600000,\ \ p_3 = -700000 \tag{72}$$

The derived transfer functions of Eq. (71) are open-loop stable and the curve-fit results of Fig. 29 show good quality to represent the complex functions with the 2nd order numerators and the 3rd order denominators.

Experience indicates that low order fits are required to obtain reliable system eigenvalue results. This results because the magnitudes of the coefficients in the transfer functions significantly increase for higher order transfer functions. In case of the approximated impedance case of Fig. 28, smooth curves of $D(j\Omega)$ and $E(j\Omega)$ facilitate to obtain good quality curve-fits with relatively lower order transfer functions. However, when considering the complex curves of Fig. 12 and Fig. 13, the order of the transfer functions must be increased to enhance the curve-fit qualities.

A novel approach is utilized in order to obtain high quality curve-fit with lower order transfer functions for arbitrary shapes of the complex impedance curves. This approach divides the frequency range into segments and then employs independent curve fits of $D(j\Omega)$ and $E(j\Omega)$ over each frequency segment. For the segmentation approach, the curves of Fig. 28 should be divided in the frequency domain and the transfer functions should be calculated for each segment, respectively.

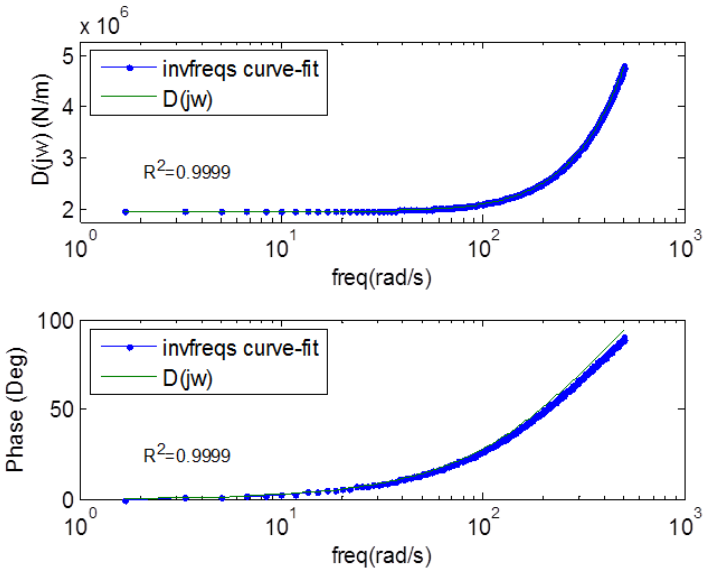

(a)

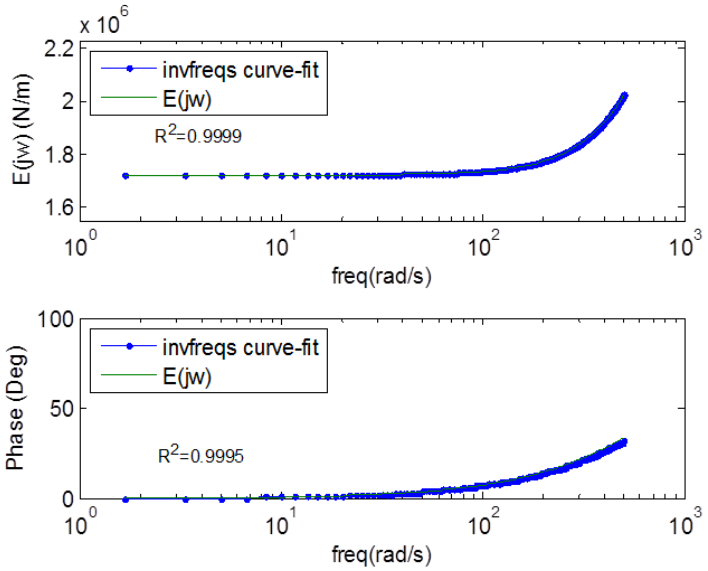

(b)

Fig. 29 Curve fit results of $D(j\Omega)$ and $E(j\Omega)$ for the approximated impedances of 2,000 rpm case

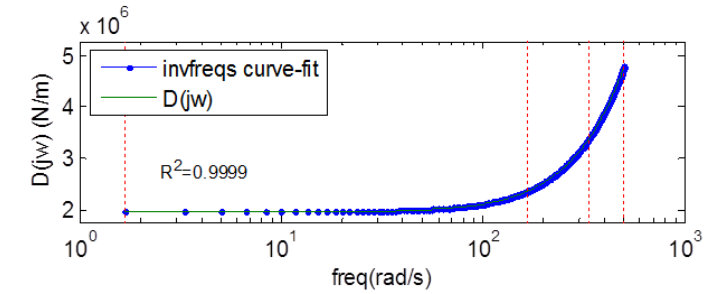

(a)

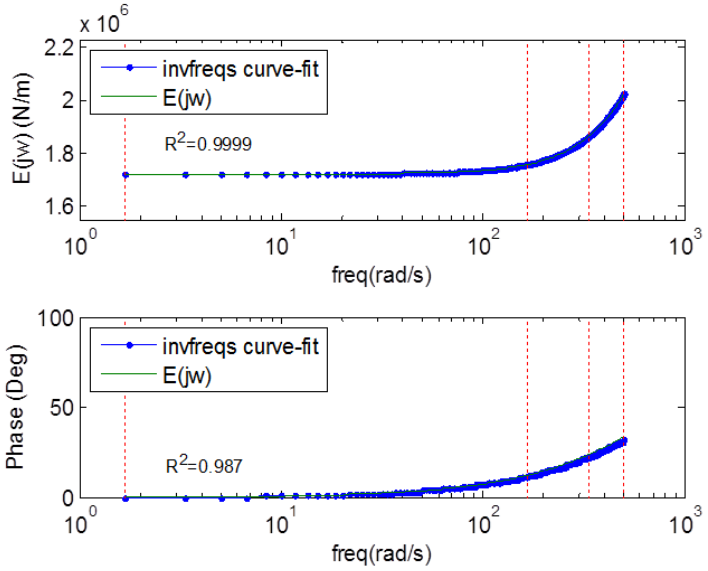

(b)

Fig. 30 Curve fit results utilizing frequency range segmentation of $D(j\Omega)$ and $E(j\Omega)$ for the approximated impedances of 2,000 rpm

Fig. 30 show curve-fit results with the multiple segments (red dashed lines) transfer function. The curve-fits are sufficient to represent the function of $D(j\Omega)$ and

$E(j\Omega)$ quite well. These transfer functions are provided in the Appendix A. In the proposed segmented model approach, the width of each segment is determined with the analyst's intuition using the following considerations:

1) The curve-fit quality of each segment should be high enough to predict m ore accurate eigenvalues and eigenvectors for the stability analysis.
2) The order of the determined transfer function should be minimized to red uce mathematical errors and computation time.
3) The number of segments should be minimized to secure computational ef ficiency.

In order to examine the validity of the segmentation, an eigenvalue analysis is provided and comparison of logarithmic decrement (log-dec) for 'MCK model', 'Transfer Function Model', and 'Transfer Function Model with Segmentation' is made for the verification. For the analysis, the mass and the natural frequency of the Jeffcott rotor model (without impeller force) of Fig. 26 are chosen as below:

$$m_d = 120 \text{ Kg}, \ \omega_n = 150 \text{ rad/s} \quad \textbf{(73)}$$

A system matrix, A, in Eq. (33) is evaluated for each frequency range segment established in the transfer function curve fit. The eigenvalues of the i^{th} segment A matrix are evaluated and those with frequencies outside of the i^{th} frequency segment range are discarded. This process is repeated for all frequency segments. Fig. 31 shows the calculated log-dec from the computed eigenvalues. As expected the calculated results for the three approaches are almost identical since the impedance curve was developed

by selecting dynamic coefficients and generation the impedance curves using quadratic frequency representations. This provided confirmation of the segmentation approach for stability analysis, for the no-dip, no-bump, conventional quadratic impedance case. In the next section, the transfer function model with segmentation will be applied for the unconventional impedance cases and the influence of the bumps and dips in the impedance curves on the rotordynamic stability will be examined.

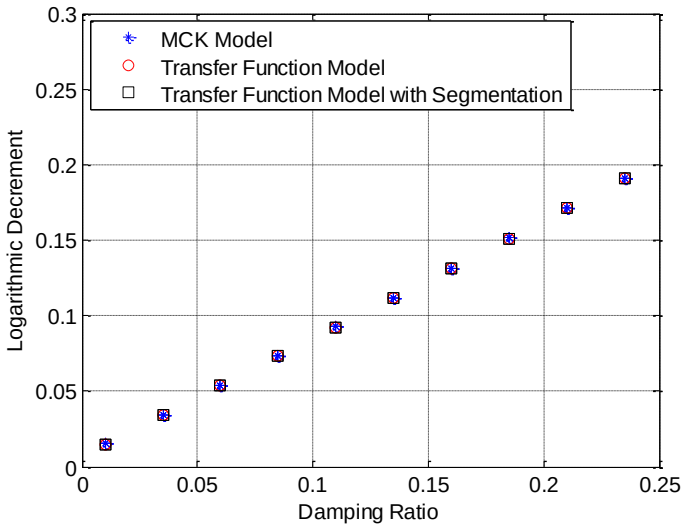

Fig. 31 Comparison of system log-dec for the quadratic impedance case, vs. damping ratio ζ

5.3 Unconventional Impedance and Stability Analysis

The impedances for the 4,000 rpm case in Fig. 23 are chosen to investigate the effect of the magnitude of the bump and dip in the impedance curves. The full frequency range curve fit approach is first utilized to identify the transfer functions of the impedance curves.

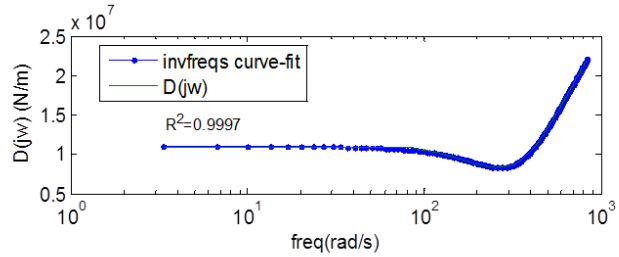

(a)

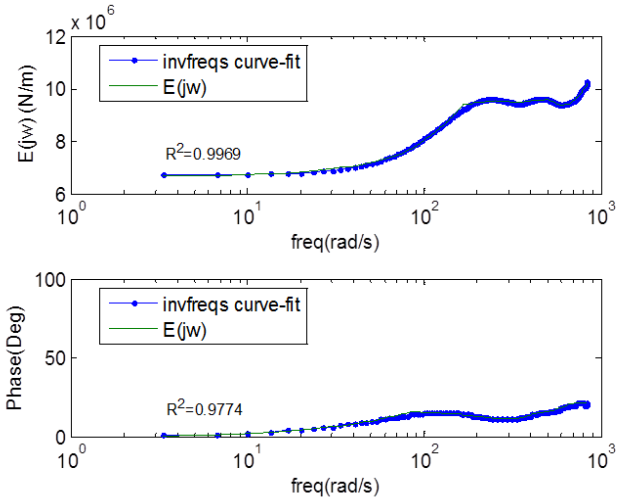

(b)

Fig. 32 Curve fit results of 4,000 rpm case by transfer function model

Fig. 32 illustrates the results of the transfer function model. As mentioned in the previous section, transfer functions should have low order numerators and denominator to ensure numerically stable results. For the selected case, however, the orders of the numerators and denominators are determined to be 18 and 19 after repeating the curve-fit process for several times to obtain high quality curve-fit results. The derived transfer

functions are shown in the Appendix A. The high orders of the numerators and the denominators yield coefficients with magnitudes exceeding 10^{100}. This will result in erroneous eigenvalues and singular matrix calculations in Matlab. Thus, the derived high order transfer functions cannot be applied for stability analysis and the segmentation approach is required to calculate low order transfer functions for the selected case.

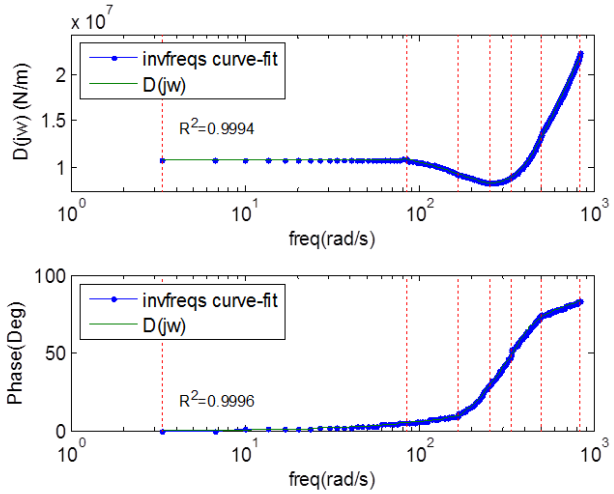

(a)

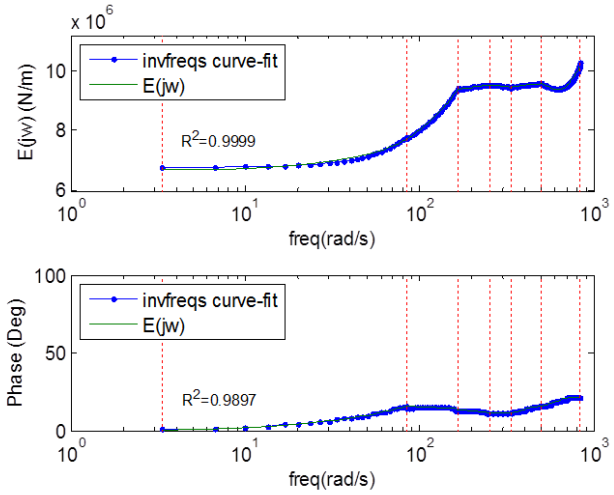

(b)

Fig. 33 Curve fit results of 4,000 rpm case by transfer function model with segmentation

To obtain high quality curve-fit results with lower order transfer functions, the curves are divided into 6 segments and the transfer function for each segment is calculated separately. Fig. 33 provides the results of the transfer function model with segmentation. The obtained transfer functions are also indicated in Appendix A.

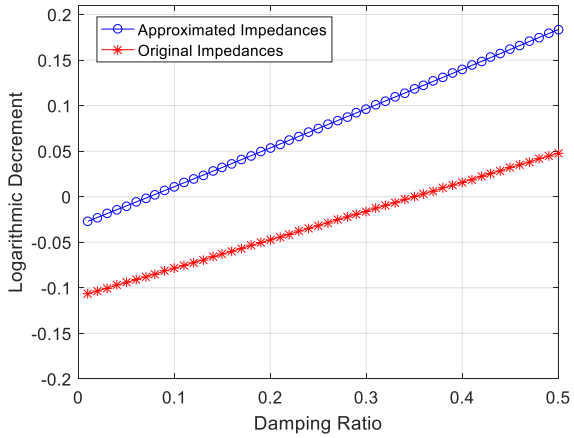

Fig. 34 Comparison of log-dec between the approximate (quadratic) impedances and the original (segmented curve fit) impedances, vs damping ratio ζ for 4,000 rpm case

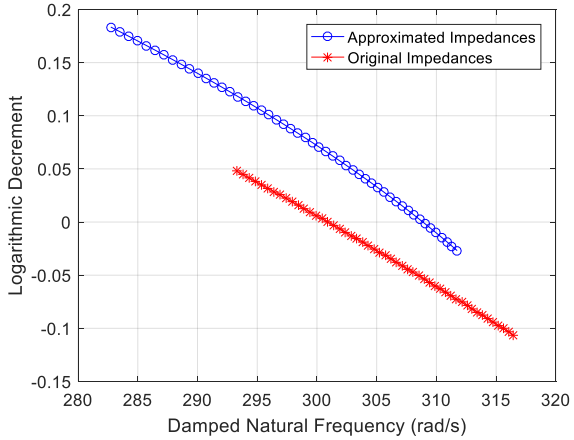

Fig. 35 Log-dec versus damped natural frequency (rad/s) for 4,000 rpm case

Stability analysis of the Jeffcott model is performed utilizing the parameters of Eq. (73). A comparison is made between the approximate (quadratic curve fit) impedances and the original impedances in Fig. 34 by utilizing impedances at 4,000 rpm in Fig. 23. The purpose is to investigate the effect of the impedance curve bump and dip on rotordynamic stability. The results of the approximated (quadratic curve fit) impedance case have relatively larger logarithmic decrement values than the results of the original (segmented curve fit) impedance case and the differences are too large to neglect for accurate stability analysis. Fig. 35 indicates the compared log-dec versus damped natural frequency for 4,000 rpm case. The damped natural frequency is reduced by 3 percent producing smaller values of log-dec when the original impedances are applied in the Jeffcott rotor model. These results suggest a necessity of the segmentation approach for more accurate results when predicted or measured fluid induced forces acting on the rotordynamic systems cannot be properly fit by the conventional quadratic model.

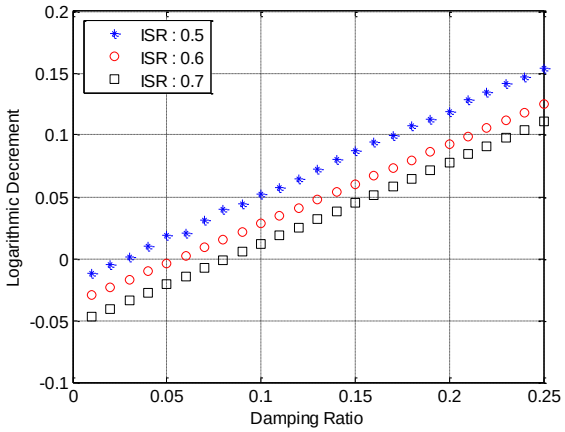

Fig. 36 Log-dec versus damping ratio ζ comparisons for different ISR for 2,000 rpm case using the multi-segment approach

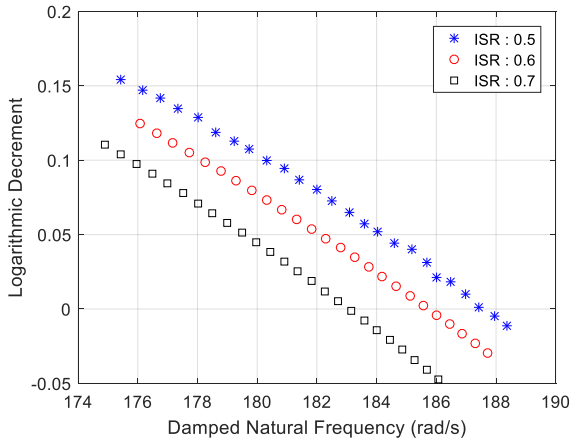

Fig. 37 Log-dec versus damped natural frequency (rad/s) for different ISR for 2,000 rpm case using the multi-segment approach

Fig. 36 indicates the predicted log-dec for 3 inlet swirl ratios ISR of the Jeffcott rotor model. Impedances of Fig. 12 and Fig. 13 are utilized to evaluate the effect of ISR on the rotordynamic stability. Fig. 37 shows log-dec versus damped natural frequency according to the applied ISR. With larger ISR, speed for the unstable motion is decreasing.

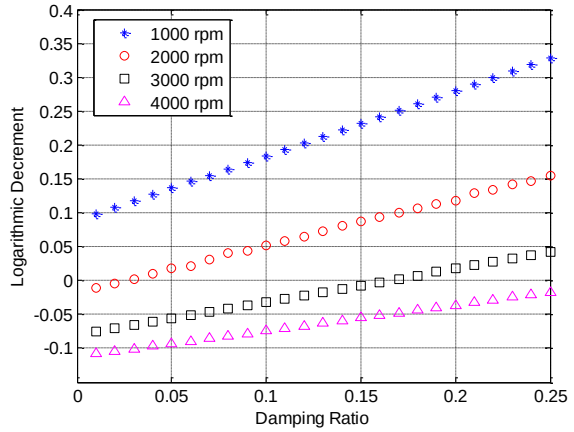

Fig. 38 Log-dec versus damping ratio ζ comparisons for different spin speeds using the multi-segment approach

In Fig. 38, the dependence on impeller spin speed is investigated using the impedances in Fig. 23. The rotor bearing system stability is seen to be significantly diminished and lost as spin speed increases. The effect of the spin speed on the rotordynamic stability is clearly larger than the effect of the ISR.

Fig. 34 clearly indicates that the peaks in the impedances curves have a negative influence on the rotordynamic stability of the Jeffcott rotor model. From the results, it can be concluded that stability predictions may have significant errors when the radial and tangential impedances curves do not follow the forms of a parabola, using the conventional form of Eq.(31).

6. ROTORDYNAMIC ANALYSIS OF CENTRIFUGAL COMPRESSOR IMPELLER WITH PRECESSING MOTION[5]

6.1 Overview of Precessing Motion

In rotating machinery, a vibrating rotor can be described by whirling and precessing motions that can cause rotordynamic instability problems. In the present study, the analyses shown so far are about the fluid induced forces caused by the whirling motion of the frond shroud leakage path. Unlike the whirling motion, the studies on the precessing motion mostly have been performed for the backshroud region. Tsujimoto et al. [6] and Yoshida et al. [7] measured and predicted the reaction moments induced by the precessing motion on the backshroud/casing and explained the destabilizing mechanism at small precessing velocity ratio for the positive radial fluid moment. Flow mechanism was discussed using bulk flow analysis by Tsujimoto et al. [6]. With the reduced clearance at the entrance ('Gap-A') of the backshroud, the absolute value of fluid moments is increasing and the range of the destabilizing frequency is increasing with the increased leakage flow rate in their research.

[5] Reprinted in Part with permission from "Fluid Force Moment on a Centrifugal Impeller Shroud in Precessing Motion," by Yoshinobu Tsujimoto, Yoshiki Yoshida, Hideo Ohashi, orihiro Teramoto, and Shin Ishizaki, J. Fluids Eng., 1997, 119(2), pp. 366-371. © 1997 ASME.

6.2 Moment Coefficients for Precessing Impeller

In turbomachinery, precessing motion occurs by the angular motion of the tilted rotating shaft. Fig. 39 describes a precessing motion of an impeller studied by Tsujimoto et al. [6]. In the precessing motion of the centrifugal impeller, the rotor is precessing at the speed Ω while its surface spins on center of rotor at the speed ω. The r-axis is on the impeller and located at the maximum backshroud/casing clearance and the t-axis is also on the impeller and placed perpendicular to the r-axis. The fluid moment indicated in the coordinate system can be calculated as follows:

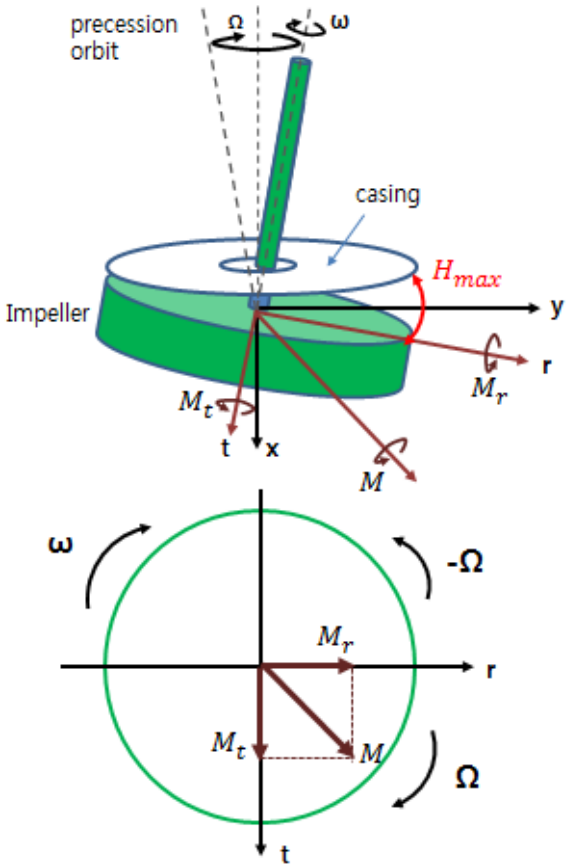

Fig. 39 Coordinate system and components of moment [6]

$$\begin{aligned}\vec{M} &= \vec{r} \times \vec{F} \\ &= |M_x|\vec{e}_x + |M_y|\vec{e}_y + |M_z|\vec{e}_z \\ &= \sum\left[\left(|y||f_z| - |z||f_y|\right)\vec{e}_x + \left(|z||f_x| - |x||f_z|\right)\vec{e}_y + \left(|x||f_y| - |y||f_x|\vec{e}_z\right)\right]\end{aligned} \quad \textbf{(74)}$$

where, f_x : X direction force at each node

f_y : Y direction force at each node

f_z : Z direction force at each node

x, y, z : Cartesian Coordinates at each node

In Eq.(74), the magnitudes of M_x and M_y are

$$|M_x| = |y||f_z| - |z||f_y| \quad \textbf{(75)}$$

$$|M_y| = |z||f_x| - |x||f_z| \quad \textbf{(76)}$$

The reaction moments are represented as:

$$\begin{bmatrix} M_x \\ M_y \end{bmatrix} = -\begin{bmatrix} M_\alpha & m_\alpha \\ -m_\alpha & M_\alpha \end{bmatrix}\begin{Bmatrix} \ddot{\alpha}_x \\ \ddot{\alpha}_y \end{Bmatrix} - \begin{bmatrix} C_\alpha & c_\alpha \\ -c_\alpha & C_\alpha \end{bmatrix}\begin{Bmatrix} \dot{\alpha}_x \\ \dot{\alpha}_y \end{Bmatrix} - \begin{bmatrix} K_\alpha & k_\alpha \\ -k_\alpha & K_\alpha \end{bmatrix}\begin{Bmatrix} \alpha_x \\ \alpha_y \end{Bmatrix} \quad \textbf{(77)}$$

where, M_α : Direct added inertia, m_α : Cross-coupled inertia

C_α : Direct damping, c_α : Cross-coupled damping

K_α : Direct stiffness, k_α : Cross-coupled stiffness

Eq. (77) is non-dimensionalized by $I\alpha\omega^2$. I is the moment of inertia which is defined as

$$I = \rho \pi R_i^{\,2} b_2 i^2 \tag{78}$$

where, ρ : fluid density

R_i : impeller outer radius

b_2 : impeller outlet height

i : radius of gyration : $i = \sqrt{\frac{R_i^{\,2}}{4} + \frac{b_2^{\,2}}{12}}$

Since the geometrical condition around the impeller is symmetric, M_r and M_t can be defined by the following quadratic equation using nondimensionalized components follows **[7**, 9]:

$$M_r = \frac{M_y}{I\alpha\omega^2} = \frac{m_\alpha}{I}\left(\frac{\Omega}{\omega}\right)^2 + \frac{C_\alpha}{I\omega}\left(\frac{\Omega}{\omega}\right) - \frac{k_\alpha}{I\omega^2} \tag{79}$$

$$M_t = \frac{M_x}{I\alpha\omega^2} = \frac{M_\alpha}{I}\left(\frac{\Omega}{\omega}\right)^2 - \frac{c_\alpha}{I\omega}\left(\frac{\Omega}{\omega}\right) - \frac{K_\alpha}{I\omega^2} \tag{80}$$

6.3 Modeling for Precessing Impeller

The basic geometry of the backshroud is shown in Fig. 40. The center of precessing motion is placed at the impeller center 'O' and the tilt angle of the shaft is set with 0.9°. Tsujimoto et al. **[6**] measured pressure distribution between radii r=47.5 and r=165mm and integrated it to calculate the fluid moment of the backshroud for various leakage flow rate which was controlled by suction blower. And the measured range of precessing frequency ratio ($f = \Omega/\omega$) is from -1.4 to 1.4.

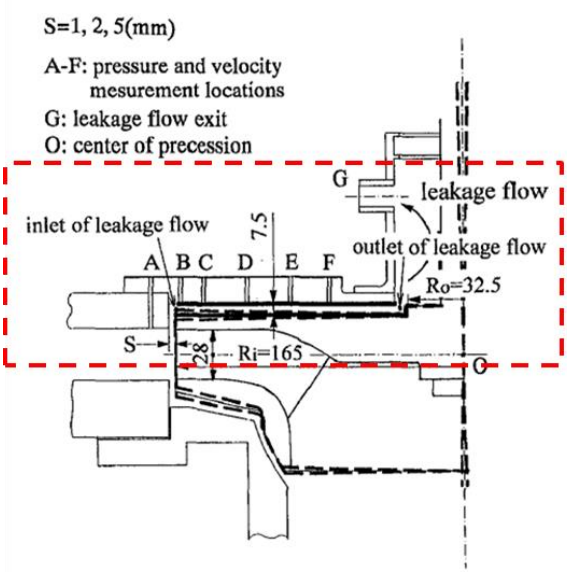

Fig. 40 Basic geometry of Backshroud [6]

Dimensions indicated in Fig. 41 are utilized to construct 3D Backshroud model for CFD analysis. Downstream region of the figure is for the leakage flow and the region including 1mm outlet gap is approximated based on the indicated shape in Fig. 40. The backshroud surface in Fig. 41 is rotated through 0.9° counterclockwise with respect to the origin O to make precessing motion of the backshroud. Based on the dimensions, a 3D model is created using 3D modeler as shown in Fig. 42.

The precessing motion can be solved by defining the tilted fluid region as a rotating frame while the stator wall is defined as a rotating wall in the opposite direction to the rotating frame. The center of the precessing is z-axis and the center of the rotating shroud surface is the inclined axis with 0.9 from the z-axis. For the CFD simulation, the backshroud model of centrifugal impeller is composed of 2 domains, IN and OUT as shown in Fig. 41. IN domain is for imposing the inlet swirl velocity and OUT domain is for generating precessing frequency.

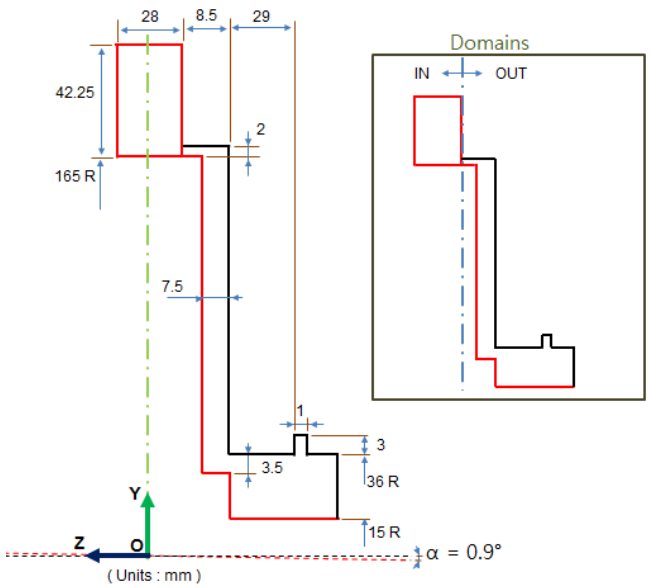

Fig. 41 Dimensions of the backshroud/casing for 3D CFD modeling

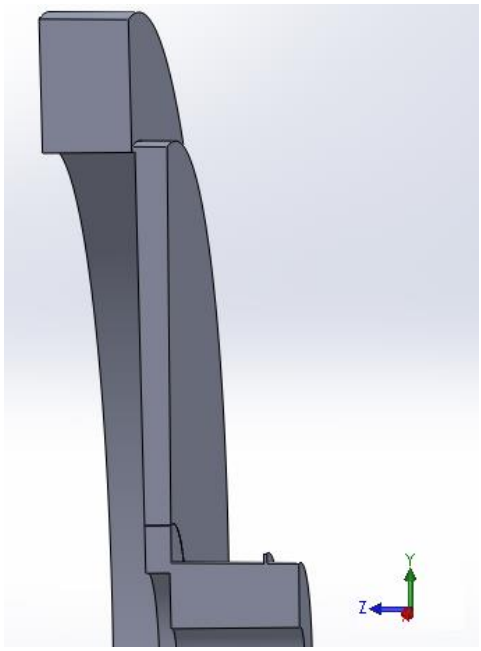

Fig. 42 3D model of the backshroud of centrifugal impeller

6.4 Calculating Rotordynamic Coefficients for Precessing Impeller

In CFD analysis, the considered precessing frequency ratios in the backshroud leakage path for calculating the rotordynamic coefficients are ranging from -1 to 1.5. Shroud surface between r=47.5mm and r=165mm is defined for integrating pressure to calculate the moment coefficients. Based on the test parameters of Ref **[6**, 7], boundary conditions for CFD analysis are determined. Table 13 shows the operating conditions of the centrifugal impeller. Working fluid is air and isothermal condition is assumed in the simulation.

Table 13 Operating conditions of the centrifugal impeller

Supply Pressure	1.1375 bar
Exit Pressure	1.1329 bar
Running Speed	677 rpm
Design flow rate	0.043 kg/s
Inlet Swirl Ratio	0.5
Temperature	305 K
Working Fluid	Air
Leakage Flow Rate	0.00355 kg/s

Vector plot at the backshroud inlet is shown in Fig. 43, showing the presence of recirculation zone. The centrifugal acceleration force causes reverse flow toward the backshroud inlet, while pressure forces drive the flow downward near the stator wall. Fig. 44 shows velocity vector at leakage flow path. Since the space of the leakage path is large when considering the leakage flow rate, the intensity of the recirculation flow near the leakage outlet is relatively week.

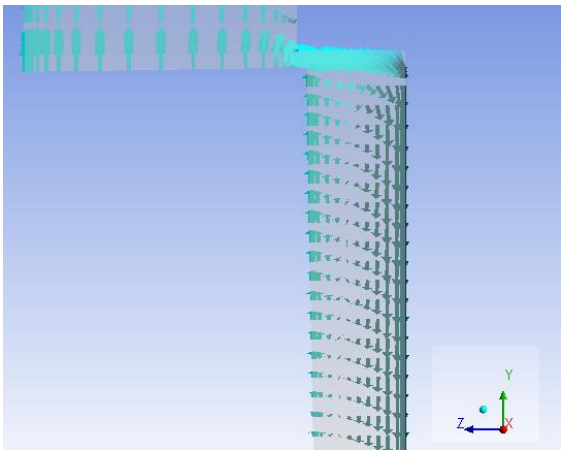

Fig. 43 Computed velocity vector at backshroud inlet

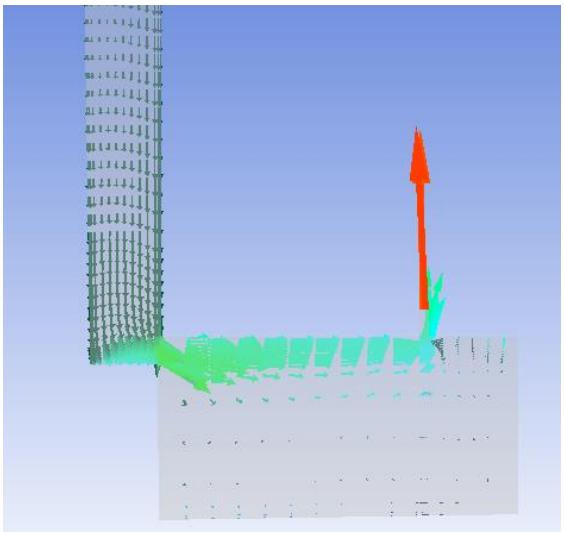

Fig. 44 Velocity vector at leakage flow path

Fig. 45 provides comparisons for the measured and predicted transverse moment coefficient and direct moment along with the curve-fits. The plot shows reasonable prediction in both moment coefficients and improved results compared to the bulk flow model. The rotordynamic coefficients from the curve-fits are summarized in Table 14. Comparisons to the experiment results of a precessing centrifugal impeller show good correlation.

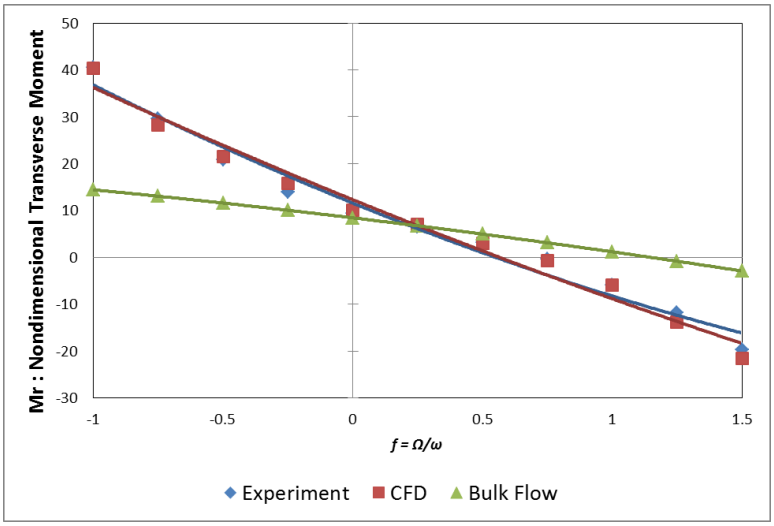

(a)

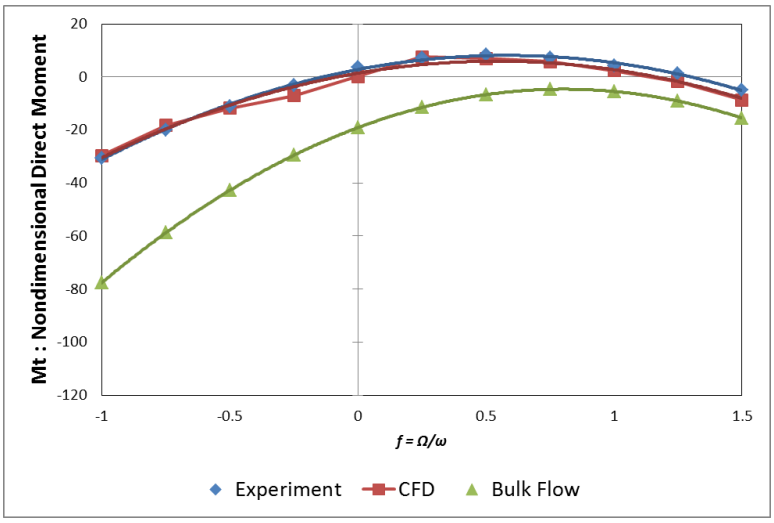

(b)

Fig. 45 Normalized moment components (a) Transverse moment (b) Direct moment

Table 14 Summary of predicted rotordynamic moment coefficients

	M_α (Kgm^2)	m_α (Kgm^2)	C_α (NmS/rad)	c_α (NmS/rad)	K_α (Nm/rad)	k_α (Nm/rad)	$\frac{k}{C\omega}$
CFX	2.93E-04	-2.66E-05	3.06E-02	2.25E-02	1.38E-01	1.18E+00	0.54
Experiment	3.20E-04	4.10E-06	2.20E-02	1.60E-02	2.58E-01	1.02E+00	0.65
Gupta (Bulk Flow) $\xi = 0.1$	4.30E-03	1.20E-05	9.00E-03	4.90E-02	-1.84E+00	8.11E-01	1.27

Since the leakage outlet path is not clear, the influence of the outlet gap is considered. Fig. 46 shows conceptual figure for changing outlet gap. The predicted impedance curves according to the inlet gap are shown in Fig. 47. As the gap is getting smaller, the direct moment coefficient is getting closer to the experiment result and the direct damping coefficient is increasing. In

Table 15, the rotordynamic coefficients are calculated from the curve-fit. With smaller outlet gap, the solved rotordynamic coefficients show good agreement with the experiment results.

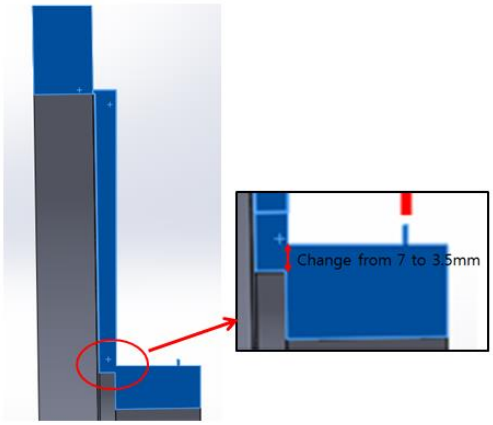

Fig. 46 Changing outlet gap for leakage flow

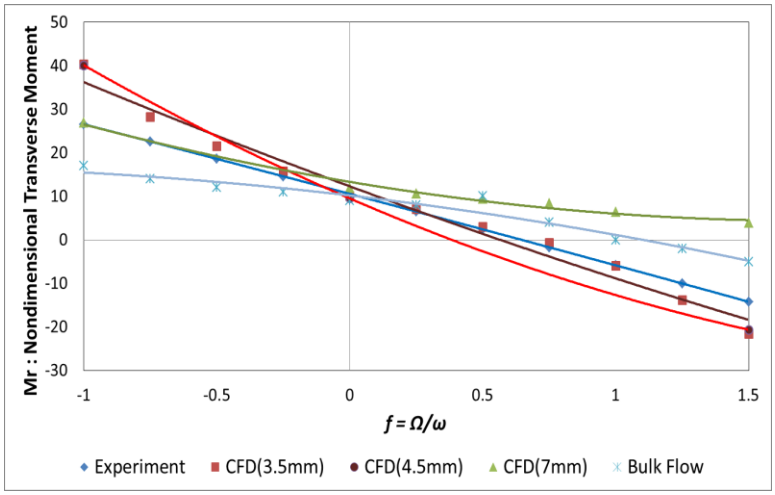

(a)

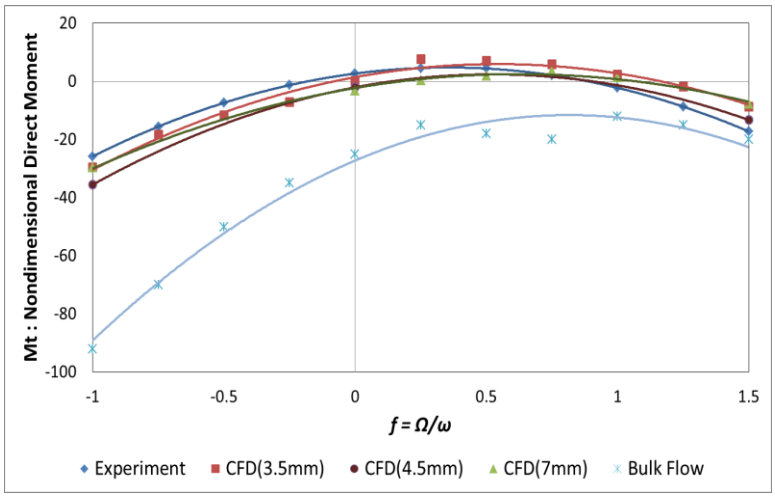

(b)

Fig. 47 Impedance curves according the inlet gap size (a) Transverse moment (b) Direct moment

Table 15 Predicted moment coefficients according to the outlet gap

	M_α (Kgm^2)	m_α (Kgm^2)	C_α (NmS/rad)	c_α (NmS/rad)	K_α (Nm/rad)	k_α (Nm/rad)	$\frac{k_\alpha}{C_\alpha \omega}$
CFD(7mm)	2.36E-04	-5.62E-05	1.39E-02	2.08E-02	-2.21E-01	1.28E+00	1.3
CFD(4.5mm)	3.11E-04	-4.76E-05	3.36E-02	2.36E-02	-2.46E-01	1.12E+00	0.47
CFX(3.5mm)	2.93E-04	-2.66E-05	3.06E-02	2.25E-02	1.38E-01	1.18E+00	0.54
Experiment	3.20E-04	4.10E-06	2.20E-02	1.60E-02	2.58E-01	1.02E+00	0.65
Gupta (Bulk Flow) $\xi = 0.1$	4.30E-03	1.20E-05	9.00E-03	4.90E-02	-1.84E+00	8.11E-01	1.27

7. PREDICTING ROTORDYNAMIC COEFFICIENTS FOR CIRCULAR AND CONICAL MOTION OF A SHROUDED CENTRIFUGAL IMPELLER

7.1 Circular and Conical Motion of Rotor

Childs [8] introduced an equation to describe the forces and moments of the impeller and Gupta [9] utilized the relation to predict a full set of the rotordynamic coefficients of a compressor stage. The linearized equations for circular and conical motion of a concentric impeller have the form of Eq. (81) and the circular and conical whirling motions are described in Fig. 48. In the equation, the reaction forces are caused by circular motion with coordinates (x, y) and the reaction moments are induced by conical motion with rotations (α_x, α_y).

$$
\begin{aligned}
-\begin{Bmatrix} F_X \\ F_Y \\ M_Y \\ M_X \end{Bmatrix} = &\begin{bmatrix} K & k & K_{\varepsilon\alpha} & -k_{\varepsilon\alpha} \\ -k & K & -k_{\varepsilon\alpha} & -K_{\varepsilon\alpha} \\ K_{\alpha\varepsilon} & k_{\alpha\varepsilon} & K_{\alpha} & -k_{\alpha} \\ k_{\alpha\varepsilon} & -K_{\alpha\varepsilon} & k_{\alpha} & K_{\alpha} \end{bmatrix} \begin{Bmatrix} X \\ Y \\ \alpha_Y \\ \alpha_X \end{Bmatrix} \\
&+ \begin{bmatrix} C & c & C_{\varepsilon\alpha} & -c_{\varepsilon\alpha} \\ -c & C & -c_{\varepsilon\alpha} & -C_{\varepsilon\alpha} \\ C_{\alpha\varepsilon} & c_{\alpha\varepsilon} & C_{\alpha} & -c_{\alpha} \\ c_{a\varepsilon} & -C_{\alpha\varepsilon} & c_{\alpha} & C_{\alpha} \end{bmatrix} \begin{Bmatrix} \dot{X} \\ \dot{Y} \\ \dot{\alpha}_Y \\ \dot{\alpha}_X \end{Bmatrix} \\
&+ \begin{bmatrix} M & m & M_{\varepsilon\alpha} & -m_{\varepsilon\alpha} \\ -m & M & -m_{\varepsilon\alpha} & -M_{\varepsilon\alpha} \\ M_{\alpha\varepsilon} & m_{\alpha\varepsilon} & M_{\alpha} & -m_{\alpha} \\ m_{a\varepsilon} & -M_{\alpha\varepsilon} & m_{\alpha} & M_{\alpha} \end{bmatrix} \begin{Bmatrix} \ddot{X} \\ \ddot{Y} \\ \ddot{\alpha}_Y \\ \ddot{\alpha}_X \end{Bmatrix}
\end{aligned}
\qquad \textbf{(81)}
$$

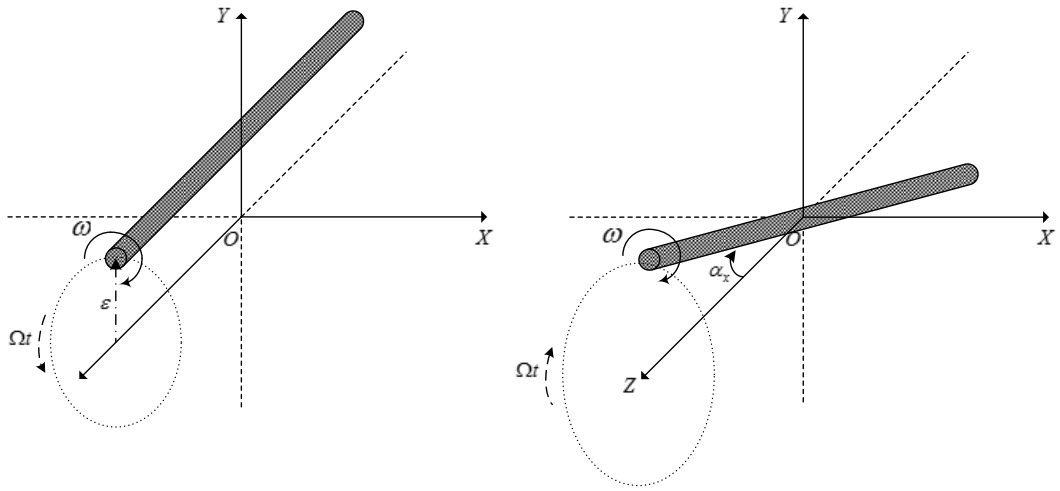

(a) (b)

Fig. 48 Configuration of whirling rotor (a) circular motion (b) conical motion

Rotordynamic coefficients for the whirling and precessing motions are defined by Childs **[8**]. The equations are:

For the whirling motion,

$$\begin{aligned} F_{r\_w} &= -K - c\,\Omega + M\Omega^2 \\ F_{t\_w} &= k + C\,\Omega + m\Omega^2 \\ M_{n\_w} &= K_{\alpha\varepsilon} + c_{\alpha\varepsilon}\,\Omega - M_{\alpha\varepsilon}\,\Omega^{2_2} \\ M_{t\_w} &= k_{\alpha\varepsilon} - C_{\alpha\varepsilon}\,\Omega^2 - m_{\alpha\varepsilon}\,\Omega \end{aligned} \qquad \textbf{(82)}$$

For the precessing motion,

$$\begin{aligned} F_{r\_p} &= -K_{\varepsilon\alpha} - c\,\Omega_{\varepsilon\alpha} + M_{\varepsilon\alpha}\Omega^2 \\ F_{t\_p} &= k_{\varepsilon\alpha} + C_{\varepsilon\alpha}\,\Omega + m_{\varepsilon\alpha}\Omega^2 \\ M_{n\_p} &= K_{\alpha} + c_{\alpha}\,\Omega - M_{\alpha}\,\Omega^{2_2} \\ M_{t\_p} &= k_{\alpha} - C_{\alpha}\,\Omega^2 - m_{\alpha}\,\Omega \end{aligned} \qquad \textbf{(83)}$$

7.2 Calculating a Full Set of Rotordynamic Coefficients

CFD models for the circular and conical motions of the face-seal impeller are constructed and simulated at multiple precession frequency ratios to obtain the full set of the rotordynamic coefficients. The imposed precession frequency ratios in the CFD model is ranging from -1.5 to 2.5. Fig. 49 and Fig. 50 contain impedances for eccentric motion and Fig. 51 and Fig. 52 contain impedances for tilting motion. For the tilting motion, the approach verified with the case by Yoshida et al. [7] is utilized. In contrast to the force impedances for the circular motion, the moment impedances and the force impedances for the conical motion have some bumps and dips in the impedance curves. Especially, the force impedances for the conical whirling motion have relatively larger bumps and dips than those of other impedances.

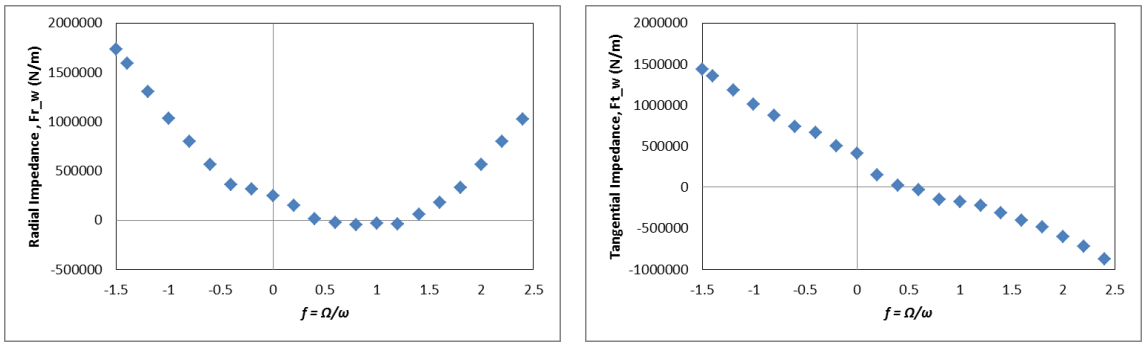

(a) (b)

Fig. 49 Force Impedances for circular whirling motion (a) radial (b) tangential

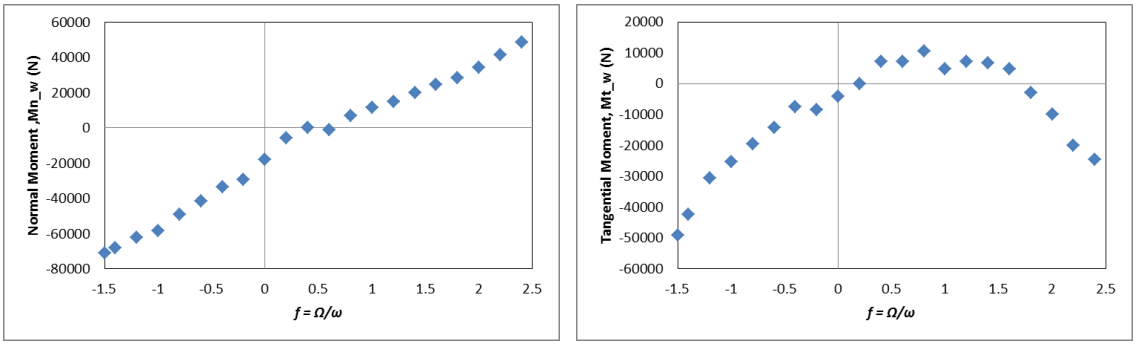

(a) (b)

Fig. 50 Moment impedances for circular whirling motion (a) transverse (b) direct

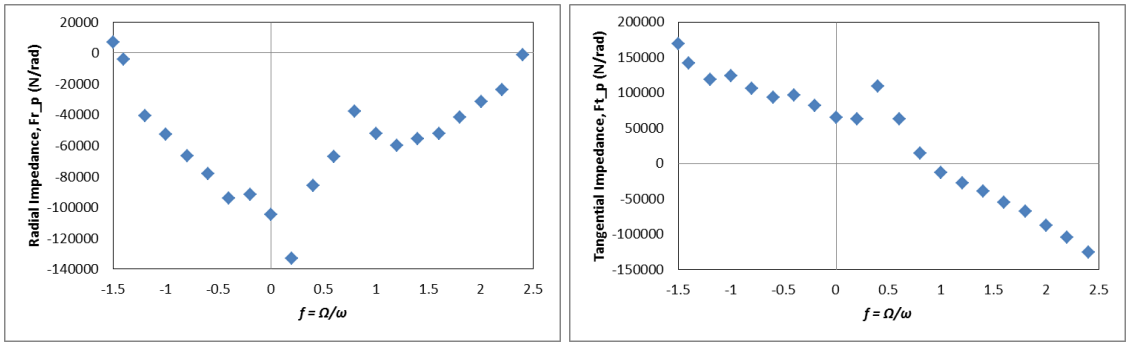

(a) (b)

Fig. 51 Force impedances for conical whirling motion (a) radial (b) tangential

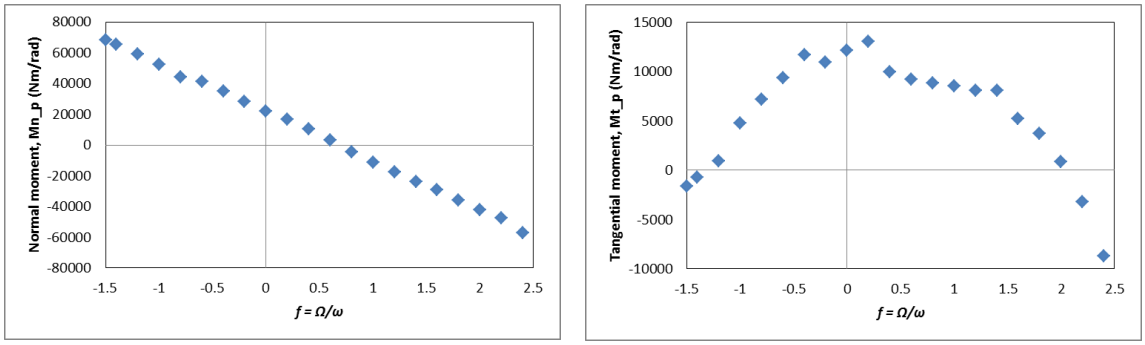

(a) (b)

Fig. 52 Moment impedances for conical whirling motion (a) transverse (b) direct

Table 16 gives the full set of the rotordynamic coefficients for the face-seal impeller. When comparing the dynamic coefficients between the circular motion and conical motion, the rotordynamic coefficients caused by the circular motion are relatively larger than those of the circular motion.

Table 16 Full set of the rotordynamic coefficients for face-seal impeller

K (N/m)	c $(N\cdot s/m)$	M (Kg)	k (N/m)	C $(N\cdot s/m)$	m (Kg)
-247181.00	3538.50	10.56	407424.00	4352.30	-6.06
$k_{\alpha\varepsilon}$ (N/m)	$C_{\alpha\varepsilon}$ $(N\cdot s)$	$m_{\alpha\varepsilon}$ $(N\cdot s^2)$	$K_{\alpha\varepsilon}$ (N)	$c_{\alpha\varepsilon}$ $(N\cdot s)$	$M_{\alpha\varepsilon}$ $(N\cdot s^2)$
-19346	-155.93	0.0521	1442.40	78.71	0.2627
$K_{\varepsilon\alpha}$ (N/rad)	$c_{\varepsilon\alpha}$ $(N\cdot s/rad)$	$M_{\varepsilon\alpha}$ $(Kg\cdot m)$	$k_{\varepsilon\alpha}$ (N/rad)	$C_{\varepsilon\alpha}$ $(N\cdot s/rad)$	$m_{\varepsilon\alpha}$ $(Kg\cdot m)$
84905.00	70.44	0.4910	74675.00	292.19	0.2113
k_{α} $(N\cdot m/rad)$	C_{α} $(N\cdot m\cdot s/rad)$	m_{α} $(Kg\cdot m^2)$	K_{α} $(N\cdot m/rad)$	c_{α} $(N\cdot m\cdot s/rad)$	M_{α} $(Kg\cdot m^2)$
21556.00	150.15	0.0033	11271.00	11.94	0.0932

7.3 Stability Analysis using 4×4 Rotordynamic Coefficients

Whirl frequency at instability is a useful coefficient to explain the rotordynamic instability of turbomachinery. The conventional whirl frequency ratio is defined as

$$f_w = \frac{k}{C\omega} \tag{84}$$

According to the test data for centrifugal pump impellers in Ref. [1, 4, 5, 6, 7], the calculated whirl frequency ratios are typically around 0.5. However, the whirl

frequency ratio of the face-seal impeller tested by Bolleter et al. [2] is $f_w = 0.94$ while the result of the current CFD model is $f_w = 0.45$.

For the explanation of the large whirl frequency ratio of Bolleter et al. [2], Childs [44] developed an analytical model for the reaction force and moments for circular and conical motion of pump-impeller-shroud surfaces. Following explanations show the procedure to derive the modified whirl frequency ratio at instability utilizing the full set of the rotordynamic coefficients.

Consider an operating impeller pitching up in a clockwise direction as it moves vertically upwards [44]. The complex motion can be described as shown in Fig. 48, and the motion is expressed by

$$Y = Y(t) : \alpha_x = -a_l Y, \;\; X(t) = \alpha_y(t) = 0 \tag{85}$$

where

$$a_l = \frac{\alpha}{\varepsilon}, \tag{86}$$

α : magnitude of rotation vector

ε : magnitude of eccentricity vector

The reaction force due to pitch and yaw motion is derived by substituting above equation in to 4by4 matrix equation as shown below:

$$
\begin{aligned}
-F_x &= kY - k_{\varepsilon\alpha}\alpha_x + c\dot{Y} - c_{\varepsilon\alpha}\dot{\alpha}_x + m\ddot{Y} - m_{\varepsilon\alpha}\ddot{\alpha}_x \\
&= (k + a_l k_{\varepsilon\alpha})Y + (c + a_l c_{\varepsilon\alpha})\dot{Y} + (m + a_l m_{\varepsilon\alpha})\ddot{Y}
\end{aligned}
\tag{87}
$$

$$
\begin{aligned}
-F_Y &= KY - K_{\varepsilon\alpha}\alpha_x + C\dot{Y} - C_{\varepsilon\alpha}\dot{\alpha}_x + M\ddot{Y} - M_{\varepsilon\alpha}\ddot{\alpha}_x \\
&= (K + a_l K_{\varepsilon\alpha})Y + (C + a_l C_{\varepsilon\alpha})\dot{Y} + (M + a_l M_{\varepsilon\alpha})\ddot{Y}_x
\end{aligned}
\tag{88}
$$

Ignoring the virtual-mass term m, the whirl frequency ratio for the pitch and yaw motion of the shrouded face-seal impeller can be expressed as

$$
f_{w\_\alpha} = \frac{(k + a_l k_{\varepsilon\alpha})}{\omega(C + a_l C_{\varepsilon\alpha})} = \frac{k}{C\omega}\frac{(1 + a_l \dfrac{k_{\varepsilon\alpha}}{k})}{(1 + a_l \dfrac{C_{\varepsilon\alpha}}{C})}
\tag{89}
$$

To evaluate the stability of the shroud face-seal impeller using the modified whirl frequency ratio at instability, the predicted rotordynamic coefficients in Table 16 are utilized. The detailed procedures are shown in the below:

The imposed dynamic eccentricity is $\varepsilon = 0.00062\,m$*, and the imposed tilting angle is 0.05 deg. Thus,* a_l *of Eq.* (86) *can be calculated as follows:*

$$
a_l = \frac{\alpha}{\varepsilon} = \frac{0.05\,\text{deg} \times [\dfrac{\pi}{180\,\text{deg}}]}{0.00062\,\text{m}} = 1.4075\,\text{rad/ m}
\tag{90}
$$

$$f_{w\_\alpha} = \frac{(k + a_l k_{\varepsilon\alpha})}{\omega(C + a_l C_{\varepsilon\alpha})} = \frac{k}{C\omega} \frac{(1 + a_l \frac{k_{\varepsilon\alpha}}{k})}{(1 + a_l \frac{C_{\varepsilon\alpha}}{C})} = 0.514 \quad \textbf{(91)}$$

By reviewing the calculated whirl frequency ratio in Eq. (91)*, it can be known that the coupled perturbation of the circular and conical whirling cause larger whirl frequency ratios. In the present study, the value increases by 12 %.*

7.4 Effect of Moment of Coupled Motion

Tsujimoto et al. [45, 45] introduced a novel approach to evaluate whirl and precession moment on the back shroud of centrifugal impeller. The author studied the influence of the whirling or precession moment on the rotordynamic stability. The moment coefficients were computed from the measured normal and tangential moment, and the values were utilized to figure out the effect of the whirl and precession moments in the rotordynamic stability analysis. Tsujimoto et al. [45, 46] considered a cantilevered rotor system using lumped parameter method to perform the stability analysis and showed: (i) The rotor motion is destabilizing when the normal moment has the same sign as the whirl/precession, and (ii) The precession moment is dominant on the system with the shorter shaft and the whirl moment has more influence on the longer shaft.

Tsujimoto's work showed that the moments from the whirling and precessing motion of the back shroud leakage path of the impeller can produce self-excited vibration of a vertical hydraulic pump or turbine. However, since the gyroscopic moment and the fluid forces were not considered in the vibration model, there might be a

limit to investigate the effect of the destabilizing motion caused by the whirling and precessing motion. Childs and Muhammed [47] reduced a 4 DOF model into two separate models of the displacement and the rotation using Guyan reduction. Model A that only considers displacements provide inconsistent instability requirement. However, Model B that only considers rotations showed consistent instability requirement with Tsujimoto's results.

The calculated 4×4 rotordynamic coefficients of Table 16 can be utilized for the analysis of the approaches developed by Tsujimoto et al. [45] and Childs and Muhammed [47].

7.5 Finite Element Rotordynamic Model with Coupled Motion

FE model with the force and moment coefficients of the shrouded face-seal impeller is constructed to evaluate the effect of the pitching and yawing motion as shown in Fig. 53. The calculated 4×4 coefficients of Table 16 are used to perform the stability analysis of the FE model. In the model, it is assumed that the impeller force and moment from the lateral and tilt motion of the impeller is acting on the 9^{th} node of the model. The system is supported by the flexible bearings placed at both ends and the face-seal impeller is modeled by a disk of 2-beam elements. The off-centered position of the disk is selected to check the effect of the tilt motion clearly.

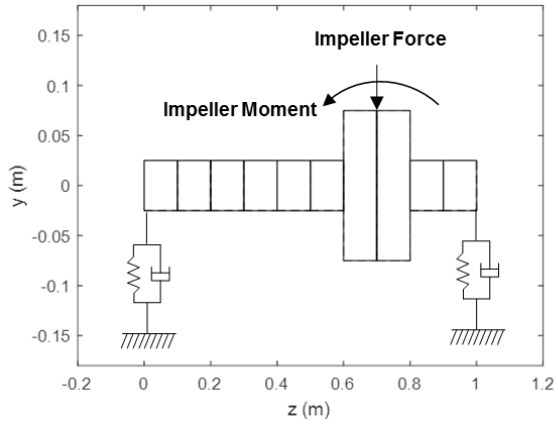

Fig. 53 Finite element model of rotor-bearing system with impeller whirling and precessing motion

7.6 Stability Analysis of FE Rotordynamic Model with Coupled Motion

The governing equation of the FE model is indicated in Eq. (36) and (37). In this chapter, the $[F_I]$ of Eq. (36) is changed to have impeller force and moment coefficients in the equation. An element vector of the changed $[F_I]$ at node No.9 of Fig. 53 can be expressed with mass, damping, and stiffness matrices and it has a form of

$$\begin{aligned}[F_{I9}] = &-\begin{bmatrix} M & -m_{\varepsilon\alpha} & m & M_{\varepsilon\alpha} \\ m_{\alpha\varepsilon} & M_a & -M_{\alpha\varepsilon} & m_\alpha \\ -m & -M_{\varepsilon\alpha} & M & -m_{\varepsilon\alpha} \\ M_{\alpha\varepsilon} & -m_\alpha & m_{\alpha\varepsilon} & M_\alpha \end{bmatrix} \begin{Bmatrix} \ddot{x}_9 \\ \ddot{\theta}_{x9} \\ \ddot{y}_9 \\ \ddot{\theta}_{y9} \end{Bmatrix} \\ &-\begin{bmatrix} C & -c_{\varepsilon\alpha} & c & C_{\varepsilon\alpha} \\ c_{\alpha\varepsilon} & C_a & -C_{\alpha\varepsilon} & c_\alpha \\ -c & -C_{\varepsilon\alpha} & C & -c_{\varepsilon\alpha} \\ C_{\alpha\varepsilon} & -c_\alpha & c_{\alpha\varepsilon} & C_\alpha \end{bmatrix} \begin{Bmatrix} \dot{x}_9 \\ \dot{\theta}_{x9} \\ \dot{y}_9 \\ \dot{\theta}_{y9} \end{Bmatrix} - \begin{bmatrix} K & -k_{\varepsilon\alpha} & k & K_{\varepsilon\alpha} \\ k_{\alpha\varepsilon} & K_a & -K_{\alpha\varepsilon} & k_\alpha \\ -k & -K_{\varepsilon\alpha} & K & -k_{\varepsilon\alpha} \\ K_{\alpha\varepsilon} & -k_\alpha & k_{\alpha\varepsilon} & K_\alpha \end{bmatrix} \begin{Bmatrix} x_9 \\ \theta_{x9} \\ y_9 \\ \theta_{y9} \end{Bmatrix} \end{aligned} \quad \textbf{(92)}$$

The second order matrix-vector differential equation in Eq. (36) can be written in first order differential equation form as

$$\begin{bmatrix} [M_{tot}] & 0 \\ 0 & -[K_{tot}] \end{bmatrix} \begin{bmatrix} \{\ddot{z}\} \\ \{\dot{z}\} \end{bmatrix} + \begin{bmatrix} [C_{tot}] & [K_{tot}] \\ [K_{tot}] & 0 \end{bmatrix} \begin{bmatrix} \{\ddot{z}\} \\ \{\dot{z}\} \end{bmatrix} = \begin{bmatrix} \{F_u\} \\ 0 \end{bmatrix} \tag{93}$$

where

$$\begin{aligned} [M_{tot}] &= [M_I] \\ [C_{tot}] &= [C_B] + [C_G] + [C_I] \\ [K_{tot}] &= [K_B] + [K_S] + [K_I] \end{aligned} \tag{94}$$

In Eq. (101), $[M_I]$, $[C_I]$, and $[K_I]$ are mass, damping, and stiffness matrix of the applied impeller force and moment on the FE rotor model of Fig. 53. By matrix operation, Eq. (101) can be transformed as

$$\begin{bmatrix} \{\ddot{z}\} \\ \{\dot{z}\} \end{bmatrix} = \begin{bmatrix} -[M_{tot}]^{-1}[C_{tot}] & -[M_{tot}]^{-1}[K_{tot}] \\ [I] & 0 \end{bmatrix} \begin{bmatrix} \{\ddot{z}\} \\ \{\dot{z}\} \end{bmatrix} + \begin{bmatrix} [M_{tot}]^{-1}\{F_u\} \\ 0 \end{bmatrix} \tag{95}$$

Eq. (102) is used to obtain the eigenvalues and eigenvectors of the FE rotor model with whirling and precessing impeller. The bearing stiffness and damping coefficients of the FE model with impeller whirling and precessing motion are calculated by utilizing the rotor/disk mass and the assumed natural frequency. The calculated rotor/disk mass from the FE model of Fig. 53 and the assumed natural frequency values are

m_s =30.66 Kg, ω_n =80 rad/s **(96)**

The utilized parameters for the calculation of the rotor/disk mass and the simulation of the FE model are shown in Table 17. The bearing stiffness coefficient (K_b) and the bearing damping coefficient (C_b) can be calculated from the rotor/disk mass, the assumed natural frequency and the bearing damping ratio as shown in Eq. (104) .

$$K_b = m_s \omega_n^2 \quad , \; C_b = 2 m_s \omega_n \zeta \qquad \textbf{(97)}$$

Table 17 Simulation parameters of the Rotor-Bearing Model with the lateral and tilt motion of the face-seal impeller

Parameters	Values
Young's modulus (Pa)	2×10^{11}
Density (kg / m^3)	8000
Length of shaft (m)	1.0
Length of disk (m)	0.14
Diameter of shaft (m)	0.1
Diameter of disk (m)	0.3
Unbalance eccentricity of disk (m)	0.36×10^{-4}

Fig. 54 and Fig. 55 indicate the mode shapes of the FE model of Fig. 53 when $\zeta = 0.2$, $K_b = 0.196\ MN/m$, $C_b = 981.18\ N \cdot S/m$ and the rotor spin speed is 2,000 rpm. In order to investigate the stability of the FE rotor model, simulations are performed by varying the bearing damping ratio (ζ) and comparisons are made for the calculated log-dec values according to the applied impeller loads as shown in Fig. 56. The damped natural frequencies for the cases are indicated in Fig. 57. In the results, it

can be known that the rotor model goes unstable at $\zeta = 0.04$ when 4×4 full coefficients are applied in the rotor model and the damped natural frequency is 108.4 rad/s.

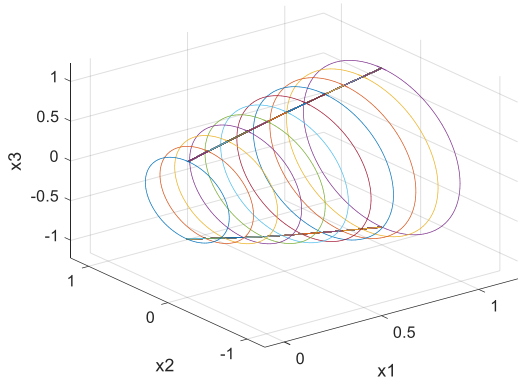

Fig. 54 1st mode shape of FE rotor model with the lateral and tilt motion, rotating at 2000 rpm, $\zeta = 0.04$, $K_b = 0.196\ MN/m$, $C_b = 196.24\ N \cdot S/m$, $\omega_{d1} = 108.4\, rad/s$, $\delta = -0.026$

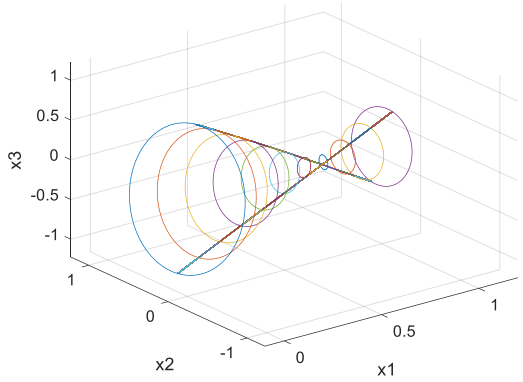

Fig. 55 2nd mode shape of FE rotor model with the lateral and tilt motion, rotating at 2000 rpm, $\zeta = 0.04$, $K_b = 0.196\ MN/m$, $C_b = 196.24\ N \cdot S/m$, $\omega_{d1} = 236.32\, rad/s$, $\delta = 0.92$

In Fig. 56, the results of 'force coeff.' have relatively larger logarithmic decrement values than the results of '4×4 full coeff.' and the differences are too large to neglect. This suggests that the tilted motion of the impeller can make the FE rotor model of Fig. 53 more unstable and the effect of the tilted motion can be considered as a crucial factor to evaluate the rotordynamic stability.

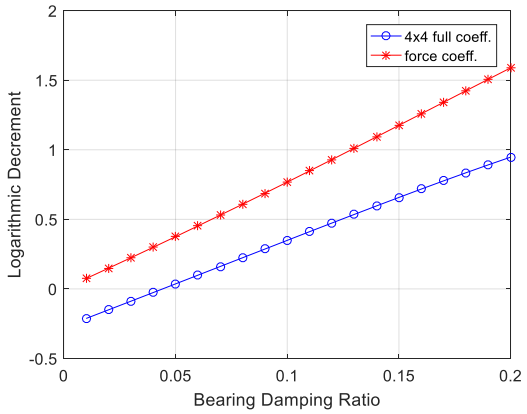

Fig. 56 Log-dec versus bearing damping ratio ζ comparisons according to the applied load for 2,000 rpm

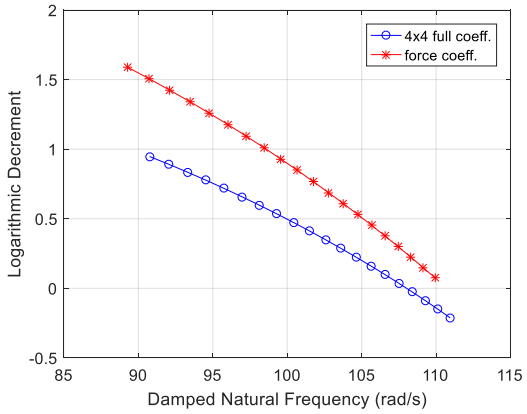

Fig. 57 Log-dec versus damped natural frequency (rad/s) according to the applied rotordynamic coefficients

In addition to the positive tilted angle of the rotor, negative tilted angle of α_l in Eq. (89) is also considered by suggestion [48]. With the negative value of a_l, the value of f_{w_α} in Eq. (89) decreases by 0.35 and this implies that the impeller motion becomes more stable than the impeller motion with positive angle or without angle. This tendency can be evaluated using FE rotor model in the following analysis.

Negative tilted angle of a_l in FE model in Fig. 53 can occur if the location of the disk moves to the opposite side as shown in Fig. 58 when considering flexible rotor motion. The FE rotor model of Fig. 58 is simulated to investigate the effect of the sign of tilting angle by varying the bearing damping ratio. The utilized parameters for the simulation are same with the FE rotor model of Fig. 53 as shown in Table 17.

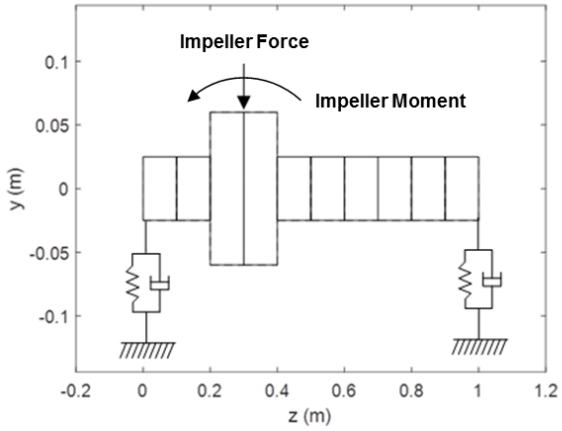

Fig. 58 Finite element model of rotor-bearing system with impeller whirling and precessing motion for negative tilted angle of impeller

The calculated logarithmic decrement values according to the applied load in the FE rotor model of Fig. 58 is shown in Fig. 59 and the corresponding damped natural

frequencies are indicated in Fig. 60. Both cases in Fig. 59 have positive log-dec values and the results of '4×4 full coeff.' are larger than the results of 'force coeff.'. This indicates that the stability of the FE rotor model with the negative tilted angle becomes more stable and this tendency is identical with the stability prediction using f_{w_α} of Eq. (89) suggested by Childs [44].

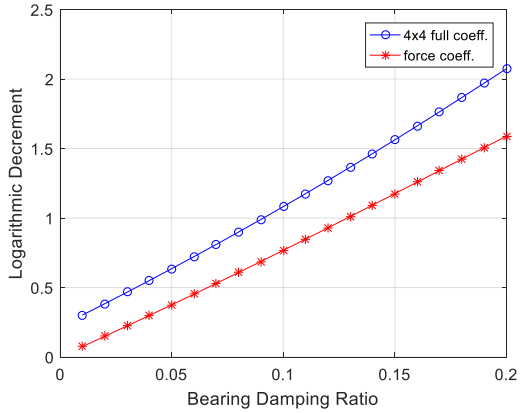

Fig. 59 Log-dec versus bearing damping ratio ζ comparisons according to the applied load for 2,000 rpm for negative tilted angle of impeller

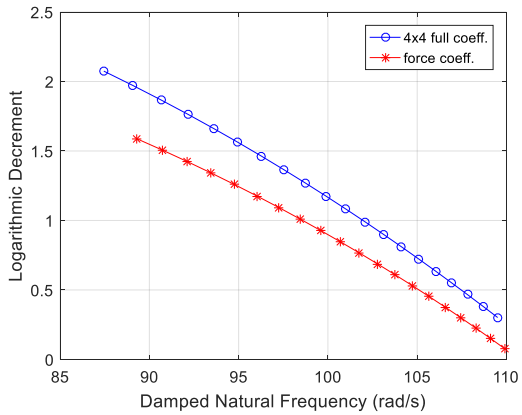

Fig. 60 Log-dec versus damped natural frequency (rad/s) according to the applied rotordynamic coefficients for negative tilted angle of impeller

7.7 Rotordynamic Coefficients for Coupled Motion

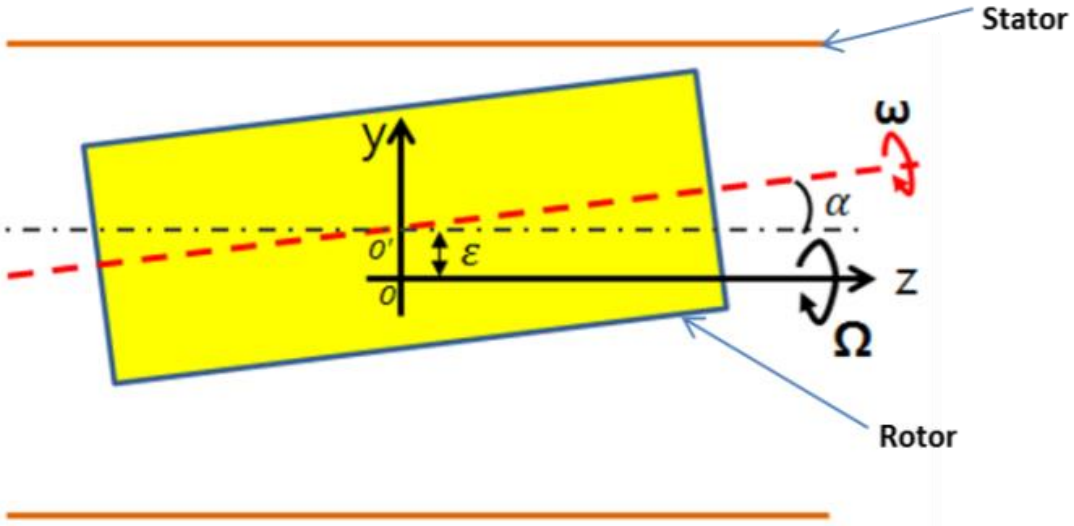

Fig. 61 Whirling and precessing motion

Tilting motion with the dynamic eccentricity would typically occur in a pump or compressor due to the flexible rotor bending. Fig. 61 shows the coupled motion of whirling with dynamic eccentricity ε, and precessing with tiling angle α. In the present study, face-seal impeller models with 10% dynamic eccentricity and 0.025/0.05° inclinations are modeled to investigate the effect of the precessing motion on the rotordynamic stability. The pitch angles are selected by considering the rub avoidance and the feasibility of the mesh generation in the small gap between the face-seal and stator. The utilized boundary conditions are same as the model with only whirling motion as shown in Table 3. The calculated radial and tangential impedances are shown in Fig. 62. In order to evaluate the effect of the tilted angle, 0deg, 0.025deg, and 0.05deg cases are compared.

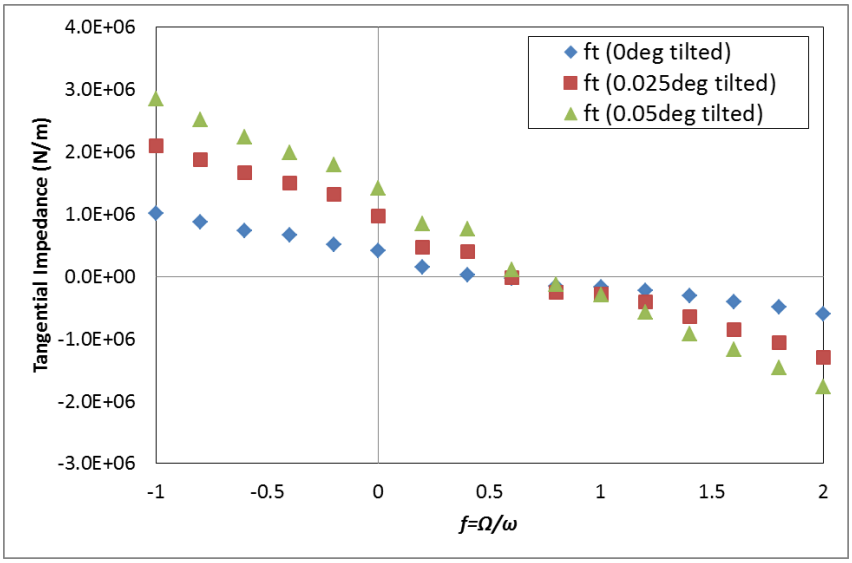

(a)

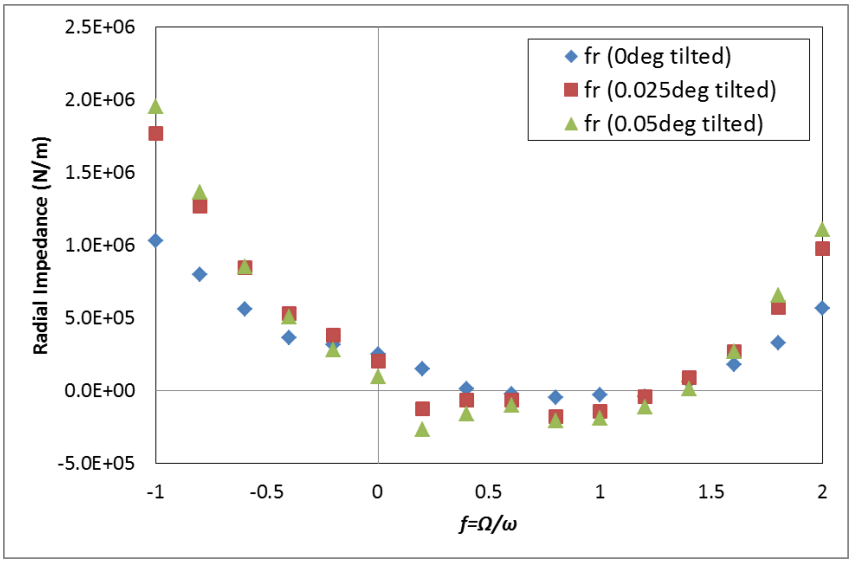

(b)

Fig. 62 Impedances versus PFR(*f=Ω/ω)* for the whirling and precessing face-seal impeller (a) tangential (b) radial

Table 18 Rotordynamic force coefficients for the whirling and precessing impeller

Angle	M_{EA} (Kg)	m_{EA} (Kg)	C_{EA} $(N \cdot s/m)$	c_{EA} $(N \cdot s/m)$	K_{EA} (N/m)	k_{EA} (N/m)
0 °	10.56	-6.06	4352.3	3538.5	-247181	407424
0.025 °	15.598	-3.27	6289.8	4768.2	-176950	842523
0.05 °	17.036	-3.67	8804.13	4886.7	-78217	1324460

Table 19 Whirl frequency ratio at instability according to the tilted angle

	0 (no angle)	0.025 °	0.05 °
$\frac{k_{EA}}{C_{EA}\omega}(=f_{w\_EA})$	$(\frac{k}{C\omega}=)0.45$	0.64	0.72

Although the impedance curves have some inflection points, they can be modeled by a MCK quadratic model of Eq. (98).

$$\frac{F_{r\_EA}}{\varepsilon_{EA}} = -K_{EA} - c_{EA}\Omega + M_{EA}\Omega^2$$
$$\frac{F_{t\_EA}}{\varepsilon_{EA}} = k_{EA} - C_{EA}\Omega - m_{EA}\Omega^2 \quad \textbf{(98)}$$

Subscript, ‘EA’, in the above equations indicates the coupled motion of the whirling and precessing. Since the 3D model for the coupled motion doesn’t have constant eccentricity because of the tilted angle, the minimum eccentric value, ε_{EA}, in the

3D model is utilized to calculate the rotordynamic coefficients. ε_{EA} is $0.00032\,[m]$ for 0.025° and ε_{EA} is $0.00028\,[m]$ for 0.05° . The rotordynamic force coefficients for the whirling and precessing motions are calculated using 2nd order curve-fit and shown in Table 18. The whirl frequency ratio at instability for each case is calculated using the corresponding coefficients and compared in Table 19. As shown in the table, the whirl frequency ratio at instability is increasing as the imposed angle increases. This relationship between the tilted angle and the whirl frequency at instability was estimated in the model developed by Childs [44]. The increased whirl frequency ratio at instability for larger tilted angle of the impeller indicate that the impeller is more destabilizing for the larger pitching(precessing) motion. This is identical with the destabilizing mechanism introduced and studied in Refs [44 - 46].

8. ROTORDYNAMIC FORCE PREDICTION FOR ECCENTRIC IMPELLER

8.1 Modeling of Orbiting Rotor at Statically Eccentric Position

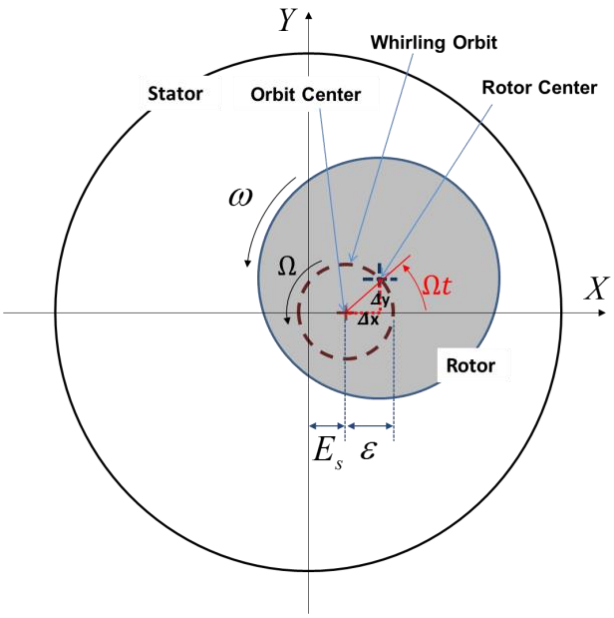

Fig. 63 Schematic of a whirling rotor motion about an eccentric position

An approach is developed to predict the rotordynamic coefficients of eccentric annular seals using CFD. Fig. 63 shows the schematic of a whirling rotor motion about an eccentric position. The reaction forces acting on the whirling rotor about a non-centered position can be expressed as

$$-\begin{Bmatrix}\Delta F_x\\ \Delta F_y\end{Bmatrix}=\begin{bmatrix}K_{xx}(E_s) & k_{xy}(E_s)\\ -k_{yx}(E_s) & K_{yy}(E_s)\end{bmatrix}\begin{Bmatrix}\Delta x\\ \Delta y\end{Bmatrix}+\begin{bmatrix}C_{xx}(E_s) & c_{xy}(E_s)\\ -c_{yx}(E_s) & C_{yy}(E_s)\end{bmatrix}\begin{Bmatrix}\Delta \dot{x}\\ \Delta \dot{y}\end{Bmatrix}+\begin{bmatrix}M_{xx}(E_s) & m_{xy}(E_s)\\ -m_{yx}(E_s) & M_{yy}(E_s)\end{bmatrix}\begin{Bmatrix}\Delta \ddot{x}\\ \Delta \ddot{y}\end{Bmatrix} \quad \textbf{(99)}$$

In the equation above, E_s is the static eccentricity of the rotor. Δx and Δy are rotor displacements from the steady-state position. The displacements are expressed as

$$\Delta x = \varepsilon \cos \Omega t$$
$$\Delta y = \varepsilon \sin \Omega t \quad \textbf{(100)}$$

where, ε is the whirling orbit radius.

The forces, ΔF_x and ΔF_y, in Eq. (99) are indicating the reaction forces caused by the whirling motion about the whirling orbit center. When the rotor is operating with the whirling motion about the misaligned position, the reaction forces can be divided into two kinds of independent forces according to their sources. They are (1) forces resulted from the whirling along the orbit radius, ε (2) forces caused by only the misaligned position which can be also defined as non-vibrating forces. Fig. 64 shows the forces acing on the rotor according to the position of the rotor. Fig. 65 indicates the forces when the rotor is operating without whirling motion at static eccentric position. In the figures, the static eccentricity is imposed along the x-axis.

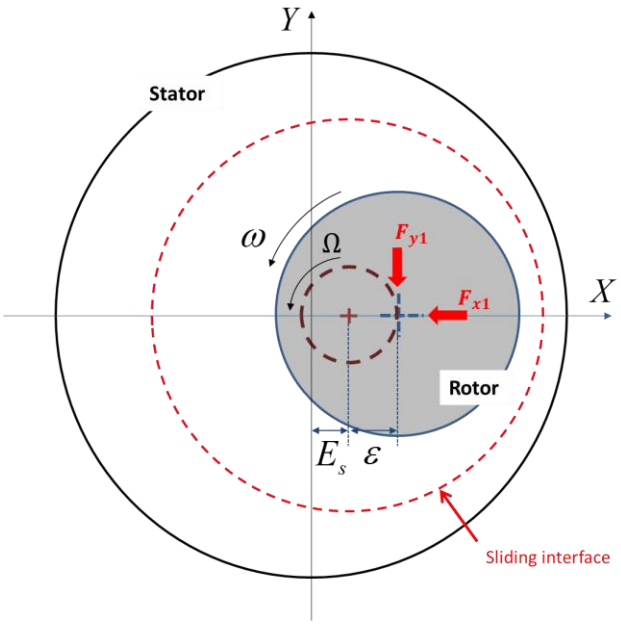

(a)

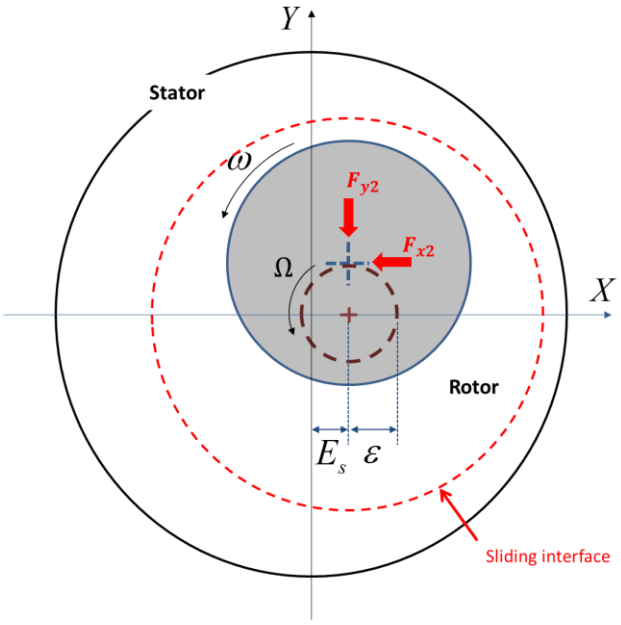

(b)

Fig. 64 Forces acing on the rotor by whirling motion at static eccentric position (a) $\Omega t = 0$ **(b)** $\Omega t = \frac{\pi}{2}$

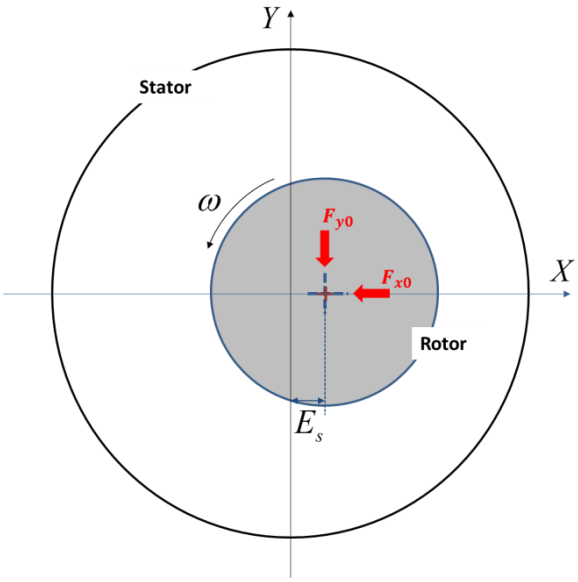

Fig. 65 Forces acing on the rotor at static eccentric position without whirling motion

In order to calculate the reaction forces in Eq. (99), non-vibrating forces at the static eccentric position of the rotor should be subtracted from the forces induced by the whirling motion about the static eccentric position. The forces of Eq. (99) are obtained according to the position of the rotor. For each position, ΔF_x and ΔF_y are calculated by

At $\Omega t = 0$

$$\begin{aligned} \Delta F_x &= F_{x1} - F_{x0} \\ \Delta F_y &= F_{y1} - F_{y0} \end{aligned} \tag{101}$$

At $\Omega t = \frac{\pi}{2}$

$$\begin{aligned} \Delta F_x &= F_{x2} - F_{x0} \\ \Delta F_y &= F_{y2} - F_{y0} \end{aligned} \tag{102}$$

The rotordynamic coefficients for the static eccentricity should be calculated for $\Omega t = 0$ and $\Omega t = \pi / 2$ because the motion of the whirling rotor about the static eccentric position is not axisymmetric. By substituting Eq. (100) into Eq. (99), the reaction forces on the rotor according to its position are defined as below.

At $\Omega t = 0$

$$\begin{aligned} -\frac{\Delta F_x}{\varepsilon} &= K_{xx} + c_{xy}\Omega - M_{xx}\Omega^2 \\ -\frac{\Delta F_y}{\varepsilon} &= -k_{yx} + C_{yy}\Omega + m_{yx}\Omega^2 \end{aligned} \quad \textbf{(103)}$$

At $\Omega t = \pi / 2$

$$\begin{aligned} -\frac{\Delta F_x}{\varepsilon} &= k_{xy} - C_{xx}\Omega - m_{xy}\Omega^2 \\ -\frac{\Delta F_y}{\varepsilon} &= K_{yy} + c_{yx} - M_{yy}\Omega^2 \end{aligned} \quad \textbf{(104)}$$

8.2 CFD Approach for Static Eccentricity

Though ANSYS CFX is only capable of solving axisymmetric model, an approximated model can be created for the simulation of the static eccentric case which is asymmetric. Fig. 64 illustrates a whirling rotor about a position misaligned statically. Ω is the whirling frequency and ω is the spin speed of the misaligned whirling rotor. A sliding surface is generated between the rotor surface and the stator surface. The center of the sliding surface is identical to the center of the whirling motion. Outer region divided by the sliding surface should be defined as a stationary frame while the inner region is defined as a rotating frame. The inner rotating frame makes the whirling motion of the rotor and causes fluid rotation between the rotor and stator. The

rotordynamic coefficients for the static eccentricity of the rotor can be calculated by varying the precession frequency ratio of the inner rotating frame.

8.3 Case Studies for Verification

8.3.1 Test Case by Falco et al. [23]

In order to validate the CFD approach for the rotordynamic coefficients caused by the static eccentricity, comparisons with experimental data of Falco et al. [23] are made in Fig. 66 and Fig. 67. The eccentric seal parameters are shown in Table 20.

Table 20 Eccentric seal data of Falco et al. [23]

Seal Geometry	
Length	4.0 cm
Radius	8.0 cm
Nominal clearance	0.36 mm
Fluid properties & Operating conditions	
Density	1000 kg / m^3
Viscosity	10E-3 $N s / m^2$
Pressure drop	1 MPa
Rotor angular speed	4000 rpm
Inlet pre-swirl ratio	0.3
Inlet loss coefficients	0.3

For the case, Falco et al. [23] analyzed the annular seal using the Reynolds-equation based FE solution and Nelson et al. [25] developed bulk flow code with Moody

friction model for eccentric seals. Those previous results are compared with the current CFD results to validate the approach. The predicted rotordynamic coefficients using CFD model show reasonable results and follow similar trend when comparing with the results of others. The calculated stiffness values of 0 and 0.5 eccentric ratio cases are close to the results of experiment. However, 0.7 eccentric ratio results are relatively larger than others except for k_{xy}.

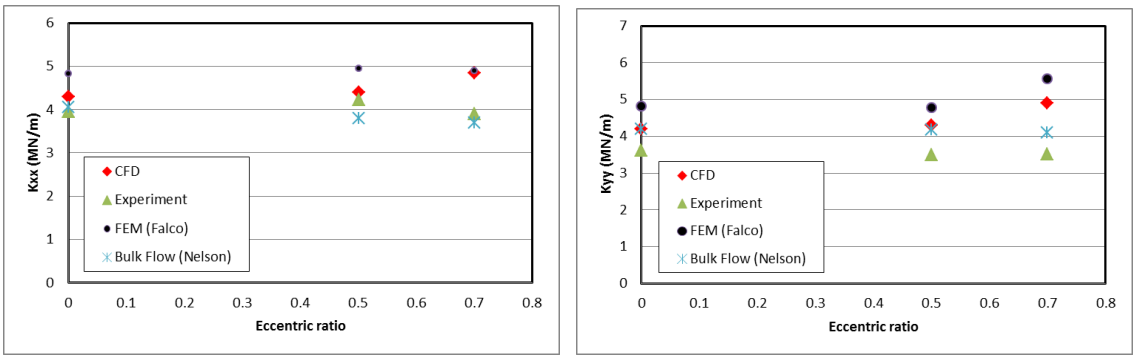

(a) (b)

Fig. 66 Direct stiffness vs. eccentric ratio (a) K_{xx} (b) K_{yy}

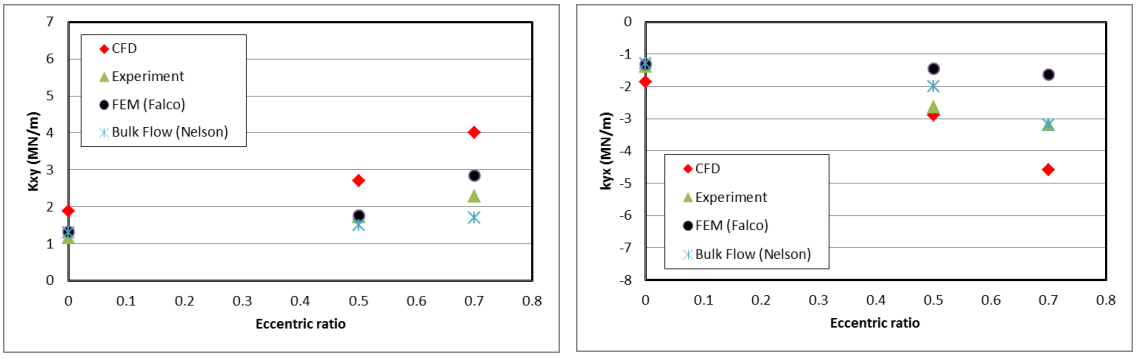

(a) (b)

Fig. 67 Cross-coupled stiffness vs. eccentric ratio (a) k_{xy} (b) k_{yx}

8.3.2 Eccentric Seal of Allaire et al. [27]

Allaire et al. [27] examined the effect of the eccentric seals using short seal solution. Direct stiffness, damping and cross-coupled stiffness are compared with the previous results [24, 25, 27, and 28]. The seal parameters are shown in Table 21. Comparisons in Fig. 68 show that all of the approaches predict similar results for the eccentric seal.

Table 21 Eccentric seal data of Allaire et al. [27]

Seal Geometry	
Length	40.6 mm
Radius	39.9 cm
Nominal clearance	0.14 mm
Fluid properties & Operating conditions	
Density	57.657 kg / m^3
Viscosity	7.4396E-6 $N s / m^2$
Pressure drop	7.26 MPa
Rotor angular speed	23700 rpm
Inlet pre-swirl ratio	0.3
Inlet loss coefficients	0.10

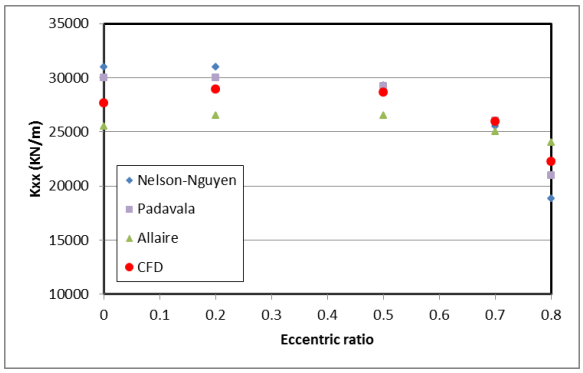

(a)

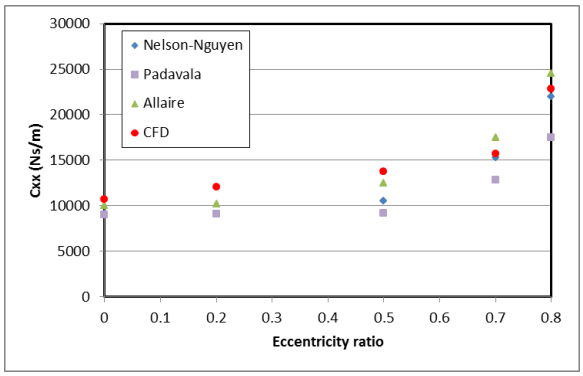

(b)

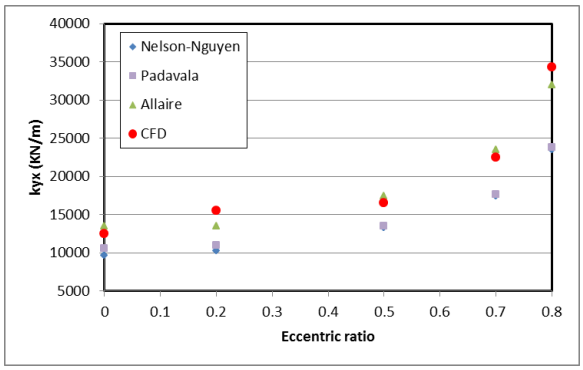

(c)

Fig. 68 rotordynamic coefficients vs. eccentric ratio (a) direct stiffness (b) direct damping (c) cross-coupled stiffness

8.4 Rotordynamic Coefficients for Statically Eccentric Impeller

The impedances of the face-seal impeller for the static eccentricity are calculated for $\Omega t = 0$ and $\Omega t = \pi / 2$. The boundary conditions are same with the concentric case of Table 3. The investigated precession frequency ratios are ranging from -3.0 to 3.0 as shown in Fig. 69 and Fig. 70. Bump and dip are observed in the impedance curves and their sizes are increasing for the larger static eccentricity. For the static eccentricity cases, the rotordynamic coefficients cannot be calculated because of the bump and dip and therefore the rotordynamic stability for the static eccentricity of the shroud will be investigated using the transfer function model.

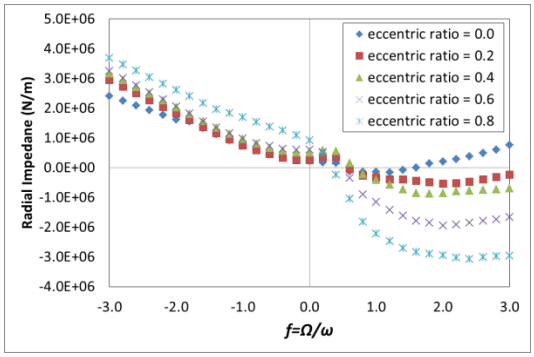

(a)

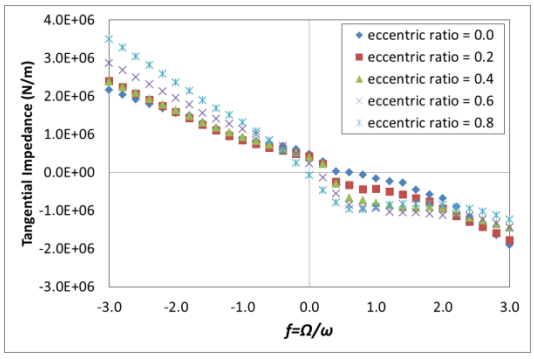

(b)

Fig. 69 Impedances of the whirling shroud about the statically eccentric center at $\Omega t = 0$ (a) ΔF_x (b) ΔF_y

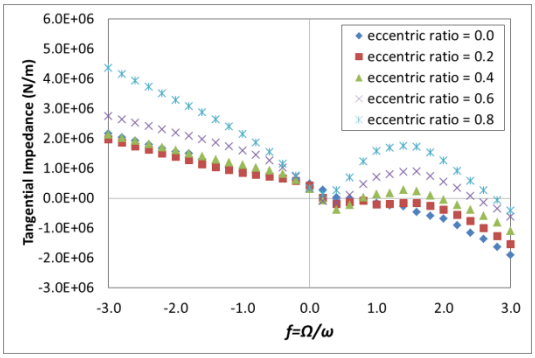

(a)

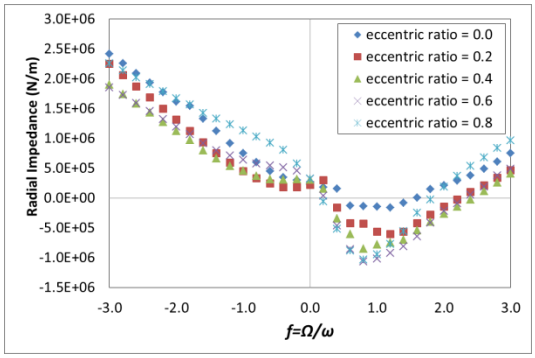

(b)

Fig. 70 Impedances of the whirling shroud about the statically eccentric center at $\Omega t = \frac{\pi}{2}$ (a) ΔF_x (b) ΔF_y

8.5 Curve-Fits for Identification of Unconventional Impedances

In this chapter, rotordynamic stability analysis is performed using the transfer function model. Eq. (53) has a form of skew symmetry because the center of the whirling motion is same with the center of the stator center. However, the whirling motion about the statically eccentric position is asymmetric and therefore the reaction forces acting on the statically eccentric shroud should be changed in the form of equation shown in the below:

$$
\begin{aligned}
-\begin{Bmatrix} F_x \\ F_y \end{Bmatrix} &= \begin{bmatrix} a_0 & b_0 \\ c_0 & d_0 \end{bmatrix}\begin{Bmatrix} x \\ y \end{Bmatrix} + \begin{bmatrix} a_1 & b_1 \\ c_1 & d_1 \end{bmatrix}\begin{Bmatrix} \dot{x} \\ \dot{y} \end{Bmatrix} + \begin{bmatrix} a_2 & b_2 \\ c_2 & d_2 \end{bmatrix}\begin{Bmatrix} \ddot{x} \\ \ddot{y} \end{Bmatrix} + \\
&\begin{bmatrix} a_3 & b_3 \\ c_3 & d_3 \end{bmatrix}\begin{Bmatrix} \dddot{x} \\ \dddot{y} \end{Bmatrix} + \begin{bmatrix} a_4 & b_4 \\ c_4 & d_4 \end{bmatrix}\begin{Bmatrix} x^{(4)} \\ y^{(4)} \end{Bmatrix} + \cdots + \begin{bmatrix} a_n & b_n \\ c_n & d_n \end{bmatrix}\begin{Bmatrix} x^{(n)} \\ y^{(n)} \end{Bmatrix} \\
&= \sum_{i=0}^{n} \begin{bmatrix} a_i & b_i \\ c_i & d_i \end{bmatrix}\begin{Bmatrix} x^{(\mathrm{i})} \\ y^{(\mathrm{i})} \end{Bmatrix}
\end{aligned}
\tag{105}
$$

Eq. (51) indicates the fluid forces and the resultant responses for harmonic, steady state vibration of frequency Ω. By substituting Eq. (51) into Eq. (105), the forces in x and y direction become

$$
\begin{aligned}
-\begin{Bmatrix} \bar{F}_x \\ \bar{F}_y \end{Bmatrix} e^{j\Omega t} &= \begin{bmatrix} a_0 & b_0 \\ c_0 & d_0 \end{bmatrix}\begin{Bmatrix} \bar{x} \\ \bar{y} \end{Bmatrix} e^{j\Omega t} + \begin{bmatrix} a_1 & b_1 \\ c_1 & d_1 \end{bmatrix}\begin{Bmatrix} \bar{x} \\ \bar{y} \end{Bmatrix}\left(j\,\Omega e^{j\Omega t} \right) \\
&+ \begin{bmatrix} a_2 & b_2 \\ c_2 & d_2 \end{bmatrix}\begin{Bmatrix} \bar{x} \\ \bar{y} \end{Bmatrix}\left(-\Omega^2 e^{j\Omega t} \right) + \begin{bmatrix} a_3 & b_3 \\ c_3 & d_3 \end{bmatrix}\begin{Bmatrix} \bar{x} \\ \bar{y} \end{Bmatrix}\left(-j\,\Omega^3 e^{j\Omega t} \right) \\
&+ \begin{bmatrix} a_4 & b_4 \\ c_4 & d_4 \end{bmatrix}\begin{Bmatrix} \bar{x} \\ \bar{y} \end{Bmatrix}\left(\Omega^4 e^{j\Omega t} \right) + \cdots + \begin{bmatrix} a_n & b_n \\ c_n & d_n \end{bmatrix}\begin{Bmatrix} \bar{x} \\ \bar{y} \end{Bmatrix}\left(\left(j\,\Omega \right)^n e^{j\Omega t} \right) \\
&= \sum_{i=0}^{n} \begin{bmatrix} a_i & b_i \\ c_i & d_i \end{bmatrix}\begin{Bmatrix} \bar{x} \\ \bar{y} \end{Bmatrix}\left(\left(j\,\Omega \right)^i e^{j\Omega t} \right)
\end{aligned}
\tag{106}
$$

The impeller fluid forces can be expressed with four different impedance functions, $D_{xx}(j\Omega)$, $D_{xy}(j\Omega)$, $D_{yx}(j\Omega)$, and $D_{yy}(j\Omega)$ in the frequency domain as shown below:

$$
-\begin{bmatrix} F_x \\ F_y \end{bmatrix} = \begin{bmatrix} D_{xx}(j\Omega) & D_{xy}(j\Omega) \\ D_{yx}(j\Omega) & D_{yy}(j\Omega) \end{bmatrix}\begin{bmatrix} x \\ y \end{bmatrix} \tag{107}
$$

where

$$
\begin{aligned}
D_{xx}(j\Omega) &= \left(a_0 - a_2\Omega^2 + a_4\Omega^4 - \cdots\right) + j\left(a_1\Omega - a_3\Omega^3 + a_5\Omega^5 - \cdots\right) \\
D_{xy}(j\Omega) &= \left(b_0 - b_2\Omega^2 + b_4\Omega^4 - \cdots\right) + j\left(b_1\Omega - b_3\Omega^3 + b_5\Omega^5 - \cdots\right) \\
D_{yx}(j\Omega) &= \left(c_0 - c_2\Omega^2 + c_4\Omega^4 - \cdots\right) + j\left(c_1\Omega - c_3\Omega^3 + c_5\Omega^5 - \cdots\right) \\
D_{yy}(j\Omega) &= \left(d_0 - d_2\Omega^2 + d_4\Omega^4 - \cdots\right) + j\left(d_1\Omega - d_3\Omega^3 + d_5\Omega^5 - \cdots\right)
\end{aligned}
\qquad \textbf{(108)}
$$

By considering the shaft center of Eq. (55), the radial and tangential impedances can be obtained for $\Omega t = 0$ and $\Omega t = \dfrac{\pi}{2}$ as follows:

At $\Omega t = 0$,

$$
-\begin{Bmatrix} F_x(0) \\ F_y(0) \end{Bmatrix} = \begin{bmatrix} a_0 & b_0 \\ c_0 & d_0 \end{bmatrix}\begin{Bmatrix} r \\ 0 \end{Bmatrix} + \begin{bmatrix} a_1 & b_1 \\ c_1 & d_1 \end{bmatrix}\begin{Bmatrix} 0 \\ r\Omega \end{Bmatrix} + \begin{bmatrix} a_2 & b_2 \\ c_2 & d_2 \end{bmatrix}\begin{Bmatrix} -r\Omega^2 \\ 0 \end{Bmatrix} + \begin{bmatrix} a_3 & b_3 \\ c_3 & d_3 \end{bmatrix}\begin{Bmatrix} 0 \\ -r\Omega^3 \end{Bmatrix} + \begin{bmatrix} a_4 & b_4 \\ c_4 & d_4 \end{bmatrix}\begin{Bmatrix} r\Omega^4 \\ 0 \end{Bmatrix} + \cdots \qquad \textbf{(109)}
$$

or;

$$
-\begin{Bmatrix} I_{xx} \\ I_{yx} \end{Bmatrix} = -\begin{Bmatrix} F_x(0)/r \\ F_y(0)/r \end{Bmatrix} = \begin{bmatrix} a_0 + b_1\Omega - a_2\Omega^2 - b_3\Omega^3 + a_4\Omega^4 + \cdots \\ c_0 + d_1\Omega - c_2\Omega^2 - d_3\Omega^3 + c_4\Omega^4 + \cdots \end{bmatrix} \qquad \textbf{(110)}
$$

At $\Omega t = \dfrac{\pi}{2}$,

$$
-\begin{Bmatrix} F_x\left(\pi/2\right) \\ F_y\left(\pi/2\right) \end{Bmatrix} = \begin{bmatrix} a_0 & b_0 \\ c_0 & d_0 \end{bmatrix}\begin{Bmatrix} 0 \\ r \end{Bmatrix} + \begin{bmatrix} a_1 & b_1 \\ c_1 & d_1 \end{bmatrix}\begin{Bmatrix} -r\Omega \\ 0 \end{Bmatrix} + \begin{bmatrix} a_2 & b_2 \\ c_2 & d_2 \end{bmatrix}\begin{Bmatrix} 0 \\ -r\Omega^2 \end{Bmatrix} + \begin{bmatrix} a_3 & b_3 \\ c_3 & d_3 \end{bmatrix}\begin{Bmatrix} r\Omega^3 \\ 0 \end{Bmatrix} + \begin{bmatrix} a_4 & b_4 \\ c_4 & d_4 \end{bmatrix}\begin{Bmatrix} 0 \\ r\Omega^4 \end{Bmatrix} + \cdots \qquad \textbf{(111)}
$$

or;

$$
-\begin{Bmatrix} I_{xy} \\ I_{yy} \end{Bmatrix} = -\begin{Bmatrix} F_x\left(\pi/2\right)/r \\ F_y\left(\pi/2\right)/r \end{Bmatrix} = \begin{bmatrix} b_0 - a_1\Omega - b_2\Omega^2 + a_3\Omega^3 + b_4\Omega^4 + \cdots \\ d_0 - c_1\Omega - d_2\Omega^2 + c_3\Omega^3 + d_4\Omega^4 + \cdots \end{bmatrix} \qquad \textbf{(112)}
$$

From Eq. (108), (109), (110), (111), and (112), the radial and tangential impedances for the forward and backward whirl can be determined using

$$I_{xx}^{+}(\Omega) = -\mathrm{Re}\left[D_{xx}(j\Omega)\right] - \mathrm{Im}\left[D_{xy}(j\Omega) \right]$$
$$I_{xx}^{-}(\Omega) = -\mathrm{Re}\left[D_{xx}(j\Omega)\right] + \mathrm{Im}\left[D_{xy}(j\Omega) \right] \quad \textbf{(113)}$$

$$I_{xy}^{+}(\Omega) = -\mathrm{Re}\left[D_{xy}(j\Omega)\right] + \mathrm{Im}\left[D_{xx}(j\Omega) \right]$$
$$I_{xy}^{-}(\Omega) = -\mathrm{Re}\left[D_{xy}(j\Omega)\right] - \mathrm{Im}\left[D_{xx}(j\Omega) \right] \quad \textbf{(114)}$$

$$I_{yx}^{+}(\Omega) = -\mathrm{Re}\left[D_{yx}(j\Omega)\right] - \mathrm{Im}\left[D_{yy}(j\Omega) \right]$$
$$I_{yx}^{-}(\Omega) = -\mathrm{Re}\left[D_{yx}(j\Omega)\right] + \mathrm{Im}\left[D_{yy}(j\Omega) \right] \quad \textbf{(115)}$$

$$I_{yy}^{+}(\Omega) = -\mathrm{Re}\left[D_{yy}(j\Omega)\right] + \mathrm{Im}\left[D_{yx}(j\Omega) \right]$$
$$I_{yy}^{-}(\Omega) = -\mathrm{Re}\left[D_{yy}(j\Omega)\right] - \mathrm{Im}\left[D_{yx}(j\Omega) \right] \quad \textbf{(116)}$$

Complex impedances, $D_{xx}(j\Omega)$, $D_{xy}(j\Omega)$, $D_{yx}(j\Omega)$, and $D_{yy}(j\Omega)$ can be calculated using the relationship in Eq.(113) – Eq. (116). To identifiy the complex impedances, the curve-fits are performed using multi-segment approach developed in Chapter 5. The curve-fits have been performed for various eccentric ratios. The ratios are ranging from 0 to 0.8 and the results are shown in Fig. 71 - Fig. 75. Goodness-of-fit for each result is indicated by R^2 values and the quality of the curve fits are good enough to utilize in the stability analysis of the Jeffcott rotor model.

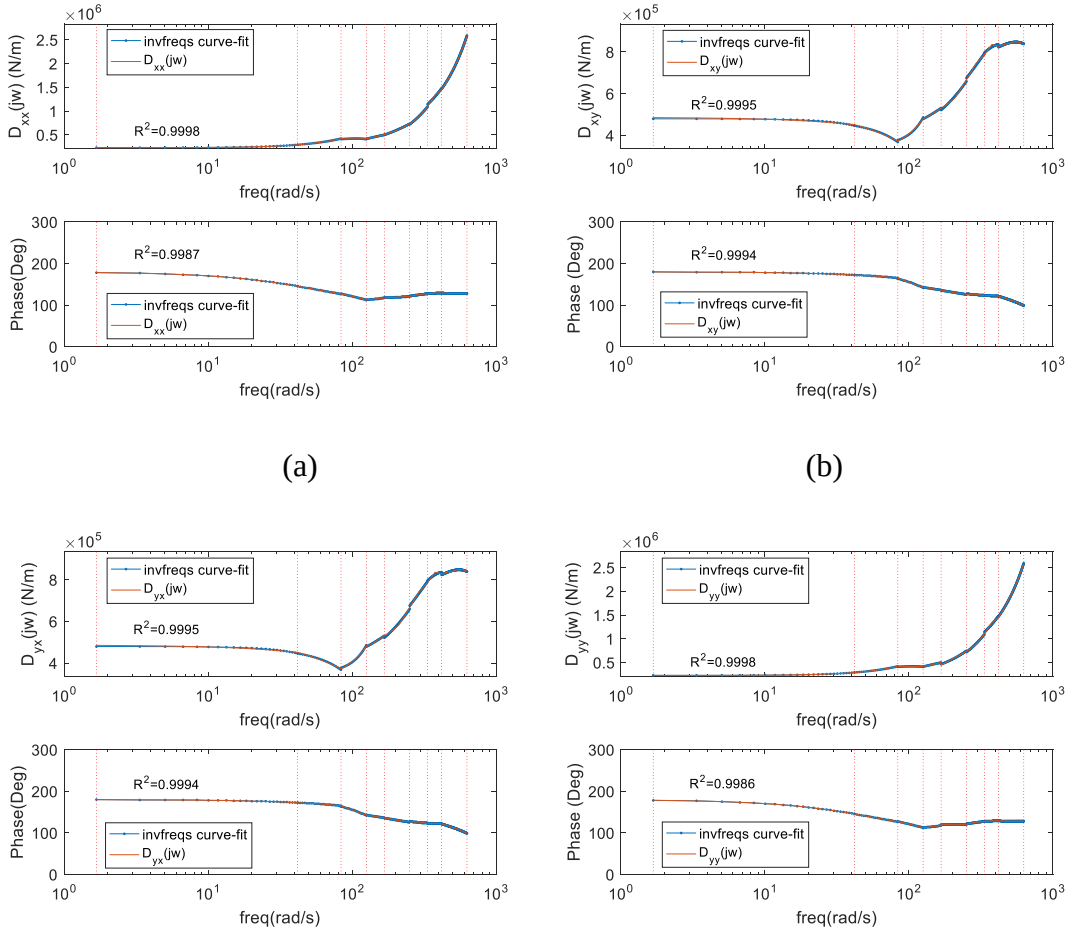

Fig. 71 Curve fit results of 0.0 eccentric ratio case by transfer function model with segmentation (a) $D_{xx}(j\Omega)$ **(b)** $D_{xy}(j\Omega)$ **(c)** $D_{yx}(j\Omega)$ **(d)** $D_{yy}(j\Omega)$

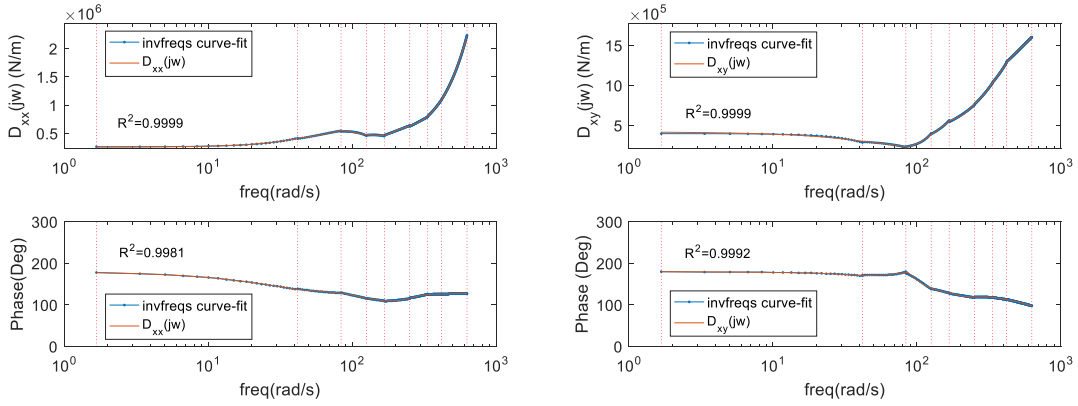

(a) (b)

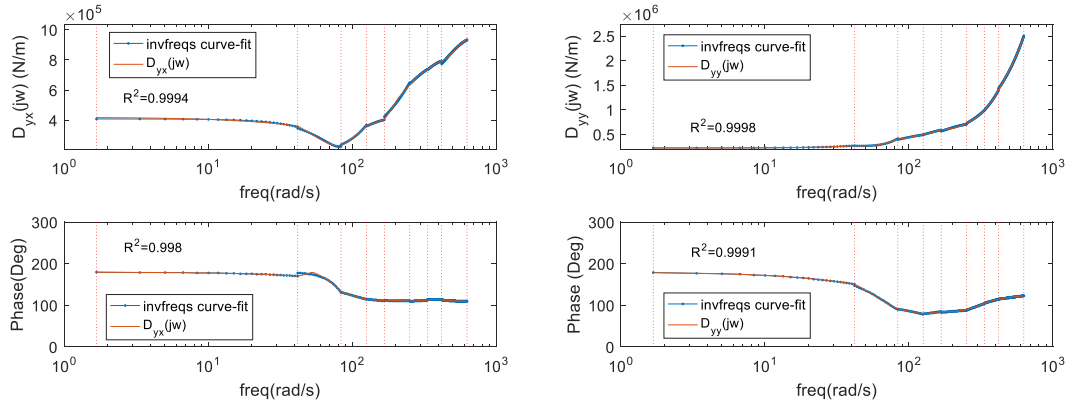

(c) (d)

Fig. 72 Curve fit results of 0.2 eccentric ratio case by transfer function model with segmentation (a) $D_{xx}(j\Omega)$ **(b)** $D_{xy}(j\Omega)$ **(c)** $D_{yx}(j\Omega)$ **(d)** $D_{yy}(j\Omega)$

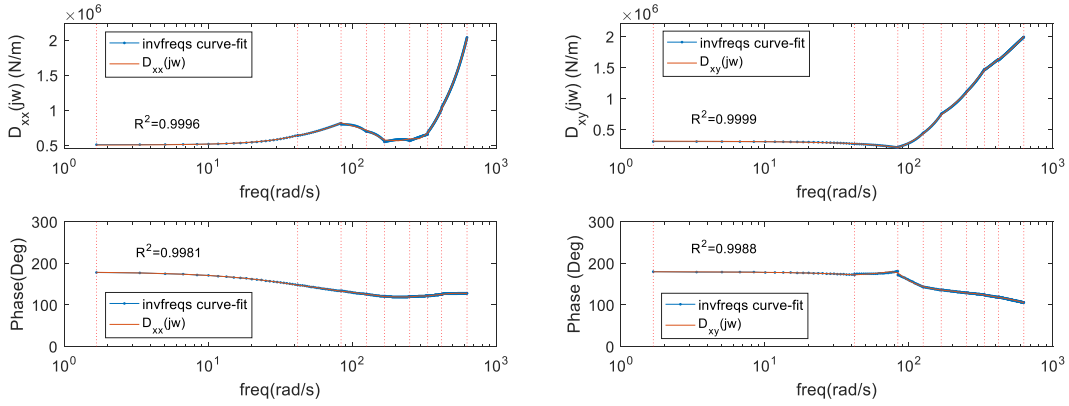

(a)

(b)

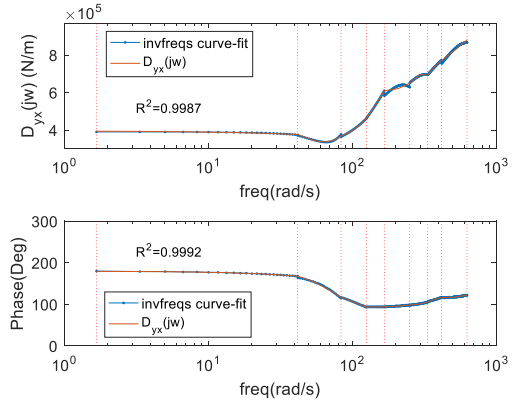

(c)

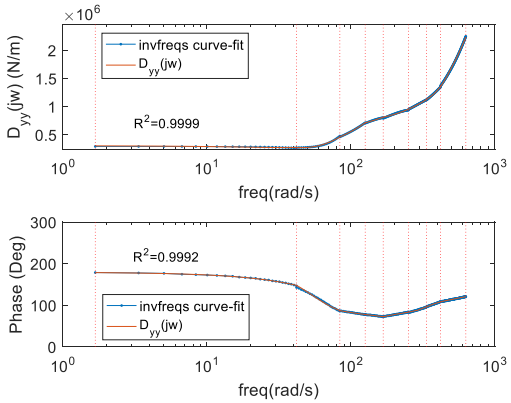

(d)

Fig. 73 Curve fit results of 0.4 eccentric ratio case by transfer function model with segmentation (a) $D_{xx}(j\Omega)$ **(b)** $D_{xy}(j\Omega)$ **(c)** $D_{yx}(j\Omega)$ **(d)** $D_{yy}(j\Omega)$

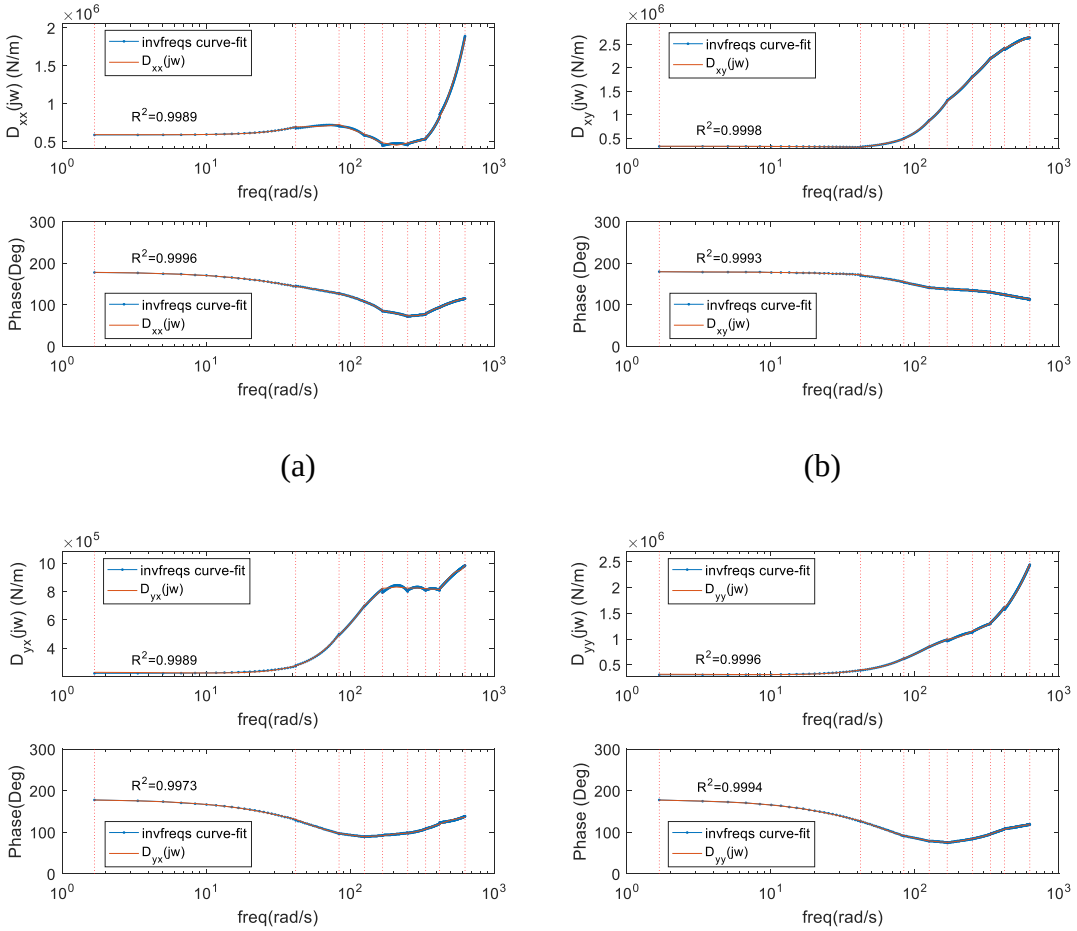

Fig. 74 Curve fit results of 0.6 eccentric ratio case by transfer function model with segmentation (a) $D_{xx}(j\Omega)$ **(b)** $D_{xy}(j\Omega)$ **(c)** $D_{yx}(j\Omega)$ **(d)** $D_{yy}(j\Omega)$

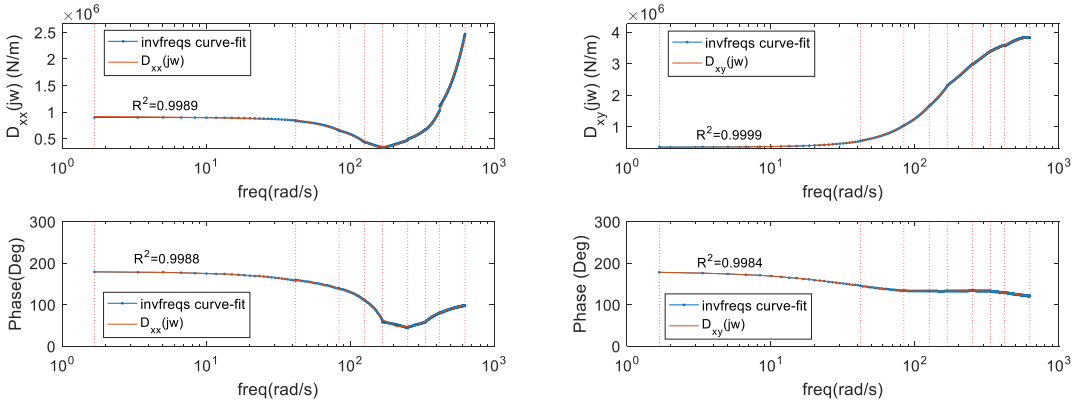

(a)

(b)

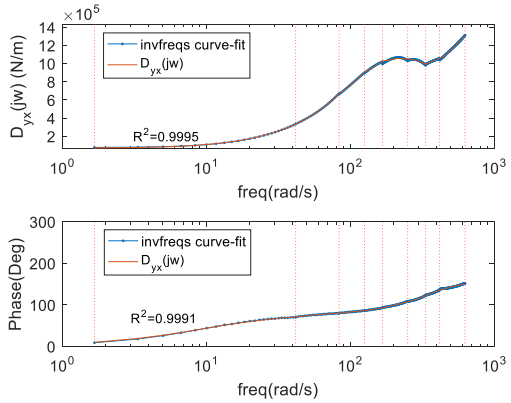

(c)

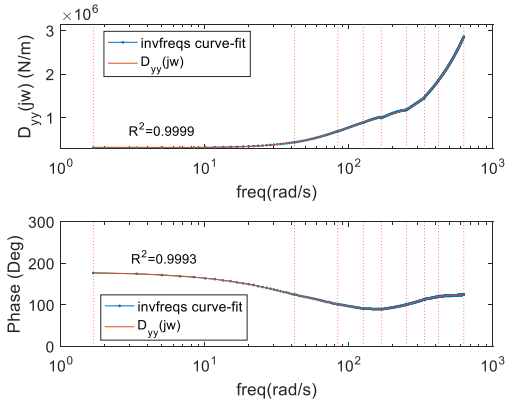

(d)

Fig. 75 Curve fit results of 0.6 eccentric ratio case by transfer function model with segmentation (a) $D_{xx}(j\Omega)$ **(b)** $D_{xy}(j\Omega)$ **(c)** $D_{yx}(j\Omega)$ **(d)** $D_{yy}(j\Omega)$

8.6 Stability Analysis of Simplified Jeffcott Rotor Model with Statically Eccentric Impedance

In order to evaluate the stability of the statically eccentric impeller, a simplified Jeffcott rotor is also considered in this chapter. The jeff-cott rotor model with the centrifugal impedances using the transfer function model is illustrated in Eq. (59). In the equations, $T_{xx}(s)$, $T_{xy}(s)$, $T_{yx}(s)$, and $T_{yy}(s)$ for the complex impedances of the statically eccentric impedances are defined as follows:

$$\begin{aligned} &T_{xx}(s) = D_{xx}(s)x(s),\ T_{xy}(s) = D_{xy}(s)y(s), \\ &T_{yx}(s) = -D_{yx}(s)x(s),\ T_{yy}(s) = D_{yy}(s)y(s) \end{aligned} \quad \textbf{(117)}$$

For the analysis, the selected mass and natural frequency of the Jeffcott rotor model is

$$m_d = 120 \text{ Kg},\ \omega_n = 480 \text{ rad/s} \quad \textbf{(118)}$$

A comparison of log-dec according to the eccentric ratio is in Fig. 76. For the given parameters of Eq. (118), log-dec is decreasing when the eccentric ratio is increasing. The deviation of log-dec in Fig. 76 is small because the magnitudes of the complex impedances are relatively small when considering the mass of the Jeffcott rotor. In order to investigate the effect of the static eccentricity, the mass is changed to 20 Kg and the log-dec values are calculated and compared in Fig. 77. With the decreased mass, the deviation of log-dec is increasing and it can be concluded that larger static eccentricity has a negative effect on the stability of the Jeffcott rotor.

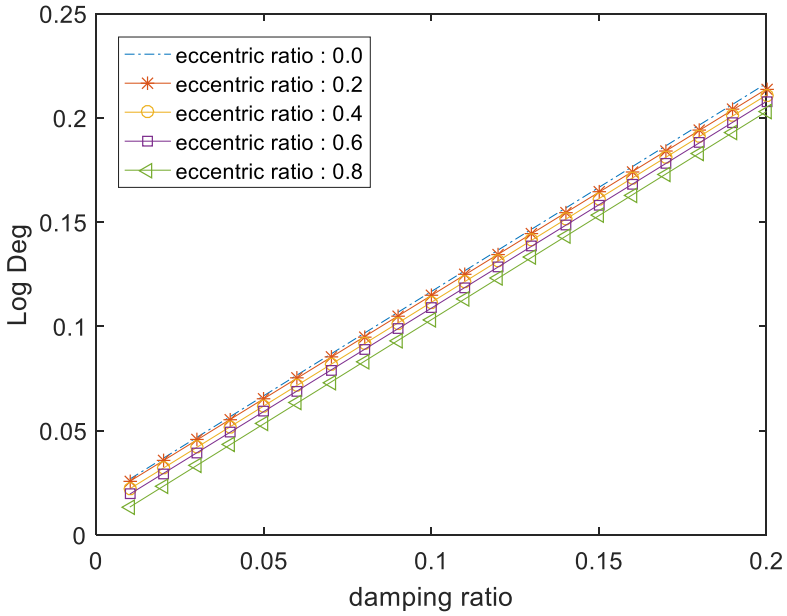

Fig. 76 Comparison of log-dec according to the eccentric ratio for m_d =120 Kg

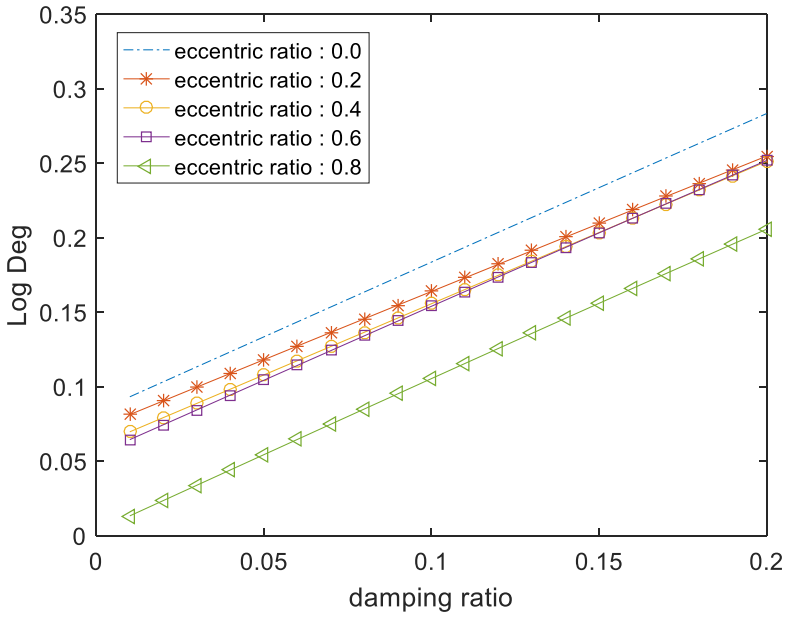

Fig. 77 Comparison of log-dec according to the eccentric ratio for m_d =20 Kg

9. CONCLUSION

The fluid induced forces arising in the leakage flow path of the shrouded face-seal impeller and the conventional wear-ring seal impeller have been investigated utilizing the CFD approach. ANSYS CFX is employed to predict the rotordynamic forces caused by a whirling centrifugal impeller by considering various operating motions and the corresponding resultant impedances are analyzed utilizing the newly developed linear curve-fit approach.

First of all, the computational approach is verified by reasonable prediction of the rotordynamic coefficients for the face-seal impeller as compared with other approaches and experiment. A wide range of precession frequency ratios (-1.5 ~ 2.0) are considered to check the existence of the bump and dip in the impedance curves of the face-seal impeller case. The conventional quadratic least square curve-fit approach can be used to determine the rotordynamic coefficients of the face-seal impeller since there are no significant bump and dip in the impedance curves. Using the validated approach, a conventional wear-ring seal impeller is analyzed and the radial and tangential impedances are computed. The results of the simulation show peaks in the impedances which have not been observed in the prior CFD models, but have appeared in the bulk flow impeller analysis of Childs. Review of past experimental work also shows the peaks in measured impeller impedances. Inlet swirl ratio, flow rate of primary passage, shape of shroud, and seal clearance are varied to analyze their effects in the conventional wear-ring seal impeller impedances. The impedances from the seal are relatively larger

than the values from the shroud of the conventional wear-ring seal impeller. The bump and dip in the impedance curves of the impeller are caused mainly by forces originating in the shroud rather than the seal. The phenomenon is clearly observed in the tangential impedance. The bump and dip in the predicted impedance curves increase with higher inlet swirl ratio. The wear-ring seal impeller is less destabilizing and the size of the impedance peaks decrease at higher flow rate of the primary passage. The trend is identical to the results of the experiment by Franz et al. **[15**]. Added recirculation zones in the leakage flow path reduce the velocity of the circumferential direction in the shroud surface and the magnitude of the impedance peaks. With larger added area in the shroud leakage path, the peaks in the impedance curves can be suppressed more effectively. Leakage flow rate is reduced with the additional recirculation zone. Enlarging the seal clearance of the impeller is one method to reduce the size of the dip and bump. However, using a larger clearance seal in the impeller model has the negative effect of increasing the leakage flow rate.

Secondly, rotordynamic stability analysis has been performed using the fluid induced forces for a conventional wear-ring seal impeller. Since the calculated impedances of Fig. 12 and Fig. 13 cannot be modeled by the traditional quadratic curve fit method, several alternative approaches are considered and suggested for the rotordynamic stability analysis. A FE model was constructed to implement the unbalance synchronous response analysis. In order to investigate the speed dependent impeller forces for the FE rotor model, speed dependent impedances are computed by employing the flow and head coefficients. Using the impedances, comparison of the

unbalance synchronous response is made between the quadratic approximation and the full impedance to estimate the validity of the approximated impedances by the least square curve-fit when the bump and dip are shown in the impedances. The computed unbalance synchronous responses of the quadratic approximation and the full impedance approaches indicate noticeable differences. A linear curve-fit algorithm is utilized to identify the irregular shapes of impedances and the identified impedances are applied to a rotordynamic stability analysis of a Jeffcott rotor model in the form of transfer functions. Earlier work utilizing the transfer function approach to address the unconventional impedance curves was suggested by Kleyhans et al.[21] and Thorat et al. [22] expanded the approach. However, Kleyhans' approach had limitations such as low curve-fit quality and limited frequency range for its application. The transfer function derived by Thorat was open-loop unstable. Two alternate approaches were developed to address these limitations. An approach using fictitious, fast poles was developed to obtain open-loop stable transfer functions. In addition to that, segmentation is utilized to perform linear curve-fits of sufficiently low order to facilitate reliable eigenvalue results. After the verification using the approximated (pure quadratic) impedance case, the transfer function model with segmentation is applied for the stability analysis of the unconventional (bump and dip) impedance case. Comparison between the actual impedance and the approximated impedance cases is made to demonstrate the limitations of the conventional MCK model and show the effects of ISR and spin speeds. The results show that bumps and dips in the impedance curves have a destabilizing influence on the Jeffcott rotor model as compared with the results from the quadratic curve fit

model. The developed transfer function model with segmentation provides good results for stability analysis even if the impedance functions have complex shapes that cannot be described well by the conventional quadratic curve form. Expanding the approach to more complicated rotor models and verifications with actual rotor tests is required as future studies.

Thirdly, a full set of the rotordynamic coefficients of the face-seal impeller has been calculated using the CFD approach. To calculate 4×4 mass, damping and stiffness coefficients, a whirling centrifugal impeller and a precessing centrifugal impeller have to be modeled and the reaction forces and moments should be calculated through the 3D whirling and precessing impeller simulation. The whirling centrifugal impeller simulation for predicting the rotordynamic coefficients using CFD technique was well validated by Moore et al. [12]. In the present study, a CFD modeling approach for a precessing impeller is developed and validated by considering a test case by Yoshida et al. [7]. Using the validated CFD approaches for the rotordynamic force and moment coefficients, a full set of the rotordynamic coefficients of the face-seal impeller is calculated and the stability analysis is performed. Childs [44] suggested a new formula of whirl frequency ratio at instability for circular and conical motion. In this study, the formula is employed to evaluate the stability of the face-seal impeller by assuming a situation that the impeller is whirling and precessing while it is operating. The calculated whirl frequency ratio at instability for circular and conical motion increases when coupled (circular and conical) motion arise during the impeller operation. The coupled circular and conical motion can be modeled with a single CFD model by imposing

dynamic eccentricity and tilting angle. Because of the geometrical limitation, small angles, 0.025 ° and 0.05 °, are imposed with the 10% of the dynamic eccentricity and the whirl frequency ratios at instability for the coupled motion are calculated to check the influence of the precessing motion on the rotordynamic stability. With the larger inclined angle of the impeller, the whirl frequency ratio at instability is increasing and this trend is identical with the conclusions of Childs [44] and Tsujimoto et al. [45] that the precessing motion makes the impeller more destabilizing.

Lastly, the influence of the static eccentricity on the face-seal impeller is investigated. Since whirling about the statically eccentric position is asymmetric, a special treatment has to be applied in the model. In order to make axisymmetric motion about the whirling center located at the eccentric position, a sliding surface is inserted and the whirl frequency is imposed by rotating the inner region that has the same center with the generated sliding surface. The developed approach for the statically eccentric rotor motion is validated for the measured data of the misaligned plain annular seals. The predicted results calculated by the CFD approach show fairly good agreement with the results of the measurement and other analytical results. This validated approach is applied to a shrouded face-seal impeller case to investigate the effect of the static eccentricity on the fluid induced forces of the shrouded impeller. Peaks are observed in the predicted impedances curves of the statically eccentric face-seal impeller and the magnitude of the bump and dip is increasing as the eccentric ratio increases. The conventional least square curve-fit for calculating the mass, damping, and stiffness coefficients of the impeller cannot be utilized for the fluctuating impedance curves. Thus,

the newly developed linear curve-fit algorithm with segmentation approach is applied to identify the impedances of the statically eccentric impeller and the transfer functions of the impedance curves are determined from the curve-fit. A simplified Jeffcott rotor model with the impeller impedances is considered to evaluate the influence of the static eccentricity. Since the magnitudes of the impedances are relatively small, the influence of the static eccentricity on the impeller seems small with the larger mass. However, with the decreased mass, it can be seen that the increased static eccentricity makes the Jeffcott rotor model more destabilized.

The following items can be expected future works:

a) Influences of the interaction between impeller and volute casing/ vaned diffuser needs to be investigated in terms of rotordynamic stability
b) Investigate the effect of the temperature on the fluid force (especially, compressible flow)
c) Various eye-seals with impeller shroud leakage path need to be considered.
d) A complete model of a centrifugal impeller including impeller, front/backshroud, and volute casing with various perturbation model needs to be modeled and analyzed.

REFERENCES

[1] Jery, B., Acosta, A. J., Brennen, C. E., and Caughey, T. K., 1984, "Hydrodynamic Impeller Stiffness, Damping, and Inertia in the Rotordynamics of Centrifugal Flow Pumps," Rotordynamic Instability Problems in High Performance Turbomachinery, NASA CP No. 2250, proceedings of a workshop held at Texas A&M University, pp. 137-160.

[2] Bolleter, U., Wyss, A., Welte, I., and Sturchler, R., 1987, "Measurement of Hydrodynamic Interaction Matrices of Boiler Feed Pump Impellers," Journal of Vibration, Stress, and Reliability in Design, 109, pp. 144-151.

[3] Bolleter, U., Leibundgut, E., Sturchler, R., and McCloskey, T., 1989, "Hydraulic Interaction and Excitation Forces of High Head Pump Impellers," in Pumping Machinery – 1989, Proceedings of the Third Joint ASCE/ASME Mechanics Conference, La Jolla, CA, pp. 187-194.

[4] Ohashi, H., Sakuraki, A., and Nishikoma, J., 1988, "Influence of Impeller and Diffuser Geometries on the Lateral Fluid Forces of Whirling Centrifugal Impeller," Rotordynamic Instability Problems in High Performance Turbomachinery, NASA CP No. 3026, proceedings of a workshop held at Texas A&M University, pp. 285-306.

[5] Yoshida, Y., and Tsujimoto, Y., 1990, "An Experimental Study of Fluid Forces on a Centrifugal Impeller Rotating and Whirling in a Volute Casing," in Proceedings, the Third International Symposium on Transport Phenomena and Dynamics of Rotating Machinery (ISROMAC-3), Honolulu, HI, 2, pp. 483-506.

[6] Tsujimoto, Y., Yoshida, Y., Ohashi, H., Teramoto, and N., Ishizaki, S., 1997, "Fluid Force Moment on a Centrifugal Impeller Shroud in Precessing Motion," ASME J. Fluids Eng., 119(2), pp. 366-371.

[7] Yoshida, Y., Saito, A., Ishizaki, S., and Tsujimoto, Y., 1996, “Measurement of the Flow in the Backshroud/Casing Clearance of a Precessing Centrifugal Impeller,” Proceedings of the 6th International Symposium on Transport Phenomena and Dynamics of rotating Machinery, Honolulu, Hawaii, 2, pp. 151-160.

[8] Childs, D., 1989,“Fluid-Structure Interaction Forces at Pump Impeller-Shroud Surfaces for rotordynamic Calculations,” Journal of Vibration, Acoustics, Stress, and Reliability in Design, Vol. 111, pp. 216-225.

[9] Gupta, M. K., 2005, “Bulk-Flow Analysis for Force and Moment Coefficients of a Shrouded Centrifugal Compressor Impeller,” Master’s thesis, Mechanical Engineering Dept., Texas A&M University, College Station, TX.

[10] Baskharone, E. A., Daniel, A. S., and Hensel, S. J., 1994, “Rotordynamic Effects of the Shroud-to-Housing Leakage Flow in Centrifugal Pumps,” ASME J. Fluid Eng., 116(3), pp. 558-563.

[11] Baskharone, E. A., and Wyman, N. J., 1999, “Primary/Leakage Flow Interaction in a Pump Stage,” ASME J. Fluid Eng., 121(1), pp. 133-138.

[12] Moore, J. J., and Palazzolo, A. B., 2001, “Rotordynamic Force Prediction of Whirling Centrifugal impeller Shroud Passages Using computational Fluid dynamic Techniques”, ASME Journal of Engineering for Gas Turbines and Power, Vol. 123, pp. 910-918.

[13] Moore, J. J., and Palazzolo, A. B., 1998, ‘‘CFD Comparison to Three-Dimensional Laser Anemometer and Rotordynamic Force Measurements for Grooved Liquid Annular Seals,’’ presented at the ASME/STLE International Tribology Conference, Oct. 25–29, Toronto, Ontario, Canada.

[14] Moore, J. J., Ransome D. L., and Viana, F., 2011, "Rotordynamic Force Prediction of Centrifugal Compressor Impellers Using Computational Fluid Dynamics", ASME Journal of Engineering for gas Turbines and Power, Vol. 133, 042504.

[15] Franz, R., and Arndt, N., March, 1986, "Measurement of Hydrodynamic Forces on the Impeller of HPOTP of the SSME", Report Number E249.2, California Institute of Technology

[16] Brennen, C. E., Franz, R., Arndt, N., 1988, "Effects of Cavitation on Rotordynamic Force Matrices," Proceedings of the 3rd Conference on Advanced Earth-to Orbit Propulsion Technology, Huntsville, AL, NASA Conference Publication No. CP-3012. NASA, Washington, DC, pp. 227-239.

[17] Childs, D., 1991, "Fluid-Structure Interaction Forces at Pump Impeller-Shroud Surfaces for Axial Vibration Analysis," ASME J. Vib. Acoust., Vol. 113, pp. 108-115.

[18] Childs, D., 1991, "Centrifugal-Acceleration Modes for Incompressible Fluid in the Leakage Annulus Between a Shrouded Pump Impeller and Its Housing," ASME J. Vib. Acoust., Vol. 113, pp. 209-218.

[19] Childs, D., 1992, "Pressure Oscillation in the Leakage Annulus Between a Shrouded Impeller and Its Housing Due to Impeller-Discharge-Pressure Disturbances," Journal of Fluids Engineering, Vol. 114, pp. 61-67.

[20] Williams, J., Childs, D., 1991, "Influence of Impeller Shroud Forces on Turbopump Rotor Dynamics," ASME J. Vib. Acoust., 113(10), pp. 508-515.

[21] Kleyhans, G., and Childs, D., 1997, "The Acoustic Influence of Cell Depth on the Rotordynamic Characteristics of Smooth-Rotor/Honeycomb-Stator Annular Gas Seals," ASME J. Eng. Gas Turbines Power, 199(4), pp. 949-957.

[22] Thorat, M., and Childs, D., 2010, "Predicted Rotordynamic Behavior of a Labyrinth Seal as Rotor Surface Speed Approaches Mach 1," ASME J. Eng. Gas Turbines Power, 132(11), p. 112504.

[23] Falco, M., Mimmi, G., and Marenco, G., 1986, "Effects of Seals on Rotor Dynamics," Proceedings of the International Conference on Rotordynamics, Sept. 14-17, Tokyo, Japan.

[24] Nelson, C. C. and Nguyen, D. T., 1988, "Analysis of Eccentric Annular Seals – Part I: A new Solution Using Fast Fourier transforms for Determining Hydrodynamic Force," ASME J. of Trib., 110, pp. 354-359.

[25] Nelson, C. C. and Nguyen, D. T., 1988, "Analysis of Eccentric Annular Seals – Part II: Effects of Eccentricity on Rotordynamic Coefficients," ASME J. of Trib., 110, pp. 361-366.

[26] Jenssen, D. N., 1970, "Dynamics of Rotor Systems Embodying High Pressure Ring Seals," Ph.D. dissertation, Heriot-Watt University, Edinburgh, Scotland.

[27] Allaire, P. E., Gunter, E. J., Lee, C. P., and Barrett, L. E., "The Dynamic Analysis of the Space Shuttle Main Engine-High Pressure Fuel Turbopump. Part II – Load Capacity and Hybrid Coefficients for the Turbulent Interstage Seals," University of Virginia, Report No. UVA/528140/ME76/103.

[28] Padavala, S. and Palazzolo, A. B., 1994, "Simulation Study with Arbitrary Profile Liquid Annular Seals," TRIBOLOGY TRANSACTIONS, 37, pp. 667-678.

[29] Kanki, H., and Kawakami, T., 1984, "Experimental Study on the Dynamic Characteristics of Pump Annular Seals," in Vibrations in Rotating Machinery, proceedings of the third IMechE International Conference on Vibrations in Rotating Machinery, York, England, pp. 159-166.

[30] San Andres, L., 1991, "Analysis of Variable Fluid Properties, Turbulent Annular Seals," ASME Trans., J. of Tribology, Vol. 113, pp. 684-702.

[31] Kanki, H., and Kawakami, T., 1987, Experimental Study on the Dynamic Characteristics of Screw Grooved Seals," Rotating Machinery Volume 1, ASME DE-Vol. 2, pp. 273-278.

[32] Marquette, O. R., Childs, D. W., San Andres, L., 1997, "Eccentricity Effects on the Rotordynamic Coefficients of Plain Annular Seals: Theory Versus Experiment" ASME Trans., J. of Tribology, Vol. 119, No. 3, pp. 443-448.

[33] Marquette, O. R., Childs, D. W., Phillips, S. G., 1997, "Theory versus Experiment for Leakage and Rotordynamic Coefficients of Circumferentially-Grooved Liquid Annular Seals With L/D of 0.45," ASME Fluids Engineering Division Summer Meeting FEDSM'97 June 22-26, FEDSM97-3333.

[34] API, 2002, Axial and Centrifugal Compressors and Expander-Compressors for Petroleum, Chemical and Gas Industry Services, API Standard 617, 7th ed., American Petroleum Institute, Washington, DC.

[35] Moore, J. J., 1999, "Rotordynamic Prediction of Centrifugal Impeller Shroud Passages using Computational Fluid Dynamic Techniques with A Combined Primary/Secondary Flow Model," Ph.D. thesis, Mechanical Engineering Dept., Texas A&M University, College Station, TX.

[36] ANSYS CFX-Solver Theory Guide, release 13.0, November 2010

[37] Grotjans, H. and Menter, F.R., 1988, "Wall functions or general application CFD codes," ECCOMAS 98 Proceedings of the Fourth European Computational Fluid Dynamics Conference, pp. 1112-1117

[38] Spalart, P.R. and Shur, M., 1997, "On the sensitization of turbulence models to rotation and curvature," Aerospace Sci. Tech., 1(5), pp. 297-302

[39] Rhie, C.M. and Chow, W.L., 1983, "Numerical Study of the Turbulent Flow Past an Airfoil with Trailing Edge Separation," AIAA J., 21, 1525-1532

[40] Majumdar, S., 1988, "Role of underrelaxtion in momentum interpolation for calculation of flow with nonstaggered grids," Numerical Heat Transfer, 13, pp. 125-132

[41] Alemi, H., Nourbakhsh, S.A., Raisee, M., and Najafi,, A. F., 2015, "Effects of Volute Curvature on Performance of a Low Specific-Speed Centrifugal Pump at Design and Off-Design Conditions," ASME Journal of Turbomachinery, Vol. 137, p. 041009

[42] Wright, T., 1999, *FLUID MACHINERY – Performance, Analysis, and Design*, CRC Press LLC, Boca Raton, U.S., Chap. 2.

[43] Levi, E. C., "Complex-Curve Fitting," IRE Trans. On Automatic Control, Vol.AC-4(1959), pp. 37-44

[44] Childs D. W: Turbomachinery Rotordynamics with Case Studies. Minter Spring; 1ST edition(2013)

[45] Tsujimoto, T., Z. Ma, B. Song and H. Horiguchi, 2010, "Moment Whirl due to Leakage Flow in the Back Shroud Clearance of a Rotor," International Journal of Fluid Machinery and Systems, 3(3), July-September, 2010, pp. 235-244

[46] Song,B., H. Horiguchi, Z. Ma, Tsujimoto, T., 2010, "Rotordynamic Instability Caused by the Fluid Force Moments on the Backshroud of a Francis Turbine Runner," International Journal of Fluid Machinery and Systems, 3(1), January-March, pp. 76-79.

[47] Childs, D., and Muhammed, A., 2013, "Comments on a Newly-Identified Destabilizing Rotordynamic Mechanism Arising in Vertical Hydraulic Turbines and the Back Shroud of Centrifugal Impellers," Proceedings of ASME Turbo Expo 2013: Turbine Technical Conference and Exposition, June 3-7, San Antonio, Texas, USA, GT2013-94202

[48] Childs, D., personal communication at Texas A&M University, July 13, 2016

APPENDIX A

1. Transfer functions for Fig. 30

Segment No.	Transfer function	
	$D(s)$	$E(s)$
1	$D_1(s)=\dfrac{2.225\times10^{18}s^2}{s^3+1.8\times10^6 s^2}\dfrac{+5.339\times10^{21}s+1.75\times10^{24}}{+1.07\times10^{12}s+2.1\times10^{17}}$	$E_1(s)=\dfrac{-2.817\times10^{17}s^2}{s^3+1.8\times10^6 s^2}\dfrac{+1.062\times10^{21}s+1.792\times10^{24}}{+1.07\times10^{12}s+2.1\times10^{17}}$
2	$D_2(s)=\dfrac{2.167\times10^7 s^3+1.78\times10^{24}s^2}{s^4+2.6\times10^6 s^3+2.51\times10^{12}s^2}\dfrac{+4.271\times10^{27}s+1.4\times10^{30}}{+1.066\times10^{18}s+1.68\times10^{23}}$	$E_2(s)=\dfrac{9.288\times10^6 s^3-2.253\times10^{23}s^2}{s^4+2.6\times10^6 s^3+2.51\times10^{12}s^2}\dfrac{+8.499\times10^{26}s+1.434\times10^{30}}{+1.066\times10^{18}s+1.68\times10^{23}}$
3	$D_3(s)=\dfrac{-9.987\times10^7 s^3+1.78\times10^{24}s^2}{s^4+2.6\times10^6 s^3+2.51\times10^{12}s^2}\dfrac{+4.271\times10^{27}s+1.4\times10^{30}}{+1.066\times10^{18}s+1.68\times10^{23}}$	$E_3(s)=\dfrac{-2.814\times10^7 s^3-2.253\times10^{23}s^2}{s^4+2.6\times10^6 s^3+2.51\times10^{12}s^2}\dfrac{+8.499\times10^{26}s+1.434\times10^{30}}{+1.066\times10^{18}s+1.68\times10^{23}}$

2. Transfer functions for Fig. 32

1) $D(s)$

Segment No.	Transfer function
1	$$D(s)=\frac{\begin{array}{l}-7.994\times10^{72}s^{18}+5.348\times10^{75}s^{17}-2.421\times10^{79}s^{16}+1.621\times10^{82}s^{15}\\-3.03\times10^{85}s^{14}+2.036\times10^{88}s^{13}-2.017\times10^{91}s^{12}+1.365\times10^{94}s^{11}\\-7.61\times10^{96}s^{10}+5.192\times10^{99}s^9-1.552\times10^{102}s^8+1.066\times10^{105}s^7\\-1.068\times10^{107}s^6+7.884\times10^{109}s^5+2.553\times10^{112}s^4-1.013\times10^{115}s^3\\+7.944\times10^{117}s^2+9.146\times10^{119}s+1.183\times10^{123}\end{array}}{\begin{array}{l}s^{19}+2.66\times10^7 s^{18}+3.323\times10^{14}s^{17}+2.591\times10^{21}s^{16}+1.413\times10^{28}s^{15}\\+5.729\times10^{34}s^{14}+1.789\times10^{41}s^{13}+4.404\times10^{47}s^{12}+8.668\times10^{53}s^{11}\\+1.376\times10^{60}s^{10}+1.768\times10^{66}s^9+1.839\times10^{72}s^8+1.541\times10^{78}s^7\\+1.031\times10^{84}s^6+5.428\times10^{89}s^5+2.195\times10^{95}s^4+6.573\times10^{100}s^3\\+1.372\times10^{106}s^2+1.778\times10^{111}s+1.077\times10^{116}\end{array}}$$

2) $E(s)$

Segment No.	Transfer function
1	$E(s)=\dfrac{\begin{array}{l}-2.458\times10^{73}s^{18}+1.386\times10^{76}s^{17}-8.481\times10^{79}s^{16}+4.494\times10^{82}s^{15}\\-1.242\times10^{86}s^{14}+6.126\times10^{88}s^{13}-1.006\times10^{92}s^{12}+4.558\times10^{94}s^{11}\\-4.908\times10^{97}s^{10}+2.009\times10^{100}s^{9}-1.475\times10^{103}s^{8}+5.319\times10^{105}s^{7}\\-2.681\times10^{108}s^{6}+8.182\times10^{110}s^{5}-2.779\times10^{113}s^{4}+6.654\times10^{115}s^{3}\\-1.447\times10^{118}s^{2}+2.802\times10^{120}s+7.23\times10^{112}\end{array}}{\begin{array}{l}s^{19}+2.66\times10^{7}s^{18}+3.323\times10^{14}s^{17}+2.591\times10^{21}s^{16}+1.413\times10^{28}s^{15}\\+5.729\times10^{34}s^{14}+1.789\times10^{41}s^{13}+4.404\times10^{47}s^{12}+8.668\times10^{53}s^{11}\\+1.376\times10^{60}s^{10}+1.768\times10^{66}s^{9}+1.839\times10^{72}s^{8}+1.541\times10^{78}s^{7}\\+1.031\times10^{84}s^{6}+5.428\times10^{89}s^{5}+2.195\times10^{95}s^{4}+6.573\times10^{100}s^{3}\\+1.372\times10^{106}s^{2}+1.778\times10^{111}s+1.077\times10^{116}\end{array}}$

3. Transfer functions for Fig. 33

1) $D(s)$

Segment No.	Transfer function
1	$D_1(s)=\dfrac{1.973\times10^{8}s^{3}-3.849\times10^{22}s^{2}+1.935\times10^{27}s+1.81\times10^{30}}{s^{4}+2.6\times10^{6}s^{3}+2.51\times10^{12}s^{2}+1.066\times10^{18}s+1.68\times10^{23}}$
2	$D_2(s)=\dfrac{1.439\times10^{22}s^{3}+1.318\times10^{25}s^{2}+1.949\times10^{27}s+1.887\times10^{30}}{s^{4}+2.6\times10^{6}s^{3}+2.51\times10^{12}s^{2}+1.066\times10^{18}s+1.68\times10^{23}}$
3	$D_3(s)=\dfrac{-2.936\times10^{22}s^{3}+9.032\times10^{24}s^{2}+8.89\times10^{26}s+1.774\times10^{30}}{s^{4}+2.6\times10^{6}s^{3}+2.51\times10^{12}s^{2}+1.066\times10^{18}s+1.68\times10^{23}}$
4	$D_4(s)=\dfrac{-1.327\times10^{22}s^{3}+4.616\times10^{24}s^{2}+1.886\times10^{27}s+1.499\times10^{30}}{s^{4}+2.6\times10^{6}s^{3}+2.51\times10^{12}s^{2}+1.066\times10^{18}s+1.68\times10^{23}}$
5	$D_5(s)=\dfrac{-6.43\times10^{21}s^{3}+2.385\times10^{24}s^{2}+2.746\times10^{27}s+1.204\times10^{30}}{s^{4}+2.6\times10^{6}s^{3}+2.51\times10^{12}s^{2}+1.066\times10^{18}s+1.68\times10^{23}}$
6	$D_6(s)=\dfrac{-1.783\times10^{23}s^{4}-4.054\times10^{25}s^{3}+2.667\times10^{29}s^{2}+3.976\times10^{33}s+6.514\times10^{35}}{s^{5}+3.5\times10^{6}s^{4}+4.85\times10^{12}s^{3}+3.325\times10^{18}s^{2}+1.127\times10^{24}s+1.512\times10^{29}}$

2) $E(s)$

Segment No.	Transfer function
1	$E_1(s)=\frac{1.316\times10^{8}s^3-1.726\times10^{25}s^2+4.195\times10^{27}s+1.136\times10^{30}}{s^4+2.6\times10^{6}s^3+2.51\times10^{12}s^2+1.066\times10^{18}s+1.68\times10^{23}}$
2	$E_2(s)=\frac{7.767\times10^{22}s^3-1.381\times10^{25}s^2+4.27\times10^{27}s+1.162\times10^{30}}{s^4+2.6\times10^{6}s^3+2.51\times10^{12}s^2+1.066\times10^{18}s+1.68\times10^{23}}$
3	$E_3(s)=\frac{2.701\times10^{22}s^3-1.021\times10^{24}s^2+2.891\times10^{27}s+1.508\times10^{30}}{s^4+2.6\times10^{6}s^3+2.51\times10^{12}s^2+1.066\times10^{18}s+1.68\times10^{23}}$
4	$E_4(s)=\frac{6.595\times10^{21}s^3+2.6\times10^{23}s^2+1.642\times10^{27}s+1.587\times10^{30}}{s^4+2.6\times10^{6}s^3+2.51\times10^{12}s^2+1.066\times10^{18}s+1.68\times10^{23}}$
5	$E_5(s)=\frac{4.329\times10^{20}s^3+6.36\times10^{22}s^2+1.005\times10^{27}s+1.565\times10^{30}}{s^4+2.6\times10^{6}s^3+2.51\times10^{12}s^2+1.066\times10^{18}s+1.68\times10^{23}}$
6	$E_6(s)=\frac{1.51\times10^{24}s^4+2.373\times10^{26}s^3+1.318\times10^{30}s^2+8.438\times10^{32}s+1.628\times10^{36}}{s^5+3.5\times10^{6}s^4+4.85\times10^{12}s^3+3.325\times10^{18}s^2+1.127\times10^{24}s+1.512\times10^{29}}$

APPENDIX B

Shroud only Model with whirling and precessing

A shroud model with the dynamic eccentricity and tilting angle is generated as shown in Fig. 78. The figure shows the whirling and precessing shroud which has 3 domains with inclined shroud rotor surface. The imposed eccentric value, α, is 0.6 mm(about 10% of the shroud clearance) and the tilting angle is 0.05° by considering the clearance between the face-seal and the stator. Fig. 79 illustrates domains and surfaces that are defined for the rotordynamic analysis using the commercial CFD program, ANSYS CFX. The eccentricity and the tilting angle are imposed on the 'Diff_Inlet', 'Sh_Rotor', 'In_Rotor', and 'In_Outlet' as shown in Fig. 79.

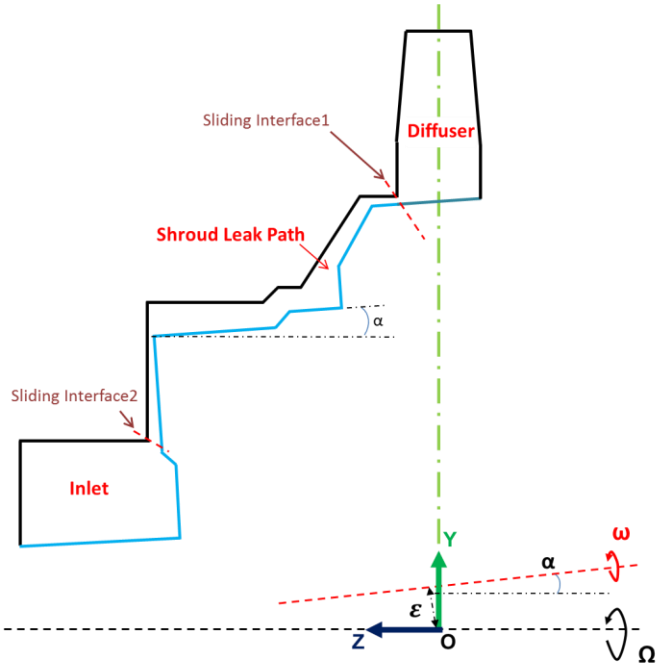

Fig. 78 Schematic of the shroud only model with the whirling and precessing

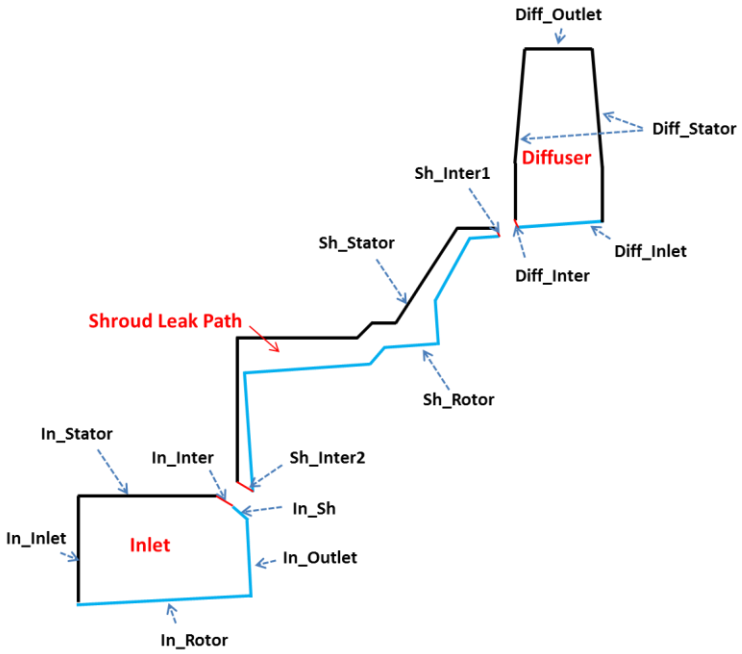

Fig. 79 Domains of the shroud only model with the whirling and precessing

The tilted shroud surface is whirling at the speed Ω about Z-axis while the rotor surface spins at the speed of ω about the tilted axis. In ANSYS CFX, this motion can be solved by defining the fluid region as a rotating frame in the model while the stator wall is defined as a counter rotating wall. To impose the spin speed of ω, the shroud surface is defined as a rotating wall.

For the rotordynamic analysis, solutions for calculating dynamic coefficients of the model should be obtained at multiple frequency ratios defined as the ratio of the shroud whirling frequency to the spin speed, $f = \frac{\Omega}{\omega}$. Once a CFD solution is obtained at a certain frequency ratio, the radial and tangential forces can be determined by integrating the static pressure of the nodes on the tilted shroud surface. By calculating

the forces at multiple frequency ratios, the rotordynamic coefficients can be calculated using the relationship of Eq. (31). To solve the whirling shroud with the tilted angle using CFD approach, relative shroud speed should be utilized. The equation is

$$\omega_{shroud} = \omega - \Omega \tag{119}$$

Ω indicates the whirling speed and ω_{shroud} is the relative rotor speed. To simulate the multi domain problems with rotating frames, interface model is required. In this study, 'Frozen Rotor' model in ANSYS CFX is utilized to capture circumferential flow variation in the shroud leakage path. Since speeds of each domain are different, mesh connection method is needed to set the speed variation between the domains using GGI(General Grid Interface). The model does not require matching nodes on either side of two connected surfaces.

APPENDIX C

Shroud only Model with Static Eccentricity

Fig. 80 indicates statically eccentric shroud model to calculate the force coefficients. The model is composed of 4 domains and 3 sliding interfaces as shown in Fig. 81. Two separate domains in the shroud leakage path are utilized to impose the whirling frequency. Inner shroud leakage path should be defined as a rotating frame and the outer shroud leakage path should be defined as a stationary frame. The axis of whirling of the inner shroud leakage path is 'Axis of Whirling' of Fig. 80 and the axis of the shroud rotation is 'Axis of Rotation' and the location is defined as the sum of the dynamic eccentricity, ε and the static eccentricity, E_s. The position of the 'Axis of Whirling' is changing according to the eccentric ratio.

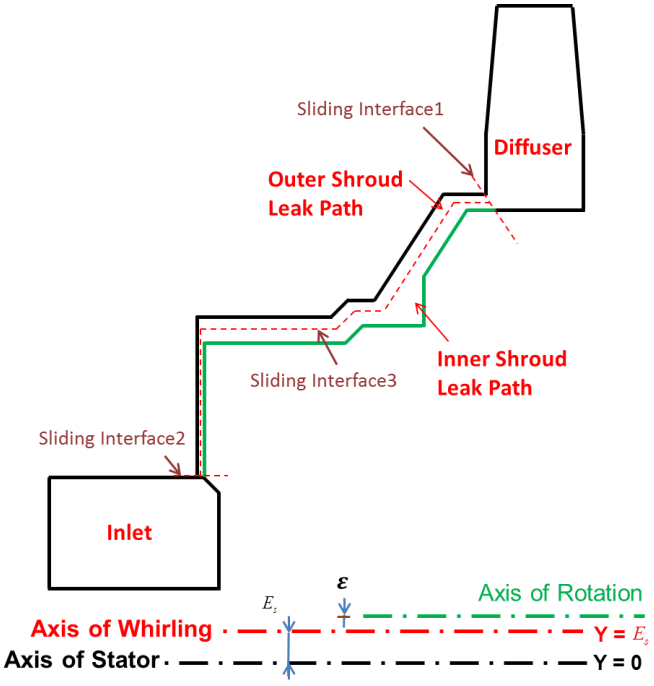

Fig. 80 Schematic of the shroud only model with the static eccentricity

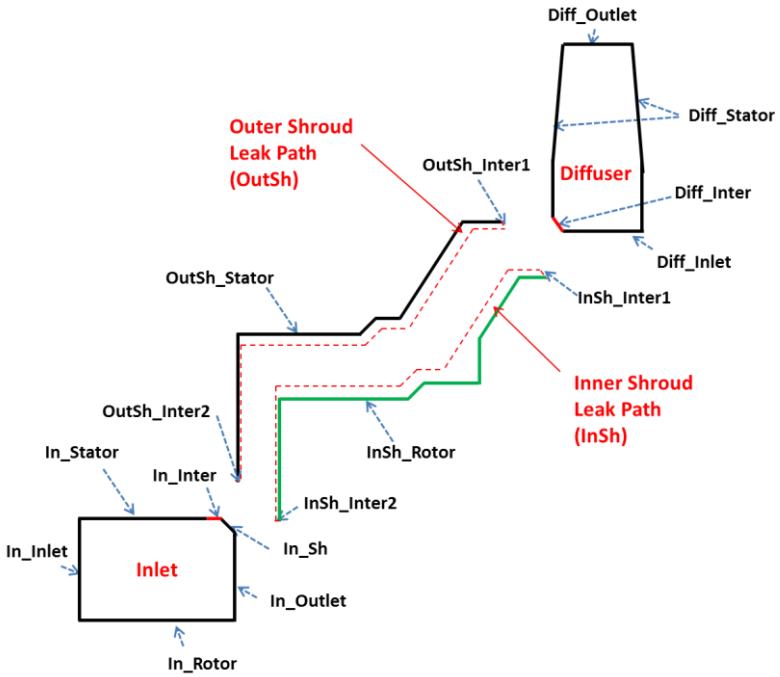

Fig. 81 Domains of the shroud only model with the static eccentricity

The orbit size of the shroud, ε is 10% of the shroud inlet gap(Gap 'A', 3.55 mm) . Overall procedure for calculating the force coefficients of the statically eccentric shroud model is same with the concentric case. The positions of 'Axis of Whirling' and 'Axis of Rotation' according to the impeller position and the eccentric ratio are indicated in Table 22 and Table 23.

Table 22 Position of 'Axis of Whirling' and 'Axis of Rotation' at $\Omega t = 0$

Eccentric ratio	Position of 'Axis of Whirling' (x, y)	Position of 'Axis of Rotation' (x, y)
0.2	(0, 0.71)	(0, 1.065)
0.4	(0, 1.42)	(0, 1.775)
0.6	(0, 2.13)	(0, 2.485)
0.8	(0, 2.84)	(0, 3.195)

(Unit : mm)

Table 23 Position of 'Axis of Whirling' and 'Axis of Rotation' at $\Omega t = \frac{\pi}{2}$

Eccentric ratio	Position of 'Axis of Whirling' (x, y)	Position of 'Axis of Rotation' (x, y)
0.2	(0.355, 0.71)	(0.355, 0.71)
0.4	(0.355, 1.42)	(0.355, 1.42)
0.6	(0.355, 2.13)	(0.355, 2.13)
0.8	(0.355, 2.84)	(0.355, 2.84)

(Unit : mm)